RAMAN SPECTROSCOPY OF THE CO_2-H_2O SYSTEM

A Thesis

Presented in Partial Fulfillment of the Requirements for

the Degree Master of Science

in the Graduate School of The Ohio State University

By

Ashley D. Swartzwelder

*****

The Ohio State University
2006

Master's Examination Committee: Approved by

Professor Heather C. Allen, Advisor

Professor Russell Pitzer

_____
Advisor
Graduate Program in Chemistry

ABSTRACT

CO_2 is considered to be a major contributor to global climate change. As the climate temperature has already increased by 2 ^{o}C since the industrial revolution, the increased concentration of CO_2 predicted to occur within the next few years is of major importance. Sequestration of anthropogenic CO_2 has been suggested as a method of remediation. One method of sequestration of CO_2 is to form CO_2 clathrates in the deep oceans. However, before this method can be utilized, the formation and dissolution of CO_2 clathrates must be better understood than it currently is. In this thesis, the CO_2-H_2O system is analyzed in the aqueous phase and in the clathrate phase (-17 ^{o}C and 15 atm) using Raman spectroscopy. The transition from the aqueous phase to the clathrate phase is followed. Frequency shifts are observed, indicating that weak van der Waals interactions occur between the H_2O and CO_2 molecules and is further supported with the spectra of the stretching and bending regions of H_2O. Narrowing of the Fermi diads of CO_2 is also observed after conversion from the solvated phase to the clathrate phase.

In addition, a solubility study is presented and determined the Henry's law constants to over a temperature range of 27 to 80 ^{o}C and a pressure range of 5 to 13 atm. At 27 ^{o}C, Henry's law constant was determined to be 3.42 x 10^{-2} M/atm. With increasing temperature, Henry's law constant decreased but was of the same order of magnitude.

To
My Parents
Tom and Ruth Swartzwelder

ACKNOWLEDGMENTS

Without the support of a large variety of people, I would not have been able to accomplish this goal. Without Dr. Heather Allen allowing me the opportunity to join her lab, I would never have completed this research. In addition, her recognition of my weaknesses and pushing me to overcome them has been the most gratifying part of this experience. I am extremely thankful for her constant support. Thanks to the members of the Allen lab, both past and present, who have all been there to answer my many questions. A special thank you goes to Kandice Harper, Lisa Van Loon, and Laura Voss for the countless brain-storming sessions but most of all for keeping me sane.

I thank my family who listened to all my experiment dilemmas while pretending they understood. Your suffering never went unnoticed. To the most important person in my life, Kyle Tomlin, I would never have survived this journey without your faith. You kept me going on the days I couldn't see the end. I thank Samantha Farley for proving to be the best friend a person can have. One of these days, though, you'll have to stop following me.

Finally, without the financial support of the American Chemical Society Petroleum Research Fund, I would not have been able to begin or complete this research.

VITA

April 7, 1982. . . . . .Born – South Point, OH

May 8, 2004. . . . . B. S. Chemistry
Marshall University

2004 – 2006. . . . . .Graduate Teaching and Research Assistant
The Ohio State University

FIELDS OF STUDY

Major Field: Chemistry

TABLE OF CONTENTS

LIST OF TABLES

LIST OF FIGURES

LIST OF ABBREVIATIONS

A.U.   arbitrary units

atm   atmosphere

CCD   charge coupled device

CW   continuous wave

°C   degrees Celsius

FD   Fermi diad(s)

$2\nu_2$ first overtone of the bending mode

FWHM   full-width at half-maximum

H   Henry's law constant

Ih   hexagonal ice

h   hour(s)

IR   infrared

K   Kelvin

L   liter(s)

MΩ Megaohms

m   milli

μ micro

min   minute(s)

mol	mole(s)
M	moles per liter
n	nano
NMR	nuclear magnetic resonance
ppm	parts per million
Pa	Pascal
PMT	photomultiplier tube
α	polarizability
s	second(s)
S/N	signal to noise ratio
sI	structure I
SS	symmetric stretch
ν	vibrational energy level
VI	virtual instrument
cm^{-1}	wavenumbers

CHAPTER 1

INTRODUCTION

Throughout the scientific community and the public, an increase in atmospheric CO_2 is believed to be a major contributor to global climate change.[1] CO_2 is the most important greenhouse gas in the atmosphere aside from water.[2] CO_2 absorbs radiation that is emitted by Earth that in turn leads to an increase in the temperature of the atmosphere. Current emission rates predict the concentration of CO_2 in the atmosphere will increase from 360 ppm to 1500 ppm by the end of the 21st century.[3,4] This increase is expected to result in a global warming increase of 2 to 5 ^oC.[4] According to current estimates, about 25% of CO_2 from the atmosphere enters the oceans[5] and can form solutions of aqueous CO_2 as well as ionic species that can impact the pH of the oceans. In addition, CO_2 exists in the form of clathrates in the deep ocean, the permafrost region, and is believed to exist on Mars.[6-8] It is a commonly accepted view that a way to mitigate anthropogenic CO_2 is to sequester CO_2 in the deep ocean.[9-14,3,4,9-16] Since CO_2 exists in a variety of phases on Earth and poses a threat to the environment, understanding the intermolecular interactions between the CO_2 and H_2O molecules is of great importance in the environmental sciences.[5,17]

1.1 Solvated CO_2

Clusters are of interest because they exhibit properties that are different from the properties of a molecule as well as those of the bulk solution.[18] CO_2 forms a variety of different sized water clusters of the form CO_2-$(H_2O)_n$ where n is the number of H_2O molecules. Depending on the number of H_2O molecules in the cluster, the structure, bond lengths, and stability of the cluster will change. It has been found that when n is greater than 3, the water molecules prefer to form a hydrogen bonded network among themselves. In the presence of CO_2, a solvation shell typically requires a large number of water molecules such as $n \geq 18$.[5] The crossover from noncrystalline to crystalline bulklike structure occurs for CO_2 clusters for the range of 25-32 molecules.[18] For smaller complexes, it has been suggested that the cluster is mainly held by electrostatic interactions between the two components with a much smaller van der Waals contribution.[5]

1.2 Clathrate Background

Clathrates are crystalline inclusion compounds that consist of guest molecules trapped inside polyhedral water cavities formed by a hydrogen bonded water network.[19,20] Clathrate clathrates form when small (<0.9 nm) nonpolar molecules come in contact with water at ambient temperatures (typically <300K) and moderate pressures (typically >0.6 MPa).[15] The presence of these guest molecules, in either the cage itself or in a large percentage of the surrounding cages, is required to prevent the clathrates from collapsing under their own attractive forces.[16] However, no chemical bonding exists between the host water molecules and the guest molecule.[21]

Three common types of clathrates exist: sI clathrate, sII clathrate, and sH clathrate, Figure 1.1.[15,19,21,22] Since only one guest molecule may occupy the cavity, the type of clathrate that forms is determined by the size of the guest molecule.[19,23] Only molecules with a diameter smaller than the diameter of the cavity will be entrapped.[21] The concept of "a ball fitting within a ball" is a good first approximation in understanding the properties of clathrates.[23] When fully occupied, the structure of all three clathrates is approximately 85 mol % water and 15 mol % gas.[15,23]

Structure I (sI) is a body-centered cubic structure that forms with small (0.4-0.55 nm) guest molecules.[15] A sI clathrate contains two different types of cavity: a pentagonal dodecahedral cavity (5^{12}) and a tetrakaidecahedral cavity ($5^{12}6^2$).[16,19,23] The water cages are described by the general notation X^n, where X is the number of sides of a cage face and n is the number of cage faces having these X sides.[19] The 5^{12} cavity consists of 12 pentagons while the $5^{12}6^2$ cavity is comprised of 12 pentagons and 2 hexagons. The unit cell contains 46 water molecules.[23] Structure II (sII) consists of a diamond lattice within a cubic framework that is formed with larger molecules (0.6-0.7 nm).[15,23] These clathrates form when 5^{12} cavities arrange so that they link together by sharing faces.[16,19,23] This arrangement results in the creation of a hexakaidecahedral ($5^{12}6^4$). The unit cell is comprised of 8 - $5^{12}6^4$ cavities and 16 - 5^{12} cavities and contains 136 water molecules.[16]

Structure H (sH) has a hexagonal framework and occurs in both man-made and natural environments.[15] Although sH is able to hold large molecules, it only exists with mixtures of both small and large (0.8-0.9 nm) molecules.[15] sH is comprised of three cavities: 5^{12}, $4^35^66^3$, and $5^{12}6^8$. In addition to the pentagonal and hexagonal faces, sH

also has a square face. Due to its large cavity size, sH is important in the oil industry since it can encage molecules found in crude oil.[19]

1.3 Solvated CO_2 vs. CO_2 clathrate

The same cages that form the CO_2 clathrate also exist as CO_2 clusters in the aqueous phase. These cages are the dodecahedral cage (20 H_2O molecules) and the tetrakaidecahedral cage (24 H_2O molecules). With the addition of the CO_2 molecule, it has been calculated in the literature that the tetrakaidecahedral cluster is stabilized the most relative to the unfilled cage by 8 kcal/mol whereas the dodecahedral cluster is not stabilized at all.[24] These stabilization energies suggest the preferred cluster cage for CO_2 is the tetrakaidecahedral cluster with a coordination number of 24 water molecules. In addition, Raman and NMR studies have shown that CO_2 only occupies the tetrakaidecahedral cavity of the sI clathrate. Since the preferred CO_2 cage structure for clusters and clathrates are the same, studies of CO_2 cluster cages could provide information about CO_2 clathrate cages.

1.4 The Carbonate System

Accurate analysis of the vibrational modes associated with solvated CO_2 and CO_2 clathrates must account for all species that result from the dissociation of CO_2 in water. Many studies have been done over the years to examine this dissociation and the subsequent equilibrium processes involving carbonate and bicarbonate ions. This equilibrium process is known as the carbonate system and includes the following reactions:

[1] $CO_{2(g)} \leftrightarrow CO_{2(aq)}$

[2] $CO_{2(aq)} + H_2O \leftrightarrow H_2CO_{3(aq)}$ $K_{eq} = 1.3 \times 10^{-3}$

[3] $H_2CO_{3(aq)} \leftrightarrow H^+_{(aq)} + HCO_3^-{}_{(aq)}$ $K_{a1} = 2.00 \times 10^{-4}$

[4] $HCO_3^-{}_{(aq)} \leftrightarrow H^+_{(aq)} + CO_3^{2-}{}_{(aq)}$ $K_{a2} = 4.69 \times 10^{-11}$
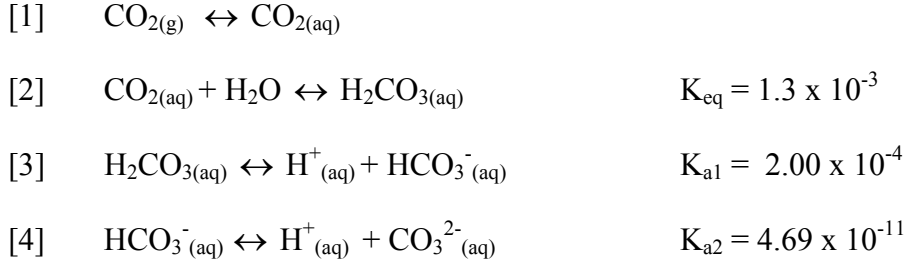
Although H_2CO_3 has not been observed in aqueous solutions using spectroscopy, it exists in both the solid state and in the gas phase.[17,25,26] Carbonic acid is not a stable species and is only present in a very small amount relative to $CO_{2(aq)}$ at equilibrium.[25,26]

1.5 Thermodynamics of Clathrates

In 1958, van der Waals and Platteeuw developed the first thermodynamic model to predict clathrate phase equilibria.[19] The well known van der Waals-Platteeuw (VDW-P) model is based on classical statistical thermodynamics. It performs well near the ice point of water but deviates significantly far from the ice point.[19] It is still used today in all later models that have been developed to predict the phase equilibria properties of clathrates. Several assumptions are made and must be considered when this model is used: (i) each cavity can contain at most one guest molecule; (ii) there is no interaction between the gas molecules in different cavities and the gas molecules interact only with the nearest neighbor water molecules; (iii) the gas molecule can freely rotate within the cavity which is treated as being perfectly spherical; and (iv) the clathrate lattice is not distorted by the guest molecule.[19,22,27]

The basic equations for the VDW-P model are shown in Equations 1.1-1.2.[16,19,27]

$$\mu_Q = \mu_Q{}^{\beta} + kT \sum_i v_i \ln\left(1 - \sum_K y_{k_i}\right) \qquad (1.1)$$

$$y_{K_i} = \frac{C_{K_i} f_K}{1 + \sum_J C_{J_i} f_i} \qquad (1.2)$$

Here μ_Q is the chemical potential of the solvent (water molecules) in the clathrate and μ_Q^β is the chemical potential of the metastable empty clathrate lattice, f_K is the fugacity of solute K, y_{Ki} is the probability of finding a solute molecule K in a host cavity of type I, C_{Ki} is an equilibrium constant for the Kth type of guest in the ith type of cavity, and v_i is the number of cavities of type i per water molecule in the clathrate lattice.
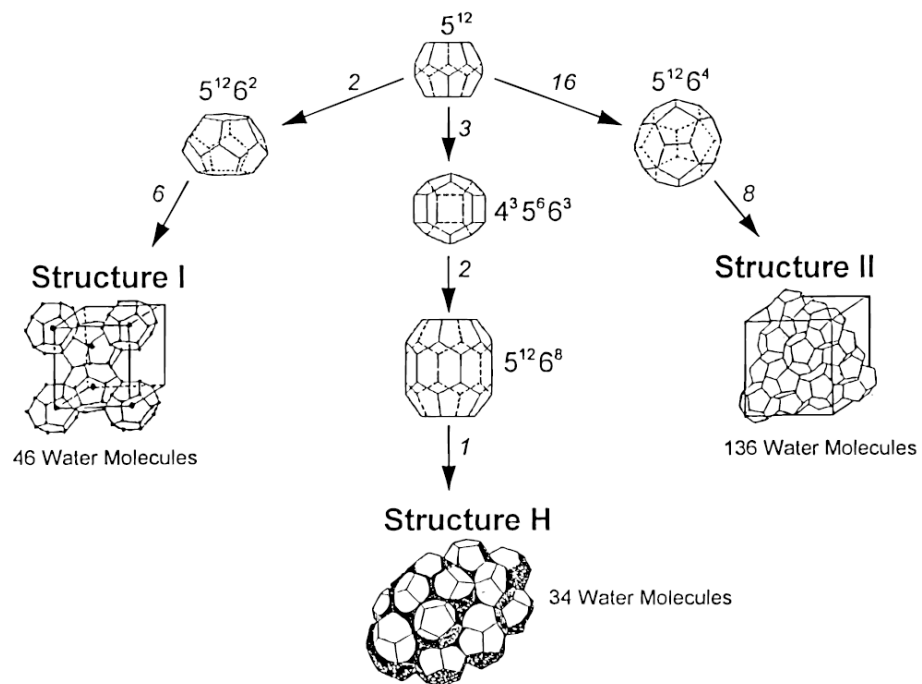
Figure 1.1: The three common clathrate structures with their corresponding unit cells.[19]

CHAPTER 2

THEORY AND EXPERIMENTAL

2.1 Raman Theory

Photons involved with the interaction of electromagnetic radiation are refracted, reflected, or scattered.[28] In Raman spectroscopy, detected scattered light from molecules is used to study the energy changes that result from this interaction. Information on the vibrational modes characteristic of the molecule is provided by the energy changes that are associated with the polarizability of the molecule.

Electromagnetic radiation is comprised of oscillating magnetic and electric fields which interact with the molecules.[28] Classically, light can cause electron clouds in a chemical bond to oscillate or polarize. This oscillation results in emission of light. The emitted light is called scatter.[28-31] Quantum mechanically, scatter is described by transitions between energy levels.[28] A molecule in the ground state absorbs a photon from the incident light and is excited to a virtual or intermediate level. A virtual level is not a real energy level of the molecule but exists due to the distortion of the electron distribution of the molecule.[30] This virtual state is not stable, and the light is immediately released as scattered radiation. In addition, the shape of the distorted electron cloud

depends on the magnitude of energy transferred to the molecule. Therefore, different frequencies of light affect the polarizability of the molecule differently.

There are two types of scatter: Rayleigh scatter and Raman scatter. The most intense form of scatter is Rayleigh scatter. The excited molecules relax back to the ground state by emitting a photon of the same frequency as that of the incident light.[28] No significant energy change occurs. This is also known as an elastic process due to the absence of an energy change. A less common event, known as Raman scatter, also occurs where only one of every 10^7 scattered photons is attributed to Raman scatter. This is an elastic process. Raman scatter occurs when the incident light interacts with the electron cloud and the nuclei move at the same time.[31] The molecule can either increase or decrease in energy depending on the original state of the molecule. This increase or decrease in energy is known as Stokes or anti-Stokes Raman scattering, respectively. When the molecule rests at a higher vibrational level after emitting a photon, the emitted photon has less energy indicating energy was transferred to the molecule. This process is known as Stokes scatter.   On the other hand, anti-Stokes scatter occurs when the emitted photon has more energy than the incident photon. In this case, the molecule has returned to a lower vibrational level. The molecule has decreased in energy. The types of scatter are shown in Figure 2.1. The two states marked *m* and *n* are different vibrational states of the ground electronic state.

The energy of the virtual state depends on the energy of the incident light. Therefore, the frequency of the absorption must account for the incident light. Raman frequencies are reported as the shift from the incident frequency. Equation 2.1 shows the

Raman shift equation where $\Delta\bar{\nu}$ is the frequency of the vibrational mode, $\bar{\nu}_R$ is the Rayleigh or incident laser energy, and $\bar{\nu}_S$ is the Stokes energy.

$$\Delta\bar{\nu} = \bar{\nu}_R - \bar{\nu}_S \qquad (2.1)$$

Prior to exposure to radiation, most molecules are likely to reside in the ground vibrational state at room temperature. At thermal equilibrium, the ratio of Stokes and anti-Stokes intensities is determined by the Boltzmann distribution, Equation 2.2, where N_n is the number of molecules in the excited vibrational energy level (n), N_m is the number of molecules in the ground vibrational energy level (m), g_i is the degeneracy of the level i and m, ΔE is the energy difference between the vibrational energy levels, and k is Boltzmann's constant. At thermal equilibrium, a lower vibrational level is more heavily populated than a higher vibrational level. Since Stokes scatter intensity is dependent on the number of molecules in the lowest vibrational level, it will always be larger than the anti-Stokes scatter intensity.[30-32] Therefore, the majority of Raman scattering is Stokes Raman scatter.

$$\frac{N_n}{N_m} = \frac{g_n}{g_m} \exp\left[\frac{-\Delta E}{kT}\right] \qquad (2.2)$$

2.2 Vibrational Modes

The following is a brief description of vibrational modes. Further information can be found in the literature.[28,30,33,34] For a molecule with k normal modes, let each vibrational mode be described by the wave function $\psi_i(\nu_i)$ where i represents the ith normal mode of the molecule and ν_i represents the kth quantum state of that mode. To describe the total vibrational wave function, ψ_v, of the molecule, the product of the individual vibrational wave functions may be used, Equation 2.3.

$$\psi_v = \psi_1(v_1)\ \psi_2(v_2)\ \psi_3(v_3)\ \dots\psi_k(v_k) \tag{2.3}$$

The molecule is in its vibrational ground state when each v_i is zero. If one vibrational mode is excited to the $v_i = 1$ state by absorption of radiation while the remaining normal modes remain in the lowest states, then the molecule has undergone a fundamental transition for that particular vibration.[33] A fundamental transition occurs when a molecule obeys $\Delta v = +1$ and starts in the ground state.

The number of normal vibrational modes a molecule is given by 3N-5 if linear and 3N-6 if non-linear. N is the number of atoms. However, not all of these vibrational modes are observed in a Raman spectrum. Those that are observed can be predicted by selection rules and are called Raman active. Selection rules state if the transition of a fundamental vibration will be observed in the spectrum but it does not predict the intensity of a particular band.

The selection rules for Raman spectroscopy are dependent on the polarizability, α, as indicated in Equation 2.4:

$$\int \psi^*(v')\alpha\psi(v)d\tau \tag{2.4}$$

where $\psi(v')$ represents the excited state and $\psi(v)$ represents the ground state of the molecule. For this integral to be nonzero, its integrand must be totally symmetric, meaning that the product of the ground state, the operator, and the excited state symmetry must be totally symmetric.[28] *This selection rule states that the vibration will only be observed when the polarizability changes during the transition.* This change in polarizability is the basis of Raman spectroscopy.

Since CO_2 is a linear molecule with three atoms, it has four fundamental vibrational modes: a symmetric stretch, an asymmetric stretch, and two degenerate

bending modes, Figure 2.2. However, only the symmetric stretch of CO_2 is Raman active, and it appears at 1334 cm^{-1}. The other three vibrational modes are IR active and will not be discussed further. Although only one normal mode is Raman active, other vibrational modes are observed. This is because transitions exist in addition to the fundamental transitions.

Overtone transitions are observed in the $CO_{2(g)}$ Raman spectra. An overtone occurs when a mode is excited beyond the $v=1$ state. The mode can be excited to the $v=2, 3,…$ from the ground state. Since multiple overtones can occur for the same vibrational mode, a naming system is used to identify different overtones. If the mode is excited to the $v=2$ or $v=3$ state, it is called the first or second overtone of the vibrational mode, respectively. The first overtone of the $CO_{2(g)}$ bending mode v_2 is observed at 1340 cm^{-1}. Hot bands are also observed in the $CO_{2(g)}$ spectrum. Hot bands occur when an already excited vibrational mode is futher excited. For example, if a vibrational mode in the $v=1$ state is excited to the $v=2$ state.

2.3 Raman Experimental Setup

A 532 nm continuous wave (CW) laser (Spectra-Physics, Millennia II, ~95 mW) was used to obtain the Raman spectra. A fiber optic probe (InPhotonics, RP 532-05-15-FC) both delivers the laser excitation source to the sample and collects the scattered light. A 200 μm collection fiber optic (InPhotonics, Inc.) delivers the scattered light to the entrance slit of a 500 mm monochromator (Acton Research, SpectraPro 500i). A 1200 g/mm grating blazed at 1 μm was used. The slit width was set to 50.0 μm with a resolution of 2.23 cm^{-1}. A liquid nitrogen cooled CCD camera (Roper Scientific,

N400EB, 1340 x 400 pixel array, back-illuminated and deep depletion CCD) collected

the data. The CCD was calibrated using the 435.83 nm line of a fluorescent lamp. The

1382 cm^{-1} peak of a crystalline naphthalene spectrum was used to calibrate the

wavenumber position by comparing the observed position to literature values.[29] Data

collection and display were performed using the SpectraSense software (Acton Research,

version 4.2.9). A basic diagram of the Raman setup is shown in Figure 2.2.

2.4 $CO_{2(g)}$

$CO_{2(g)}$ (99.9 % purity) was bubbled into a stainless steel cell (200 mL volume). A

spectrum of $CO_{2(g)}$ was acquired at 10 atm using a 300 s integration time. The

experiment was performed at 23 ± 2 ^{o}C.

2.5 The Carbonate System

An experiment was done to investigate the vibrational modes of the carbonate

system.   A reference solution of 3.0 M $KHCO_3$ was made. The experiment was done at

23 ± 2 ^{o}C. Raman spectra were acquired to determine the vibrational frequencies of the

HCO_3^- and CO_3^{2-} species. In addition, the spectrum was examined for the existence of

the H_2CO_3 and CO_2 species. Spectra were acquired with a 30 s acquisition time. Two

spectra were averaged to obtain the final spectrum.

2.6 Solvated CO_2

Solvated CO_2 experiments were done using a pressure range from 8 to 15 atm at

23 ± 2 ^{o}C. The experimental parameters used were outside the CO_2 clathrate forming

region, Figure 2.4. A stainless steel cell (200 mL volume) was filled with 100.0 mL of

nano-pure water (18.2 M$\Omega \bullet$ cm). $CO_{2(g)}$ was bubbled into the stainless steel cell at a

known pressure. Solvated CO_2 spectra were acquired every ten minutes for eight hours. A 4 min integration time was used. At the completion of the experiment, the pressure was then adjusted to obtain solvated CO_2 data at other pressures.

Solvated spectra were also acquired at -15 ± 2 ^{o}C. Since this temperature was within the temperature range to form clathrates, only pressures outside of the clathrate region were used. A pressure range of 5 to 10 atm was used. The cell was moved to the freezer after equilibrium was achieved at 23 ± 2 ^{o}C. Spectra were acquired every ten minutes for ten hours using a 4 min integration time.

2.7 CO$_2$ Clathrate

Once equilibrium was achieved at solvated conditions, the inlet valve on the stainless steel cell was closed so the cell could be removed from the gas flow. The cell was placed in a freezer and was maintained at a temperature of -15 ± 2 ^{o}C. The gas flow was restarted. The pressure was maintained at 15 atm to allow the formation of clathrates. These experimental parameters are within the CO_2 clathrate forming region, Figure 2.4. Spectra were acquired every ten minutes for ten hours using a 4 min integration time.

The above experimental parameters and conditions were adjusted to perform additional experiments to investigate the CO_2 clathrate system. For one experiment, a magnetic stirrer was added to the system. For another experiment, the volume of H_2O was decreased from 100 mL to 75 mL.

A series of experiments were done by warming and cooling the stainless steel cell over a period of three days. The cell was originally at 23 ± 2 ^{o}C and maintained at 7 atm for ten hours. The cell was then cooled to -15 ± 2 ^{o}C and remained in the freezer for an

14

additional ten hours. The pressure was then increased to 15 atm and the cell was slowly

warmed to 0 ± 2 $^{\circ}$C and was maintained at these pressure and temperature conditions

during spectral acquisition. The pressure was maintained for the duration of the

experiment. The cell was cooled back down to -15 $\pm$ 2 $^{\circ}$C. This series of warming and

cooling was repeated six times.

2.8 H_2O

A sample vial of nano-pure $H_2O_{(l)}$ (18.2 M$\Omega \bullet$ cm) was made. It was maintained

at 1 atm and 23 $\pm$ 2 $^{\circ}$C. A Raman spectrum of the stretching region (2900-3700 cm^{-1}) and

the bending region (1500-1800 cm^{-1}) was acquired using an integration time of 60 s. A

pure $H_2O_{(l)}$ spectrum of both the stretching and bending region was acquired of the

stainless steel system prior to being exposed to CO_2. It was maintained at 15 atm and 23

$\pm$ 2 $^{\circ}$C. During the solvated CO_2 experiment, the bending mode was observed in the

spectral window. Since the stretching region was not included in the spectral windows,

the stretching region of H_2O was acquired at the end of the solvated CO_2 experiment.

When the stainless steel cell was placed in the freezer to acquire CO_2 clathrate

spectra, the sample vial was also placed in the freezer. Both systems were maintained at

-15 $\pm$ 2 $^{\circ}$C but the sample vial was at 1 atm while the cell was at 15 atm. The bending

region was acquired with CO_2 clathrate spectra. The stretching region was taken at the

end of the CO_2 clathrate experiment.

2.9 Data Analysis

All spectra were evaluated using Igor Pro (Wavemetrics, Version 4.0.5.1). A

graphing macro (Appendix C), written by Dr. Laura Voss and Lisa Van Loon of the

Allen lab, loaded individual spectra into one graph and table. The spectra were fit with a

Voigt function. The peak positions, areas, and FWHM of the Fermi diads were determined using built-in functions.

2.10   Experimental Controls

The laser energy stability and peak shifts of naphthalene and solvated CO_2 peak used to test the stability of the laser system during the experiments. The laser energy was read with a laser power meter (Molectron Detector Inc., Power Max 500D) before and after acquiring spectra to verify energy stability. The energy varied by ± 5 mW during the course of the experiment. It was determined during another experiment (Appendix A) that the laser energy was not destructive to the sample. A naphthalene spectrum was acquired prior to and after obtaining solvated CO_2 spectra as well as at the end of the experiment. The 1382 cm^{-1} peak of naphthalene was evaluated for shifts in peak position. Throughout the experiment, the peak shifted less than 1 cm^{-1}. Solvated CO_2 spectra were evaluated over a period of ten hours to determine if the peak would shift as a function of time. The peak shifts observed for both Fermi diads were less than 1 cm^{-1}. Therefore, any peak shift greater than 1 cm^{-1} observed during the clathrate experiment is real and is not attributed to instrument fluctuations.
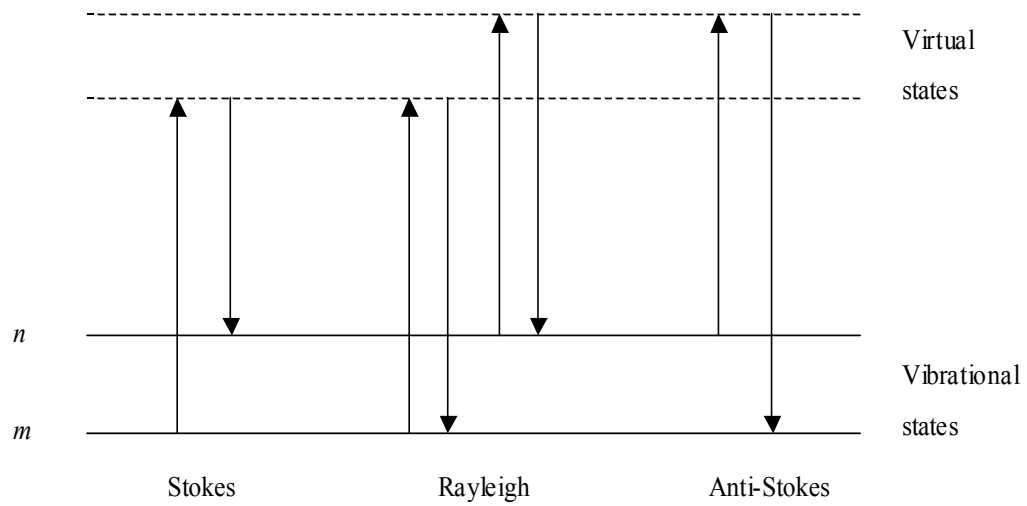
Figure 2.1: Diagram of the Rayleigh and Raman scattering processes. The lowest energy vibrational state *m* is shown at the bottom. States of increasing energy are above state *m*.

$v_s = 1337$ cm^{-1} $v_{as} = 2349$ cm^{-1} $\delta_d = 667$ cm^{-1}

v_1 v_3 v_2

Raman Active   IR Active   IR Active
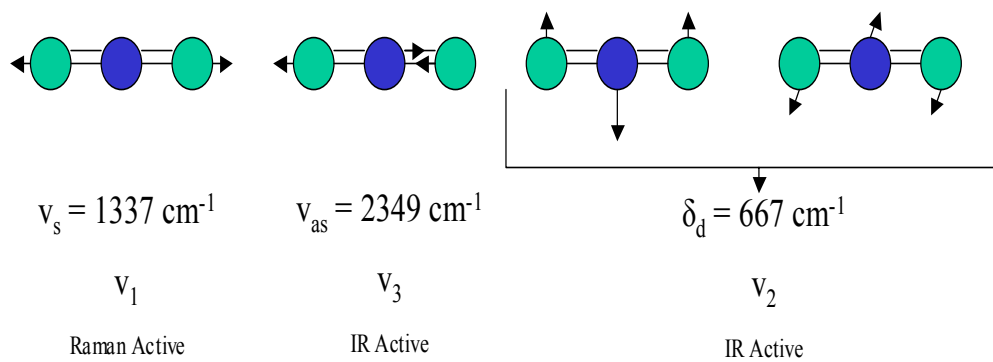
Figure 2.2: The fundamental vibrational modes of CO$_2$ are shown with their vibrational energies, where v_s is the symmetric stretch, v_{as} is the asymmetric stretch, and δ_d is the doubly degenerate bending mode.
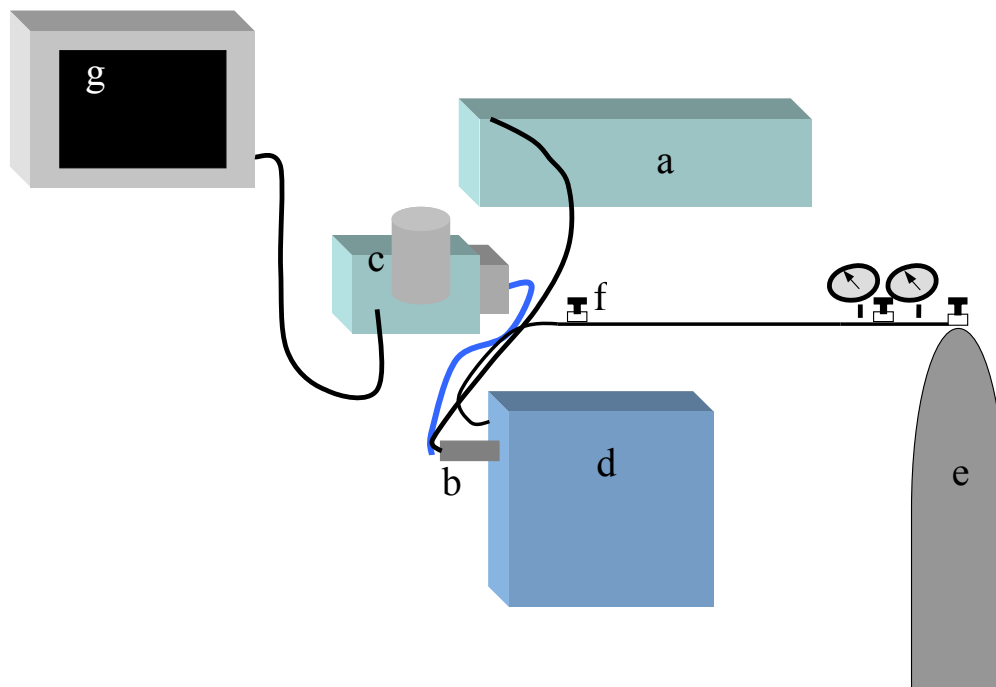
Figure 2.3: Schematic of Raman setup for obtaining CO_2 clathrate spectra: a) Spectra-Physics Millenia II laser; (b) fiber optic Raman probe; (c) monochromator; (d) freezer; (e) CO_2 tank; (f) gas inlet valve; (g) computer
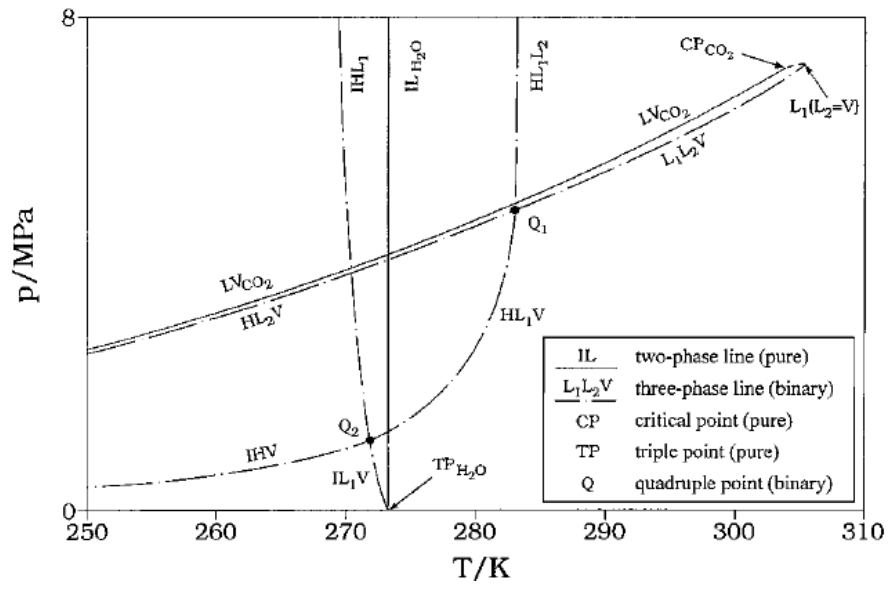
Figure 2.4: Schematic pressure-Temperature diagram of the carbon dioxide-water system at 250-310 K.[68]

CHAPTER 3

RESULTS AND DISCUSSION

3.1 Gaseous CO_2

The Raman spectrum of $CO_{2(g)}$ is shown in Figure 3.1. This spectrum is composed of two major peaks assigned to the Fermi diads and two minor peaks attributed to hot peaks. The Fermi diads are at 1285 cm^{-1} and 1387 cm^{-1} and will be called the SS-FD and $2\nu_2$-FD, respectively. The assignments of the Fermi diads use the vibrational mode that is the major contributor to the observed peak. This assignment will be discussed in more detail later. The two hot bands are at 1264 cm^{-1} and 1409 cm^{-1}.

As discussed in Chapter 2, there are four fundamental modes of CO_2. Only the symmetric stretch (ν_1) is Raman active and it has an observed Raman shift of 1334 cm^{-1}. However, the first overtone of the bending mode ($2\nu_2$) is also allowed in the Raman spectrum. Since the bending mode occurs at 670 cm^{-1}, the first overtone occurs at 1340 cm^{-1}. The intensity of the overtone is generally less than one tenth the intensity of its fundamental transition[34] because it is dependent on the anharmonicity of the molecule's polarizability as well as the vibrational potential.

In the case of CO_2, the vibrational wave functions of both the symmetric stretch and the first overtone have nearly the same vibrational frequencies. In addition, both

vibrational wave functions have the same symmetry (σ_g^+).[33,34] The combination of the

similar frequency and symmetry leads to a perturbation of the energy levels.[33-37] The

levels split forming new energy levels that are a combination of the symmetric stretch

level and the overtone level. A "mixing" of the two energy levels occurs, and the weak

overtone "borrows" intensity from the nearby fundamental. As a result, two strong

peaks, the Fermi resonances, are observed at 1388 cm^{-1} and 1286 cm^{-1}.[36,34,33,17] Although

the energy levels are perturbed, both levels contain some of the properties of the original

two levels.[36] Fermi resonance is not special to CO_2. It is observed in many molecules

and especially in large molecules of low symmetry.[36]

In the Raman spectrum of CO_2, the hot bands are weak in intensity compared to

the Fermi diads. The Boltzmann distribution predicts this weak intensity. Unlike a

fundamental transition, the lower level of a hot band is an excited state. According to

Equation 2.2, the likelihood of an excited state being occupied is low at thermal

equilibrium. Therefore, the hot bands observed in the spectrum are of weak intensity.

3.2 The Carbonate System

When H_2O is exposed to CO_2, reactions occur in addition to the solvation of CO_2.

To investigate the possibility of the formation of other species, a reference spectrum of a

3.0 M $KHCO_3$ solution is compared to the solvated CO_2 spectrum. Both systems are

maintained at 23 $^{\circ}C$. The solvated CO_2 system is held at 12 atm and the reference

solution is held at 1 atm. The most prominent peak of the reference spectrum is a large

peak at 1014 cm^{-1}(Figure 3.2). This peak is assigned to the C-OH stretch of HCO_3^-. The

small peak at 1061 cm^{-1} corresponds to the C=O symmetric stretch of CO_3^{2-}. The broad

region between 1200 and 1450 cm^{-1} reveals two peaks. The weaker peak at 1300 cm^{-1} is

attributed to the C-OH bending mode of HCO_3^- while the stronger peak at 1359 cm^{-1} corresponds to the C=O symmetric stretch of HCO_3^-.[25,38,39] Table 3.1 includes the vibrational assignments observed. There is no spectroscopic evidence of H_2CO_3. Also, no CO_2 Fermi diads are observed in the reference solution. This is expected due to the low pressure used.

The large intensity of the three peaks attributed to HCO_3^- compared to the peak attributed to CO_3^{2-} indicates a large concentration of HCO_3^- exists in the reference solution. These results are supported by the acid equilibrium constants of the system. Refer to Chapter 2 for the reactions of the carbonate system. The reaction forming H_2CO_3 from HCO_3^- has an equilibrium constant of 2.25 x 10^{-8} (calculated).[17] The reaction of HCO_3^- to form CO_3^{2-} has an equilibrium constant of 4.84 x 10^{-11}.[17] The smaller equilibrium constant for the formation of CO_3^{2-} indicates the formation of CO_3^{2-} is favored over H_2CO_3. Therefore, obtaining spectroscopic evidence of CO_3^{2-} and HCO_3^- and not H_2CO_3 is reasonable.

The peaks attributed to CO_3^{2-} are of weaker intensity than that of HCO_3^-. This intensity difference is attributed to the lower concentration of CO_3^{2-} (3.76 x 10^{-2} M) compared to the HCO_3^{2-} concentration (3.0 M). In addition, the equilibrium constants indicate CO_3^{2-} is favored over H_2CO_3. However, H_2CO_3 does exist in the solution with a concentration of 2.63 x 10^{-4} M. Since the H_2CO_3 concentration is below the Raman detection limit of 10^{-2} M, it will not be observed in the spectrum.

3.3 Aqueous CO_2

In the solvated CO_2 Raman spectrum, two peaks are observed at 1275 cm^{-1} and 1382 cm^{-1} (Figure 3.2). Table 3.1 includes the solvated CO_2 vibrational assignments.

These peaks are attributed to the Fermi diad peaks of solvated CO_2. The peak at 1165 cm^{-1} is an artifact of the silica window. No other peaks are observed. This observation indicates the system favors $CO_{2(aq)}$ over carbonic acid. These results are supported by a large rate constant of k = 2.63 x 10^2 s^{-1} for the formation of H_2CO_3 from $CO_{2(aq)}$.[25] At room temperature, ~99.8% of the dissolved CO_2 remains as $CO_{2(aq)}$ while only ~0.2% reacts with water to form H_2CO_3.[17,26,2] The high pressure used in our clathrate experiments is not enough to shift the reaction toward a detectable concentration of H_2CO_3. At 15 atm, the concentration of H_2CO_3 is 6.05 x 10^{-4} M, which is below the Raman detection limit of 10^{-2} M. Experimental data (not shown) obtained at pressures close to atmospheric pressure do not show any peak attributed to the carbonate system, including $CO_{2(aq)}$, since the concentrations are below the Raman detection limit. This observation is supported by the need for high pressures to obtain observable CO_2 concentrations in water.[25]

Solvated CO_2 Raman spectra are taken after CO_2 is bubbled into the cell containing H_2O (Figure 3.3). Spectra are acquired every ten minutes for ten hours. The two peaks observed at 1275 cm^{-1} and 1382 cm^{-1} are the Fermi diads of CO_2 as seen in the $CO_{2(g)}$ spectrum. A dotted line is used to highlight the peak position of the Fermi diads and verifies there is no significant shift during the integration period. For further discussion, see Section 2.J.

The Fermi diads of CO_2 are much broader in water than in the gas phase. The observation of this broadening is an indication that interactions are occurring between the CO_2 and H_2O molecules. If hydrogen bonding was involved in the solvated phase, the restrictions placed upon the CO_2 molecule by the strong hydrogen bonds could break the

symmetry of CO_2 found in the gas phase. If the symmetry was broken, the Fermi diads would no longer be observable. Instead, a weak peak and a strong peak attributed to the first overtone and the symmetric stretch, respectively, would be observed. If upon hydration one of the vibrational modes has a significant change in frequency, the vibrational energy levels would be shifted farther apart. This shift would reduce the perturbation of the energy levels resulting in an increase in the level separation and reducing the intensity effect. An *ab initio* study computed the C-O bond lengths to be 1.176 Å and 1.177 Å in the gas phase and aqueous phase, respectively.[40] The small difference in the bond length of the different phases is in agreement with the small change observed in the Fermi diads as a result of hydration. *Ab initio* studies also show the clathrate CO_2 molecule prefers the same symmetry as that of its gaseous state, $D_{\infty h}$.[40] Therefore, the symmetry is not broken during the transition from the gaseous state to the aqueous state.

The hot bands observed in the $CO_{2(g)}$ spectrum are not observed in the solvated CO_2 spectrum. The intensity ratio of the SS-FD in the gas phase to the aqueous phase is 22.5. In the gaseous phase, the intensity ratio of the SS-FD to the lower frequency hot band is 18.7. Assuming the ratio between the SS-FD and the lower frequency hot band is the same for the aqueous phase as that of the gaseous phase, the hot band should have an intensity of 52.7 A.U. This low intensity is below the detection limit of 570 A.U.

The decrease in intensity of the Fermi diads observed in the aqueous phase is of great importance. Since Raman intensity is proportional to concentration, the number of molecules of CO_2 will be determined for both phases at a pressure of 10 atm and a temperature of 25 °C. In the gaseous phase, the ideal gas law is used to determine the

number of molecules of CO_2 in the cell. In the aqueous phase, Henry's law is used to calculate the number of molecules in solution. It is determined that there are 4.96 x 10^{22} molecules in the gas phase compared to 1.87 x 10^{22} molecules in the aqueous phase. To compare the intensities of the Fermi diads in the gas phase to the aqueous phase, the gas phase intensities are corrected by using the concentration ratio of CO_2 in the aqueous and gas phases. As shown in Figure 3.4, correcting the gas phase intensities for the concentration difference did not result in the Fermi diads being of the same intensity. Since a large intensity difference still remains, the concentration difference between the two phases is not the only factor for the diminished intensity of the Fermi diads. This observation is an indication that the CO_2 molecules are interacting with the surrounding water molecules.

When $CO_{2(g)}$ is exposed to liquid water at 23 ^{o}C, the peak intensity of the CO_2 Fermi diads increases for up to six hours, indicating that the concentration of CO_2 molecules in water is increasing. In Figure 3.5, the peak area and peak intensity of the $2\nu_2$-FD are shown over a period of six hours. The SS-FD is not observed initially due to a low S/N ratio. For the first three hours, CO_2 dissolves rapidly in water before slowly leveling off. Equilibrium is reached in the system in approximately six hours.

3.4 CO_2 Clathrate

In Figure 3.6, a CO_2 clathrate spectrum and a solvated CO_2 spectrum are compared. Dashed lines are used to highlight the peak positions of the solvated CO_2 Fermi diads. Figure 3.7shows the spectral fits and raw data used to determine the peak shifts and FWHM of the Fermi diads. Table 3.3 shows the calculated values for the peak position, area, and FWHM for the Fermi diads. The Fermi diads of solvated CO_2 are at

1278.2 cm^{-1} and 1386.2 cm^{-1}. The Fermi diads of CO_2 clathrates are at 1280.5 cm^{-1} and

1384.7 cm^{-1}. Vibrational assignments for CO_2 clathrate are included in Table 3.1. A

small blue-shift of 1.8 cm^{-1} occurs for the SS-FD from solvated to clathrate phase, and a

small red-shift of 1.7 cm^{-1} occurs for the $2v_2$-FD. With respect to the solvated Fermi

diads, the observed blue-shift and red-shift for the SS-FD and $2v_2$-FD, respectively, are

reported in the literature as a sign of CO_2 clathrate formation.[41]

As the spectrum shows in Figure 3.5, the Fermi diads are not further split. This is

an important observation since splitting of the peaks would indicate that CO_2 is

partitioned between the small (5^{12}) and large ($5^{12}6^2$) cavities of sI.[15,19,42] For example, the

stretching mode of CH_4 is split in the clathrate phase because it occupies both cavities of

sI. Raman and NMR studies confirm CO_2 occupies only the large cavity of sI.[42]

The shift in the Fermi diads shows that the clathrate cage affects the vibrational

modes of CO_2. Interestingly, one Fermi diad is blue-shifted while the other is red-shifted.

Therefore, the clathrate cage has a different effect on the individual vibrational modes

that make up the Fermi diad. The $2v_2$-FD is dependent upon the first overtone of the

bending mode ($2v_2$).[32,43] Any changes observed in the frequency of the overtones of the

bending mode are a direct result of how the bending mode is affected by its environment.

Therefore, to completely understand the red-shift of the Fermi diad at 1383 cm^{-1} the

bending mode frequency is briefly discussed. The bending mode is IR active only and

occurs in the gas phase at 667 cm^{-1}.[44] The gas spectrum shows the bending mode

frequency decreases with clathrate formation. The decrease in frequency would then

cause the overtones to also decrease in frequency. On the other hand, the SS-FD

increases in frequency. The SS-FD is heavily dependent upon the symmetric stretch

27

(v_1).[32,42] This increase indicates the bonds involved in the symmetric stretch become stronger with the formation of clathrates.

Although the Fermi diads shift when transitioning from the aqueous to the clathrate phase, the effect is small. If stronger interactions, such as hydrogen bonding, occurred between the CO_2 molecules and the H_2O molecules composing the clathrate cage, the shift would be appreciably greater. As a result of hydrogen bonding, both Fermi diads would red-shift as the strong intermolecular interactions would weaken the CO_2 vibrational modes. In addition, the existence of the Fermi diads indicates there is no break in symmetry, which could also occur with the restrictions placed upon the vibrations of CO_2 if there was hydrogen bonding. In addition, CO_2 in the solid phase is held together primarily by weak van der Waals forces. The Fermi diads of the solid phase are 1276 cm^{-1} for the SS-FD and 1384 cm^{-1} for the $2v_2$-FD.[45] In the solid phase, the SS-FD is red-shifted by 8 cm^{-1} and the $2v_2$-FD is red-shifted by 3 cm^{-1}. Both shifts are larger than that in the aqueous phase and the clathrate phase. Therefore, any intermolecular interactions between the CO_2 molecule and the clathrate cage must be weak. This data is evidence that the forces required to prevent the clathrate cage from collapsing are van der Waals forces, which is assumed in the VDW-P model.[19,21,22,41]

The peak shift of both Fermi diads can be observed in Figure 3.8. Both Fermi diads shift when transitioning from the solvated phase to the clathrate phase. At low pressure (5 atm), the positions of both peaks do not shift significantly indicating that clathrates do not form under these conditions. The CO_2 phase diagram (Figure 2.4) illustrates that these conditions are not within the clathrate phase. With a pressure increase (15 atm) and temperature decrease (-17 ^{o}C), a significant increase and decrease

28

in the peak positions are observed for the SS-FD and $2v_2$-FD, respectively. At -17 $^\circ$C and

15 atm, the phase diagram conforms that the experimental conditions are favorable for

clathrate formation. As the system is warmed up to 22 $^\circ$C, the peaks shift back to the

position attributed to solvated CO_2. This trend is observed each time the system is

cooled and warmed.

The FWHM has been evaluated for both Fermi diads in the aqueous and clathrate

phases and are shown in Figure 3.9. In the aqueous phase, the FWHM of the Fermi

diads are much wider than that in the clathrate phase with the FWHM of the SS-FD and

$2v_2$-FD being on average 13 and 19 cm^{-1}, respectively. However, in the clathrate phase,

the FWHM of the Fermi diads narrow significantly until both peaks have similar FWHM

of 8 cm^{-1}. The FWHM increases and decreases as the system transitions from the

solvated phase to the clathrate phase and back. A comparison of the FWHM of the Fermi

diads in the gas, aqueous, and clathrate phases are shown in Table 3.2. The broadening

of the Fermi diads in the aqueous phase is the result of interactions between CO_2 and H_2O

molecules. The FWHM in the clathrate phase decreases and is similar to the FWHM of

the Fermi diads in the gas phase. Since the FWHM in the clathrate phase decreases, the

intermolecular interactions between CO_2 and H_2O molecules are weaker in the clathrate

phase than in the aqueous phase and CO_2 is more "gas-like."

Using a cavity model for gas clathrates, consider a CO_2 molecule trapped in a

spherical cavity. The carbon atom of the CO_2 molecule resides at the center of the cavity.

The vibration frequency $v^{'}$ in the cavity can be related to that in a vacuum, v_0, by

Equations 3.3-3.4[41]

$$v^{'}/v_0 = (1/\varepsilon^*)^2 \tag{3.3}$$

$$\varepsilon^* = \frac{1}{c}\int_0^c \frac{db}{1 - \left(\frac{\varepsilon' - 1}{\varepsilon' - 0.5}\right)\left(\frac{b}{a}\right)^3} \tag{3.4}$$

where b is an arbitrary radius from the center of the cavity and c is the interatomic distance between carbon and oxygen in CO_2. The radius between CO_2 and H_2O was calculated to be 2.50 Å and 3.07 Å in the aqueous phase and the clathrate phase, respectively.[41] These calculations suggest that CO_2 molecules in the aqueous phase are closely surrounded by H_2O molecules but formation of clathrates increases this spacing. Therefore, it is reasonable to suggest the decrease in the FWHM upon clathrate formation is due to decreased intermolecular interactions.

In all the phases, the combinations of the peak shifts, FWHM, and intensity changes of the Fermi diads of CO_2 indicate the vibrational modes are sensitive to their surroundings. The decrease in wavenumber separation between the two Fermi diads in the clathrate spectrum suggests that the vibrational energy levels are perturbed more than they are in the aqueous phase. Using a perturbation model, the unperturbed theoretical bending mode and symmetric stretch mode frequencies in the gas, aqueous, and clathrate phases can be calculated for Equations 3.5-3.7.[41,46] The unperturbed frequencies can be thought of as the normal mode frequency if there was no interaction between them. The perturbed frequencies are the frequencies of the Fermi diads in the spectra. Table 3.3 includes the theoretical frequencies of normal modes.

$$v_1 = 0.5(v_1 + v_u) - 0.5\Delta \tag{3.5}$$

$$v_2 = 0.5(0.5(v_1 + v_u) + 0.5\Delta) \tag{3.6}$$

$$\Delta^2 = X^2 - 4W_{10^00-02^00}{}^2 \tag{3.7}$$

30

In Equation 3.7, Δ is the theoretical separation between the unperturbed vibrational levels, X is the experimentally observed frequency separation of the two components and W, the Fermi coupling constant for CO_2, is -50.98 cm^{-1} in the literature.[35] Using the perturbed frequencies observed in the Raman spectrum, the unperturbed frequencies, ν_1 and ν_2, of the aqueous phase are calculated to be 1314.4 cm^{-1} and 675.0 cm^{-1}. For the clathrate phase, they are calculated to be 1321.9 cm^{-1} and 671.6 cm^{-1}, respectively. In the gas phase, the values are 1334.6 cm^{-1} and 669.4 cm^{-1}. In addition, the solid phase perturbed frequency separation was determined to be 108 cm^{-1}.[45] This distance is slightly larger than the perturbed frequency separation of the aqueous phase (107.1 cm^{-1}). Since CO_2 molecules in the solid phase undergoes weak van der Waals interactions with the neighboring CO_2 molecules,[45] this suggests the interactions in both the clathrate and aqueous phases are weakly interacting with the surrounding H_2O molecules via van der Waals forces. In the clathrate phase, the separation between the unperturbed frequencies decreases from that of the aqueous phase and approaches the smaller separation found for the gas phase. These results show the CO_2 molecules in the aqueous phase are experiencing more interactions with the surrounding water molecules than when in the clathrate phase. Therefore, CO_2 is more "gas-like" in the clathrate phase than in the aqueous phase.

There is a significant decrease in intensity in the Fermi diads when clathrates form, Figure 3.10. This decrease is not supported by all the literature,[41,46] but clathrate formation has been found to be highly dependent on the apparatus setup and experimental conditions,[19] and is possibly due to the clathrate nucleation site. Nucleation is the initial stage of a phase transition and the kinetics of nucleation often control the selection of the

dominant kinetic path.[47] Therefore, it is critical to understand where nucleation occurs. In condensed phases, nucleation leads to the spontaneous formation of small, unstable clusters of a new crystalline phase.[22,47]

A cluster nucleation hypothesis was developed by Sloan et al. to explain the clathrate nucleation.[22,48] Water molecules form clusters around dissolved guest molecules. Cluster size is dependent on the guest molecule size, and for CO_2, 24 water molecules are required. The clusters then form unit cells. Coordination numbers of 20 (5^{12}) and 24 ($5^{12}6^2$) are required to form sI. If the liquid phase has clusters of only one coordination number, nucleation is not allowed until the clusters rearrange to make the needed size. Breaking and making hydrogen bonds are required for this process. For the sI clathrate, CO_2 only occupies the large cavity. Since the large cavity coordination number is the same as that preferred for CO_2 clusters, clathrate formation will result in the transformation of the $5^{12}6^2$ cavity into the 5^{12} cavity. Therefore, the rate limiting step in CO_2 clathrate formation is the transformation of the large cavity into the small cavity.[49,15]

The time of clathrate nucleation has not been predictable in bulk experiments, but the clathrate formation has always initiated at a surface, most commonly the vapor-water interface.[21,22] The vapor-water interface is favored for clathrate formation because of the large concentration of both the host and guest molecules. These large concentrations are required for clusters to grow to the supercritical size required for nucleation to occur.[22]

Since the bulk liquid phase contains a small concentration of guest molecules compared to that at the interface, there is little nucleation in the bulk phase. As Raman spectroscopy probes the bulk phase of the system, the experimental setup will greatly

determine the observed vibrational modes. Variations of the clathrate experiment were

done to evaluate if the Fermi diads would change in intensity as a result of the setup used.

Figure 3.11 shows the Raman spectrum acquired during these altered experiments. A

smaller volume of water was used to lower the vapor-water interface. By lowering the

interface closer to the area probed, it was believed an increase would occur in the

intensity of the Fermi diads due to a larger concentration of clathrates. When a volume

of 75 mL was used, the interface was 0.2 cm above the probed area compared to the 1.0

cm distance when using the 100 mL. However, this was not the case as there was no

difference between this spectrum and the spectra using a larger water volume. In

addition, a magnetic stirrer was used to stir the solution while cooling. This would allow

for better mixing of the interfacial gas, liquid, and crystal structures within the liquid.[22]

Therefore, the intensity of the Fermi diads would increase due contribution from "bulk

nucleation." The intensity of the peaks did not change indicating there is another reason

complete conversion to clathrates is not observed.

Figure 3.12a shows the peaks decrease steadily for two hours before intense

peaks attributed to the clathrate phase form. Once the clathrates form (Figure 3.12b), the

intensity does not change, which indicates complete conversion to the clathrate structure.

However, it also takes two hours for the solution to freeze. It is suggested that the frozen

solution greatly reduces the rate of clathrate formation. To maximize clathrate formation,

the solution was allowed to reach equilibrium before being cooled to equilibrium to

saturate the solution with CO_2. When starting with a saturated solution, clathrate growth

is diffusion controlled. When ice forms, the process is still controlled by the diffusion

rate of CO_2 molecules through the accumulating clathrate layer.[50] The rate of formation

has been shown to increase significantly at higher temperatures when a quasi-liquid layer forms.[50,51] Almost complete conversion (~98%) to the clathrate phase is observed when the temperature is raised near the melting point of ice (-10 to 0 $^{\circ}$C).[50,51] For solutions where the availability of CO_2 is sufficiently high, the temperature in these experiments is the main limiting factor.[52] Since the system is allowed to reach equilibrium before cooling, the significant decrease in intensity of the Fermi diads is attributed to the temperature being the limiting factor. Therefore, the decreased intensity of the Fermi diads indicates the temperature is hindering complete conversion from the aqueous system to clathrates.

In addition, increased light scattering occurs with a crystalline substance. Since the solution is now frozen, the decrease in intensity can be attributed to increased scatter from hexagonal ice and the clathrate cavities. Therefore, the decreased intensity of the Fermi diads could be attributed to several factors, such as the experimental setup or increased scatter.

3.5 Pure Water vs. Solvated

A comparison between pure water and water in a CO_2 solvated environment has been done to evaluate the affect of the addition of CO_2 on the water structure. Both systems are at 23 $^{\circ}$C. The pure water system is at 1 atm and the CO_2 solvated system is at 15 atm. The different pressures used for acquiring the pure and solvated spectra will not be of major consequence as the mole fraction ratio of water is 1.01. The stretching region, Figure 3.13a, is fit with three peaks at 3291 cm^{-1}, 3459 cm^{-1}, and 3640 cm^{-1}. The peak at 3291 cm^{-1} is attributed to the symmetric vibrational modes from the four oscillating dipoles associated with four-coordinate, hydrogen-bonded water molecules.

34

The peak at 3459 cm^{-1} is attributed to the more asymmetrically oscillating dipoles from four-coordinate hydrogen-bonded water molecules, and one hydrogen is a poor hydrogen bond donor. The peak at 3640 cm^{-1} is assigned to the modes associated with three-coordinate asymmetrically hydrogen-bonded water molecules where one OH bond is involved in strong hydrogen bonding and the other is weakly hydrogen-bonded.[53] The peak at 1600 cm^{-1} (Figure 3.13b) is attributed to the bending mode of H-O-H. In the case of solvated CO_2, the stretching and bending region are both identical in peak position and intensity to that of pure water. The stretching region remains unchanged during the addition of CO_2, suggesting that CO_2 does not form hydrogen bonds with H_2O molecules.[54]

3.6 Ice vs. Clathrate

A study was done to investigate the CO_2 clathrate structure. Hexagonal ice, which forms at the same conditions that were used to form clathrates, will be used to compare structures. Both systems were at -17 $^{\circ}$C. The CO_2 clathrate spectrum was acquired at 15 atm while hexagonal ice was at 1 atm. The different pressures used for acquiring the Ih and clathrate spectra will not be of major significance as the mole fraction ratio of water is 1.01. Figure 3.14a show peaks at 3148 cm^{-1}, 3265 cm^{-1}, and 3379 cm^{-1}. The 3148 cm^{-1} peak dominates the O-H stretching region of Ih. This peak is assigned to H_2O molecules with symmetric stretch vibrations that are all in-phase with each other.[46,55] This peak is attributed to the companion OH to the "free OH."[54] In addition, the 3265 cm^{-1} is attributed to the in-phase O-H stretching motions of a hydrogen bonded aggregate consisting of a central H_2O molecule and its nearest neighbors while the 3379 cm^{-1} is attributed to the O-H stretching motions of the H_2O molecules that lost

the phase relationship.[55] The bending region (Figure 3.14b) shows no significant peak attributed to the bending mode. The stretching and bending region of the CO_2 clathrate are both identical in peak position and intensity to that of Ih. There is no significant difference between the two spectra.

The absence of the bending mode at 1600 cm^{-1} in Figure 18b is due to a mixing of the bending mode of H_2O and the overtone of the librational mode.[56] The librational mode increases significantly with increasing hydrogen bond strength unlike that observed for the symmetric stretch. This indicates the hydrogen bonds of the water structure in the solvated phase strengthen when transitioning to CO_2 clathrates.
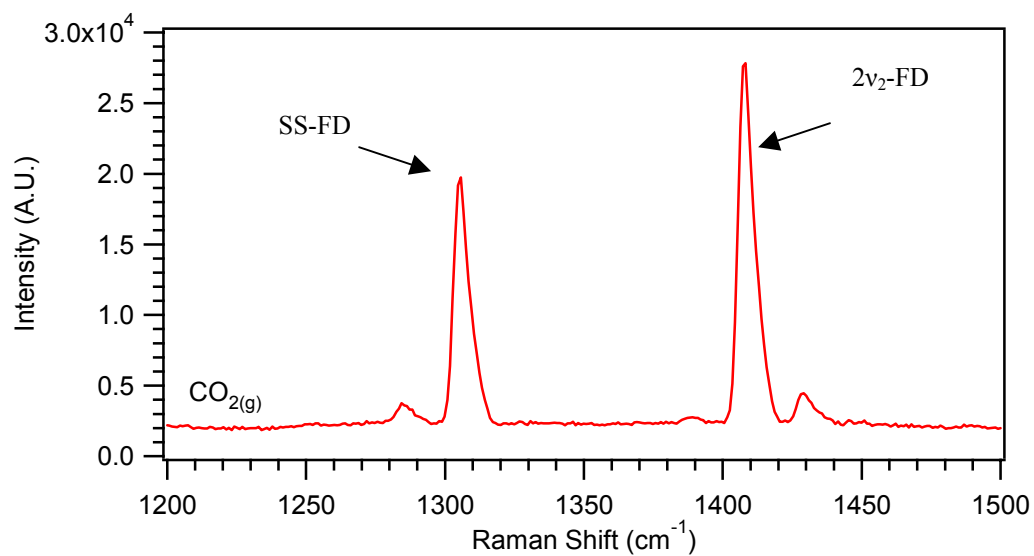
Figure 3.1: The Raman spectrum of $CO_{2(g)}$. The SS-FD is at 1308 cm^{-1} and the $2v_2$-FD is at 1410 cm^{-1}. The hot bands are at 1286 cm^{-1} and 1433 cm^{-1}.
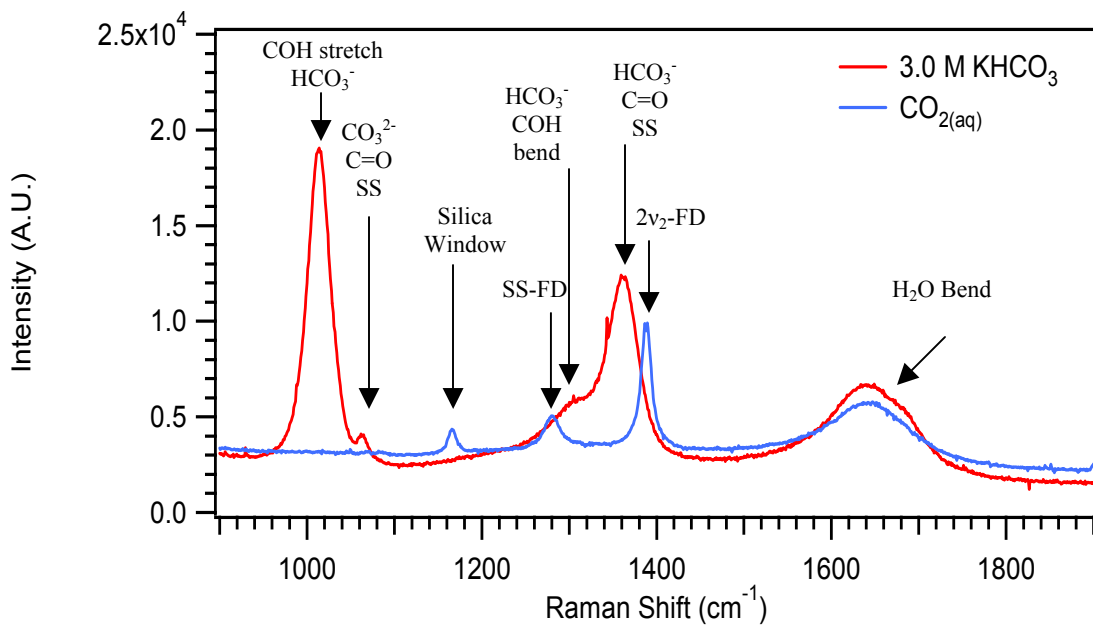
Figure 3.2: The Raman spectra of a 3.0 M KHCO$_3$ solution compared to CO$_{2(aq)}$ at 7 atm. The peak at 1165 cm^{-1} is an artifact of the silica cell window. There are two bands associated with the Fermi diad of CO$_{2(aq)}$ at 1275 cm^{-1} and 1382 cm^{-1}. The broad band at 1630 cm^{-1} is due to the bending mode of H$_2$O. The band at 1014 cm^{-1} is the C-OH stretch of HCO$_3^-$, at 1061 cm^{-1} is the C=O SS of CO$_3^{2-}$, at 1300 cm^{-1} is the C-OH bending mode of HCO$_3^-$, and at 1359 cm^{-1} is the C=O SS of HCO$_3^-$.
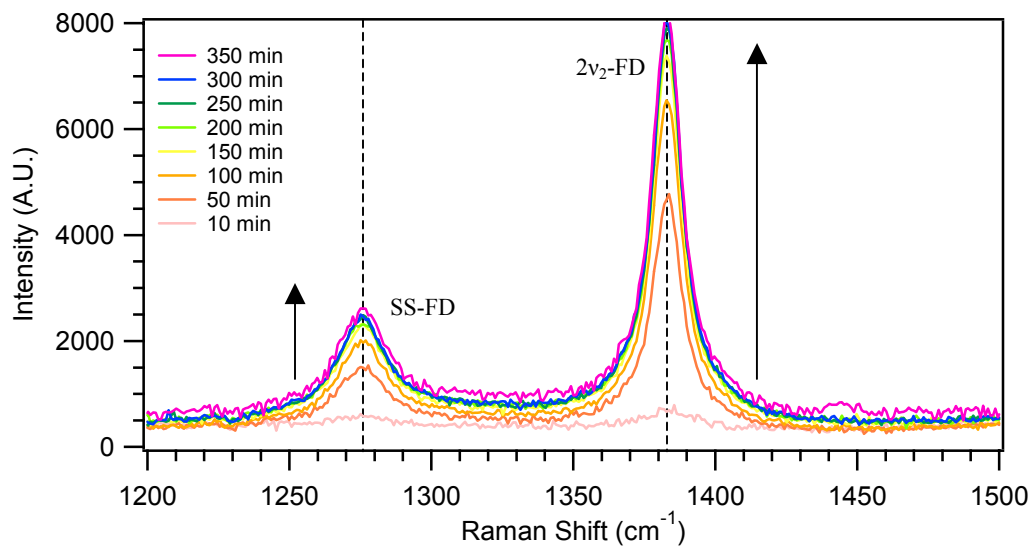
Figure 3.3: Raman spectra showing the growth of the aqueous CO_2 Fermi diads when exposed to H_2O. The peaks increase rapidly with initial exposure. Equilibrium is reached after 7 hours. The spectra are acquired at $23 \pm 2\ ^0C$ and a pressure of 15 atm.
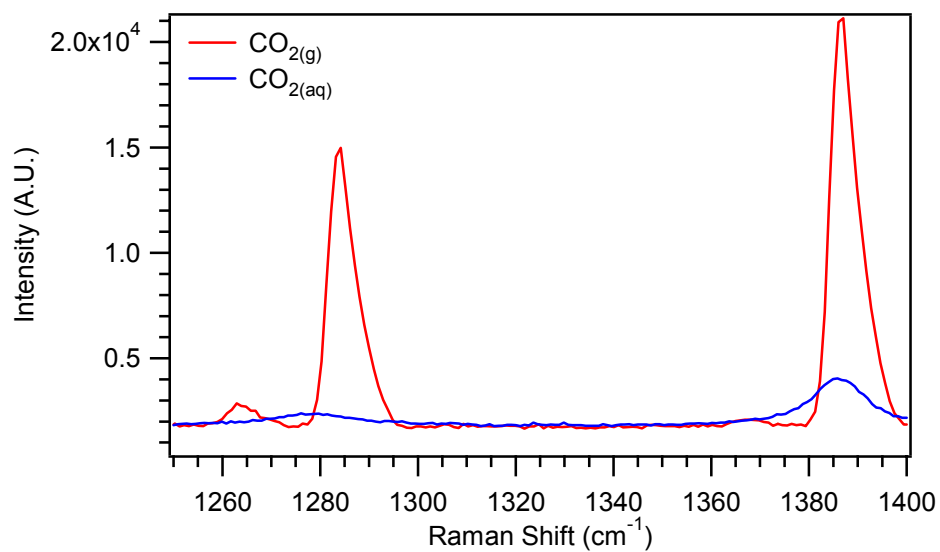
Figure 3.4: The CO$_{2(g)}$ spectrum after adjusting the intensity by the concentration ratio of 1.32. The original CO$_{2(aq)}$ spectrum is shown.
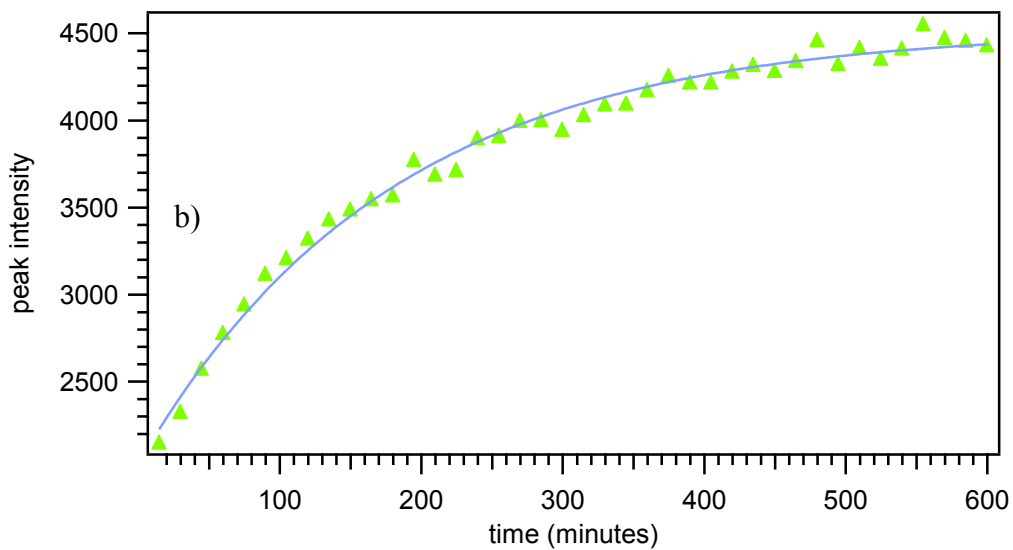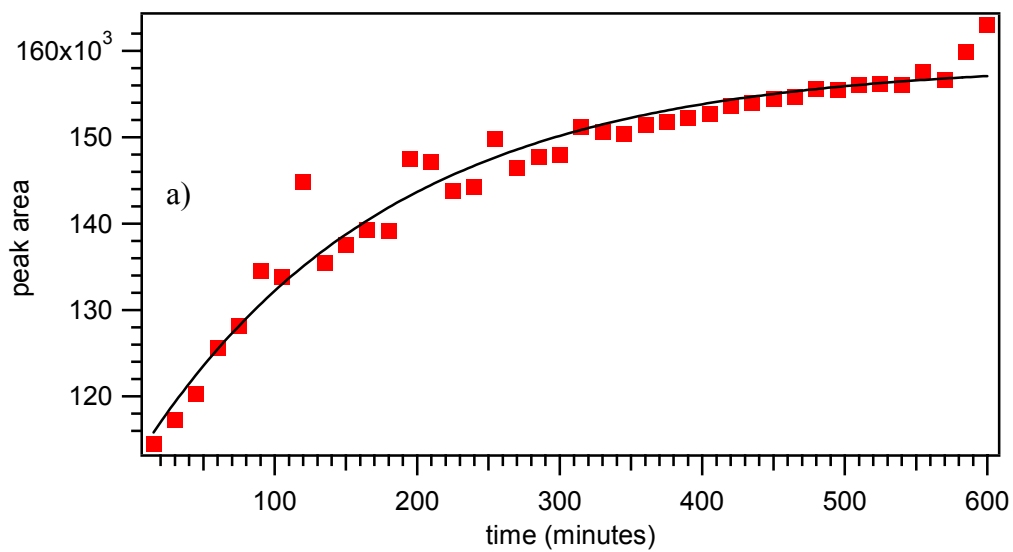
Figure 3.5: Analysis of the $2v_2$-FD of CO_2 upon exposure to H_2O as a function of time: (a) is the peak area and (b) is the peak intensity as a function of time.
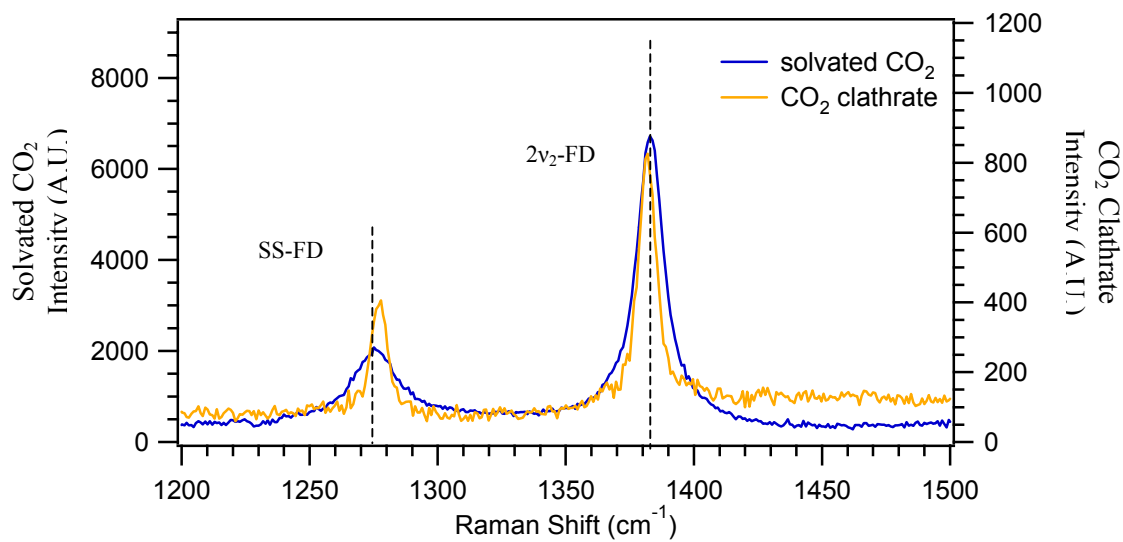
Figure 3.6: A comparison of solvated CO_2 and CO_2 clathrate spectra. The solvated CO_2 Fermi diad peak positions are highlighted with a dotted line to guide the eye to the peak shift that occurs when clathrates form. The solvated CO_2 spectrum is acquired at 15 atm and $23 \pm 2\ ^0C$. The CO_2 clathrate spectrum is acquired at 15 atm and $-17 \pm 2\ ^0C$.

42
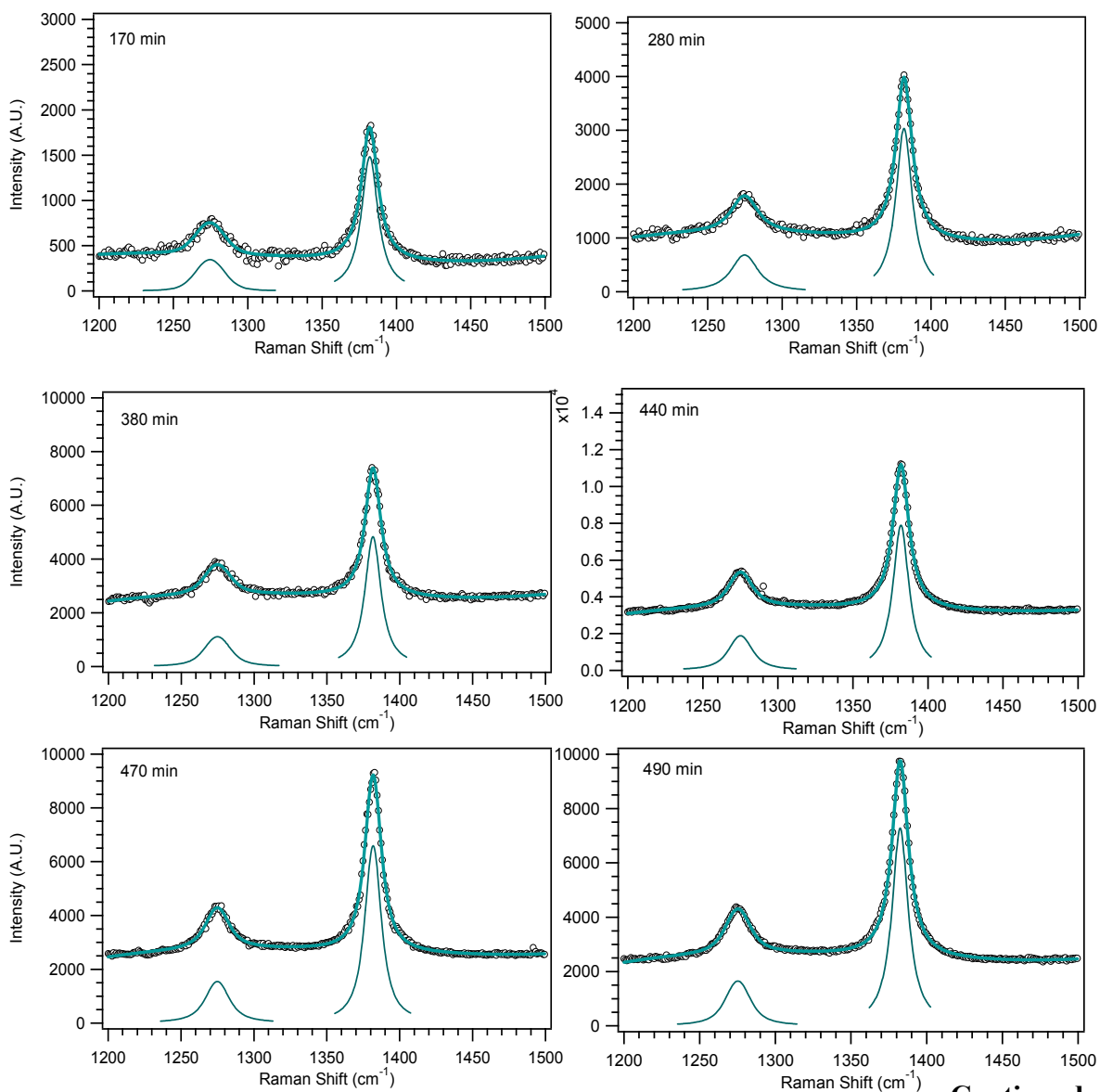
Figure 3.7: Spectral fits of the Raman spectra at various conditions during the 3600 min (3 day) experiment. The fits were used to determine the FWHM and peak shift data. The time range shown. Component peaks are shown in green as are the calculated fits. Raw data are shown as black circles.

43
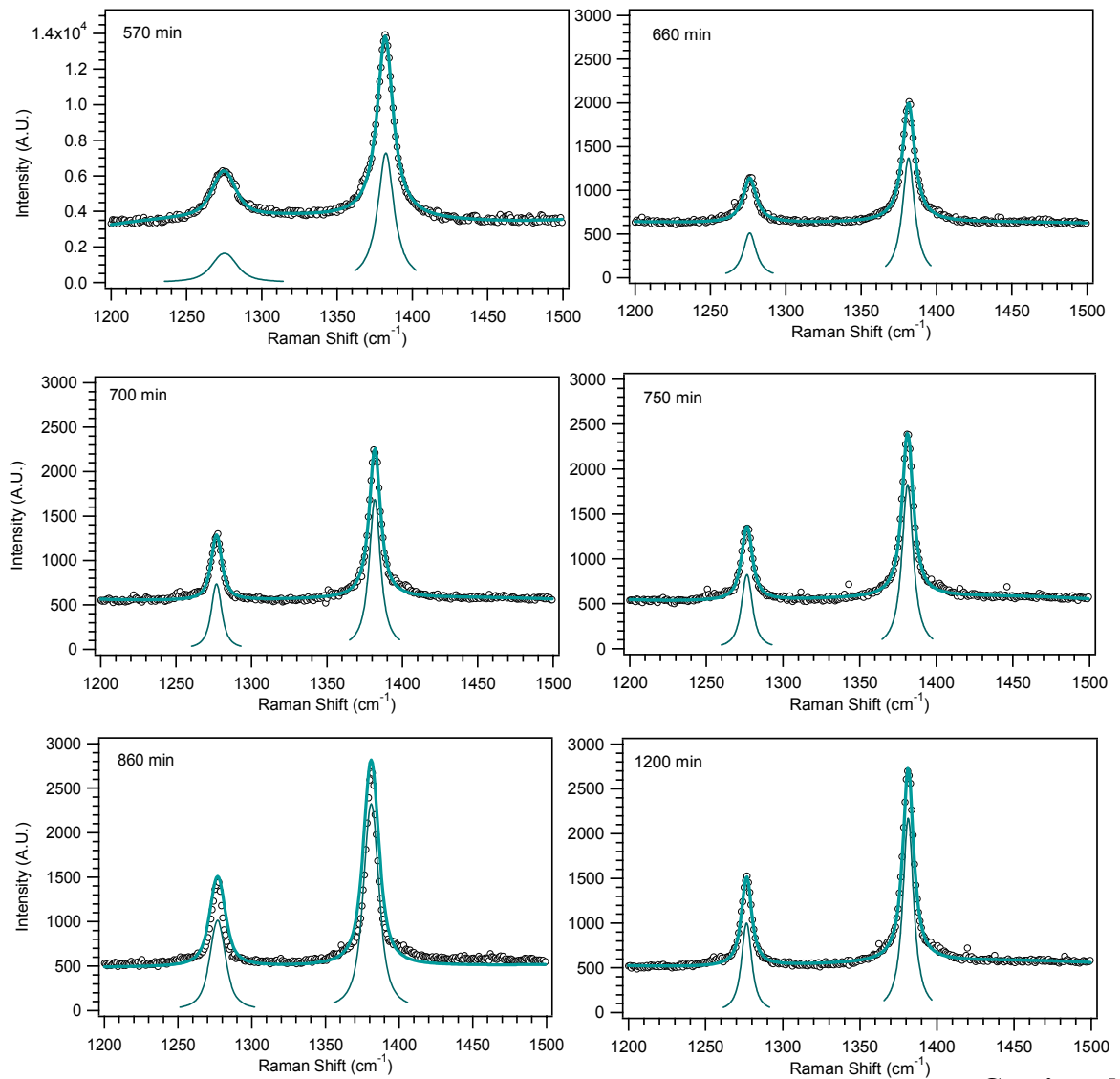
Figure 3.7 Continued

Figure 3.7 Continued

45
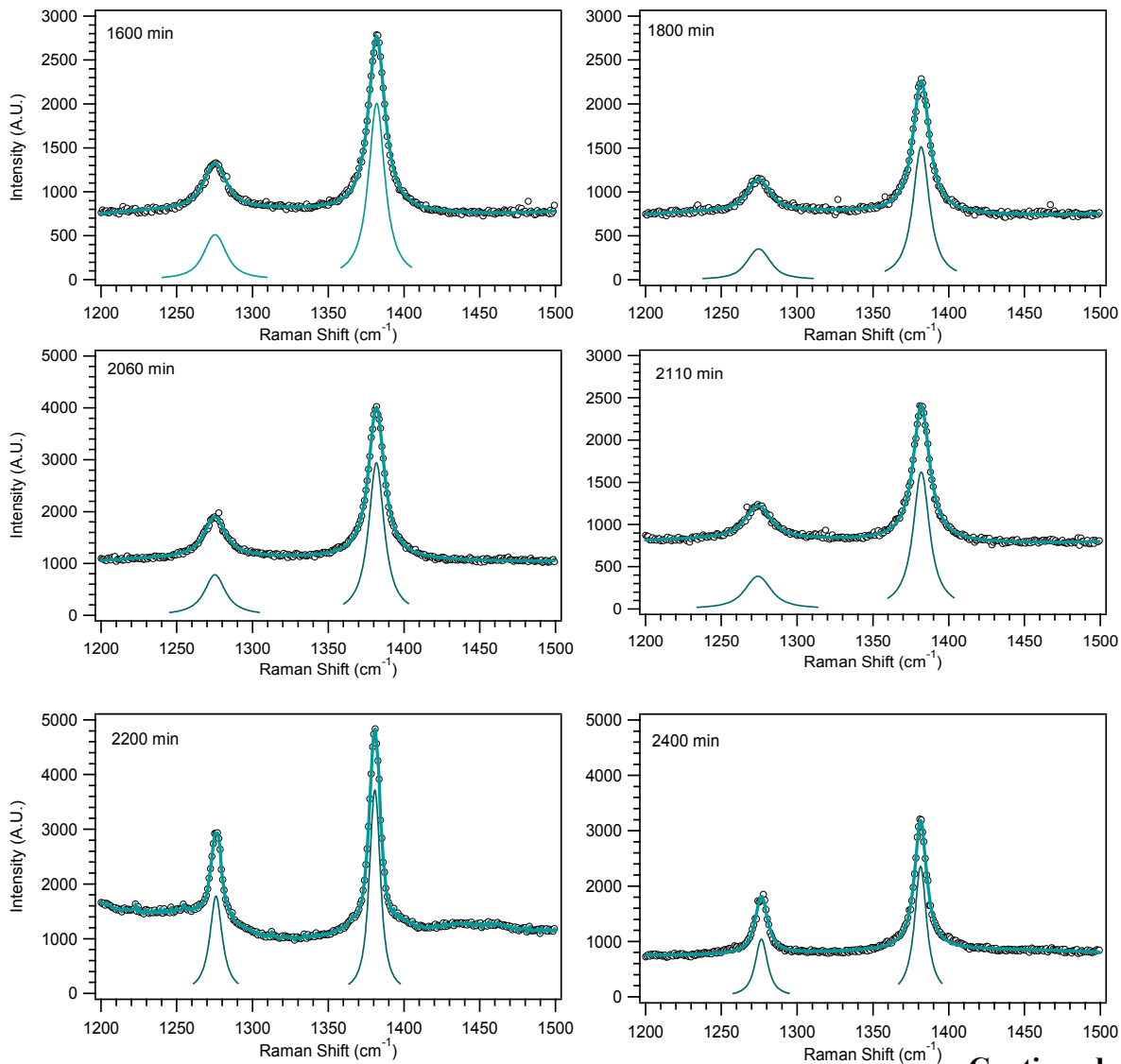
Figure 3.7 Continued
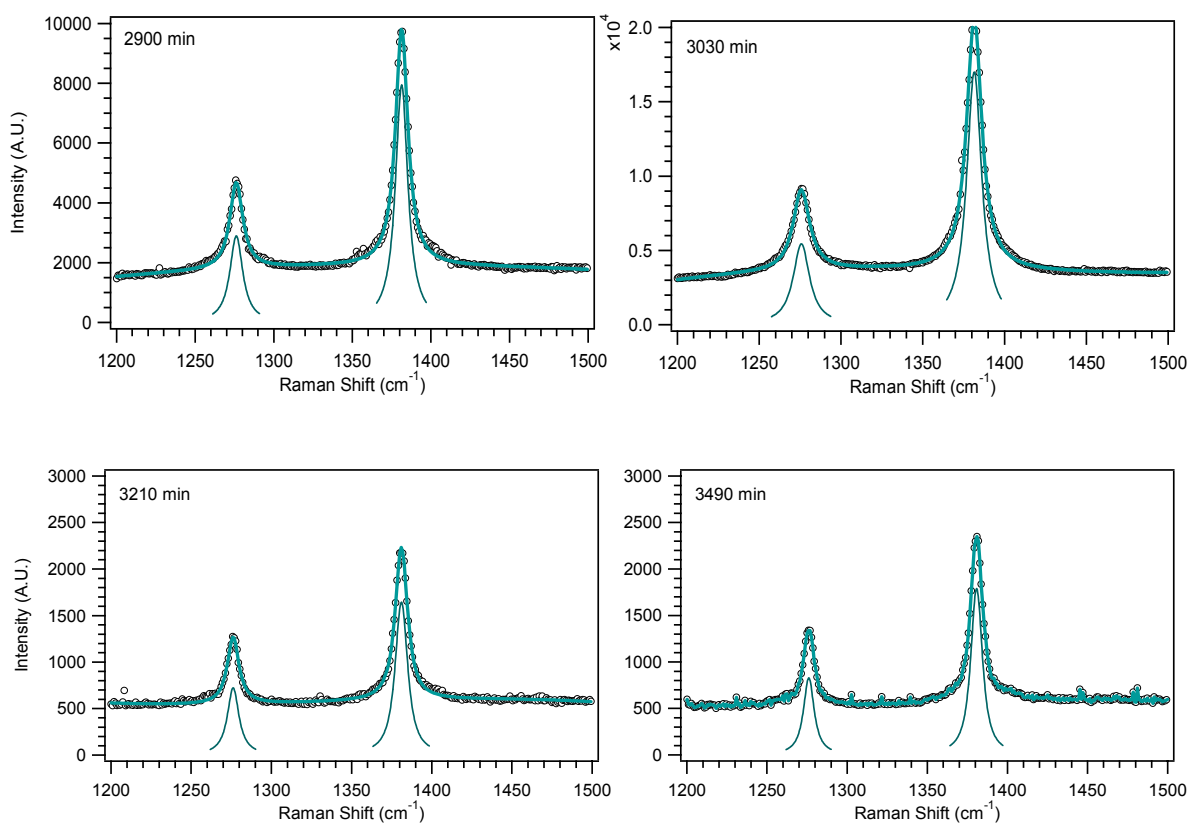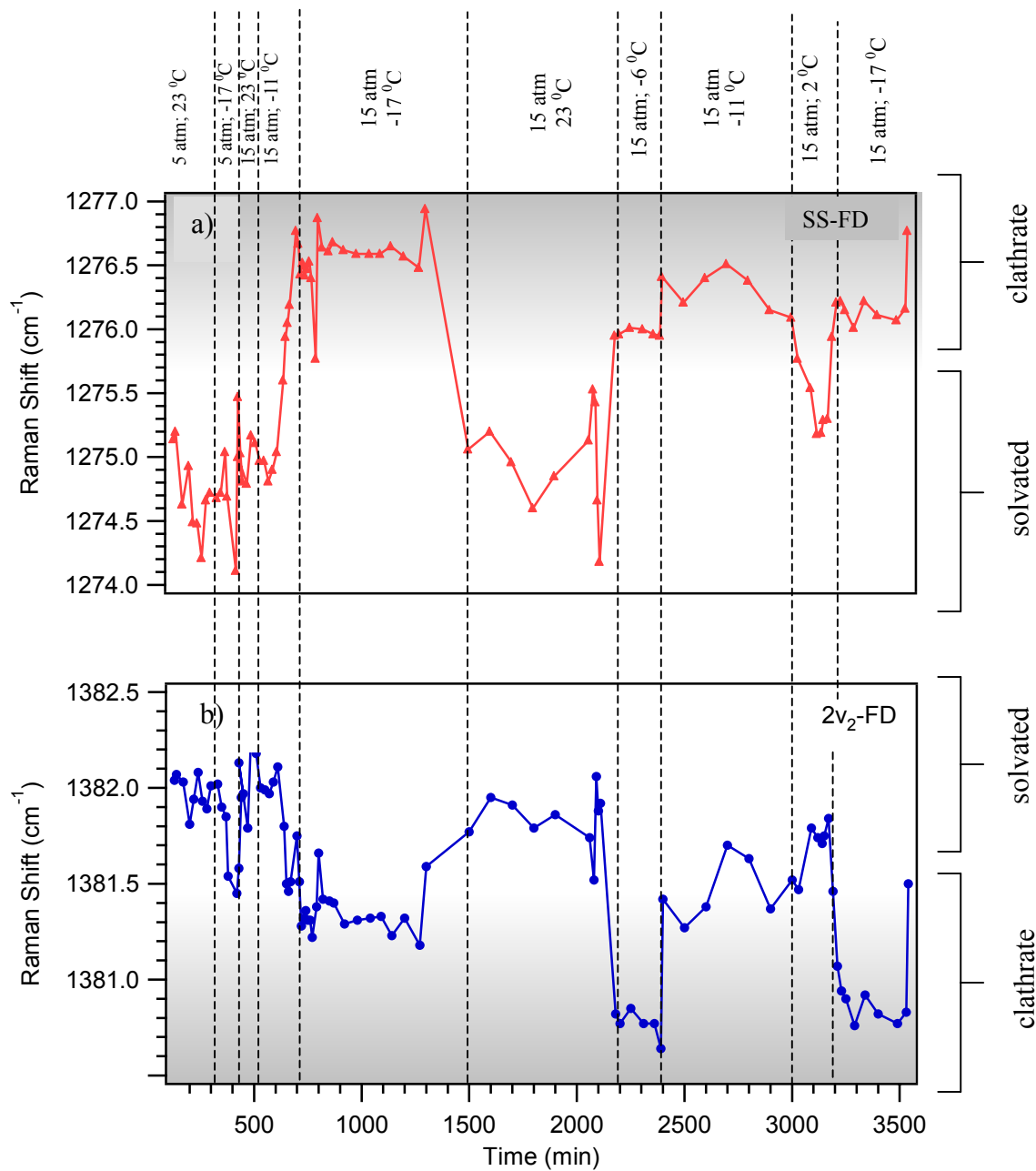
Figure 3.8: (a) SS-FD shift and (b) 2ν₂-FD shift analysis while adjusting the temperature and pressure conditions. The shifts shown were taken over a period of 3600 min (3 days).

47
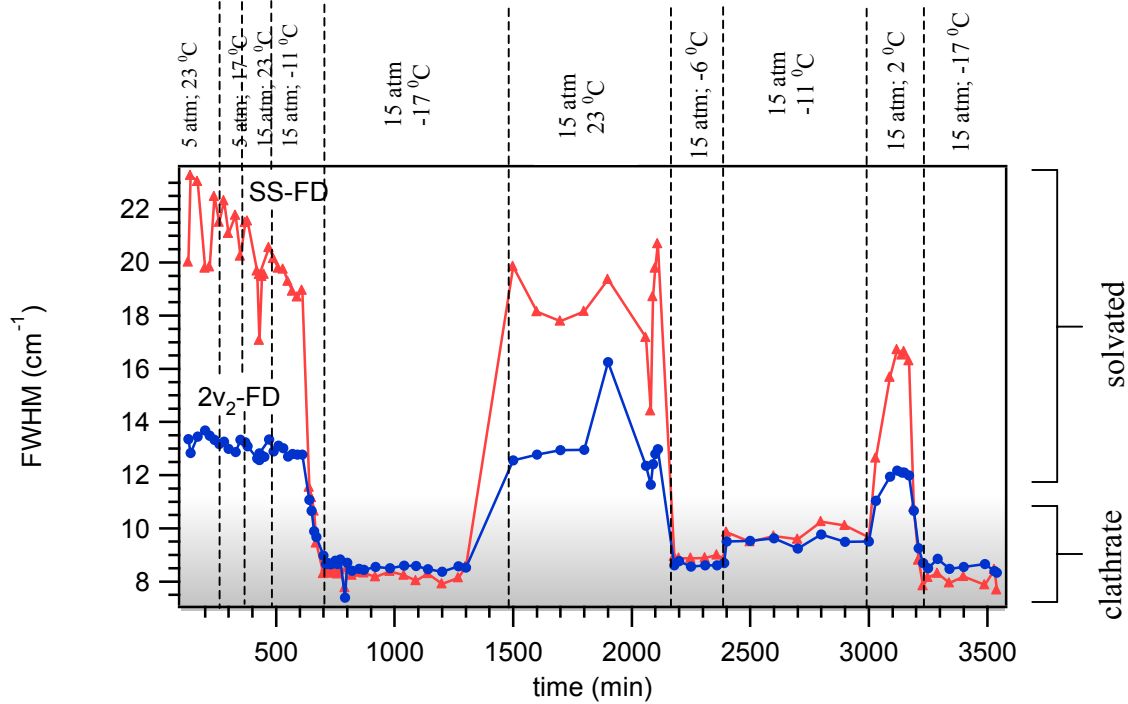
Figure 3.9: FWHM analysis of the Fermi diads in the clathrate and solvated phase while adjusting the temperature and pressure conditions. The FWHM shown are taken over a period of 3600 min (3 days).
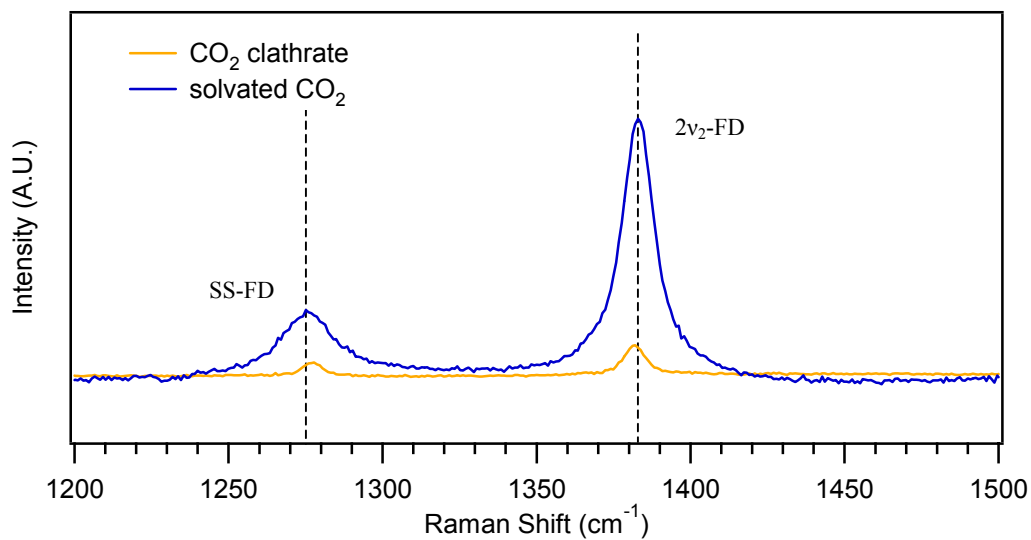
Figure 3.10: Raman spectra of solvated CO_2 and CO_2 clathrates. The black dotted lines are located at the solvated CO_2 peak positions to show the peak shift associated with clathrate formation.
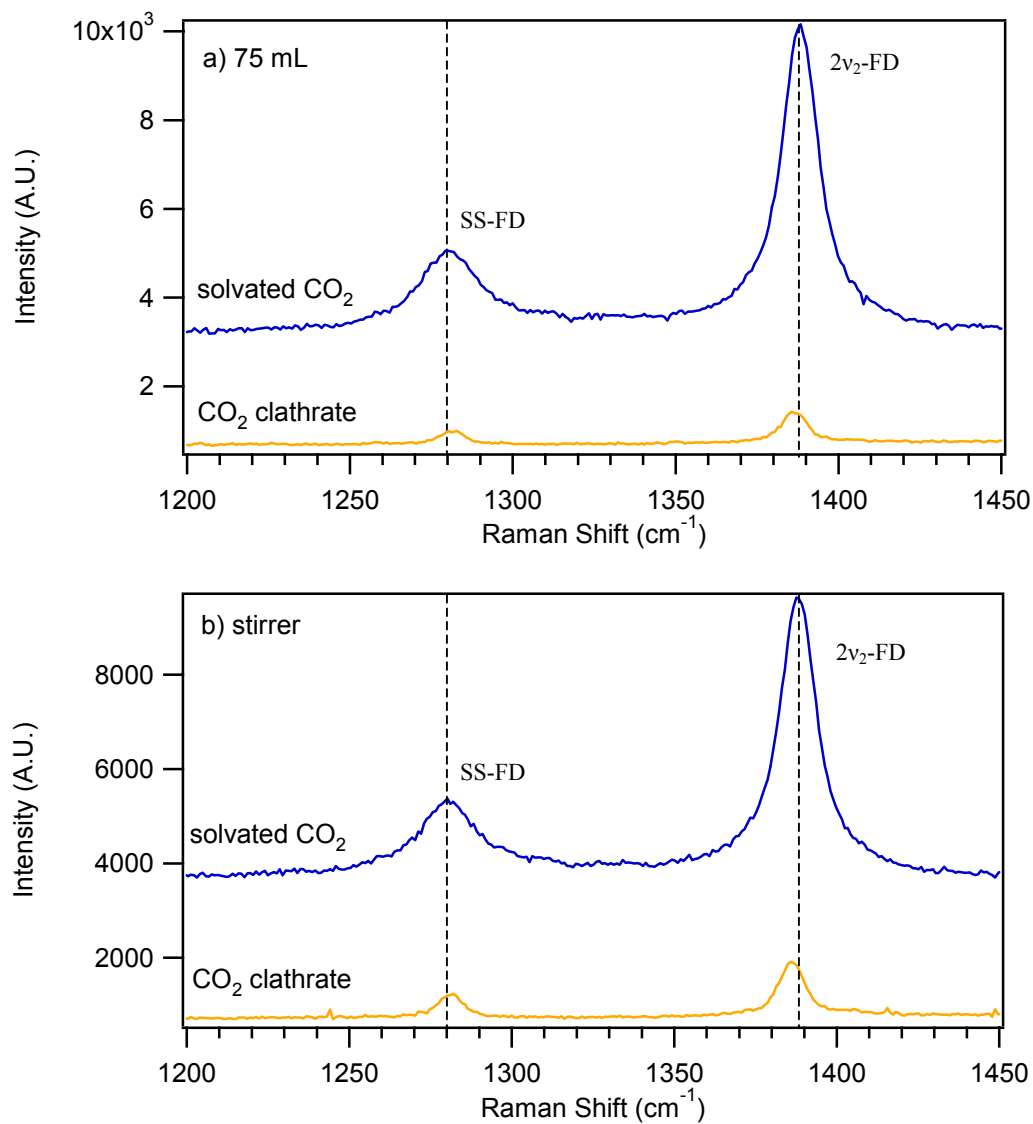
Figure 3.11: Raman spectra of solvated CO_2 and CO_2 clathrates. The spectra are acquired at 15 atm and 23 ± 2 ^{0}C and -17 ± 2 ^{0}C, respectively. The black dotted lines show the peak shift with respect to the solvated CO_2 spectrum. (a) A volume of 75 mL of nano-pure water is used. In (b), the solution was stirred continuously.
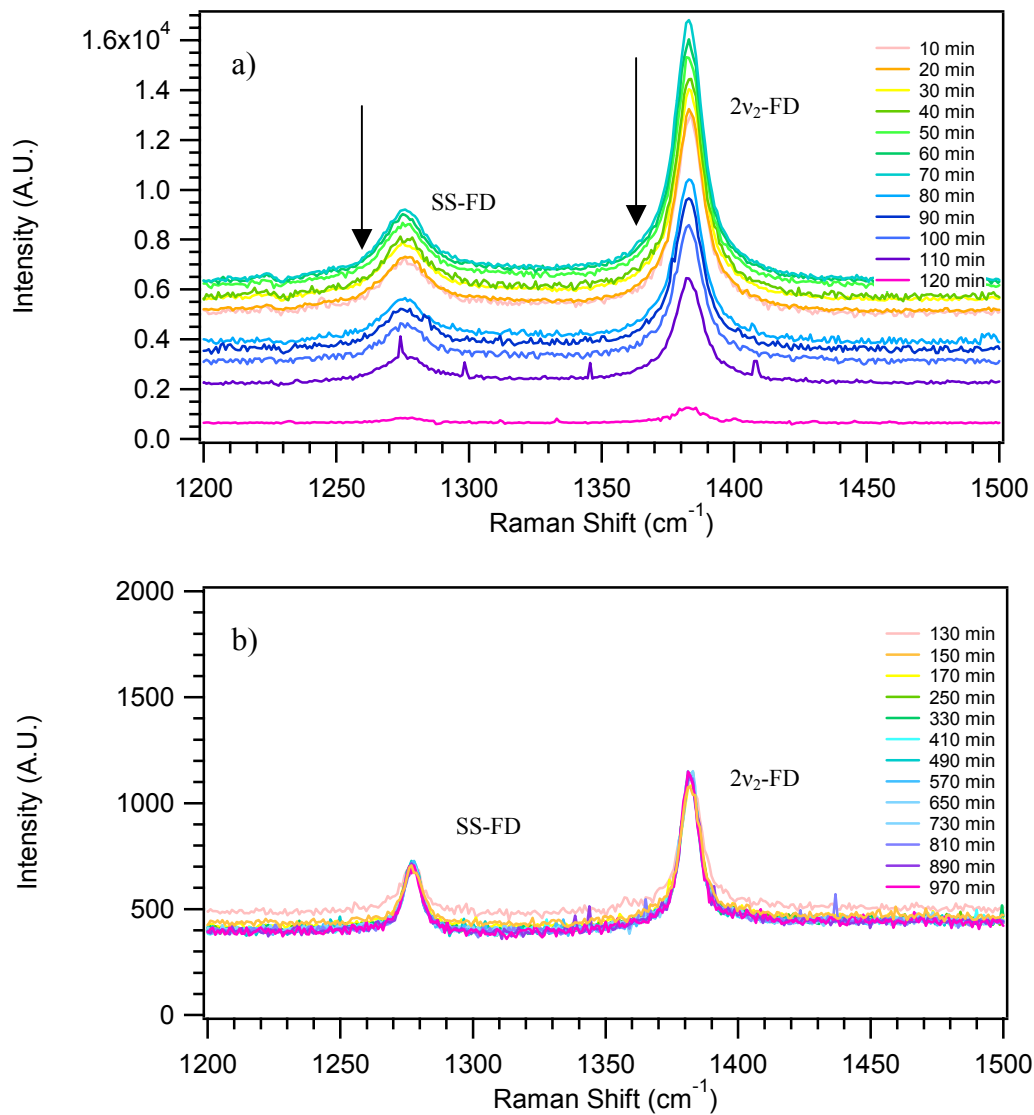
Figure 3.12: **(a) The formation of CO_2 clathrates from solvated CO_2 as a function of time. The arrows show the decrease in intensity while the system is cooling to a clathrate temperature. (b) The formation of CO_2 clathrates once formation begins.**
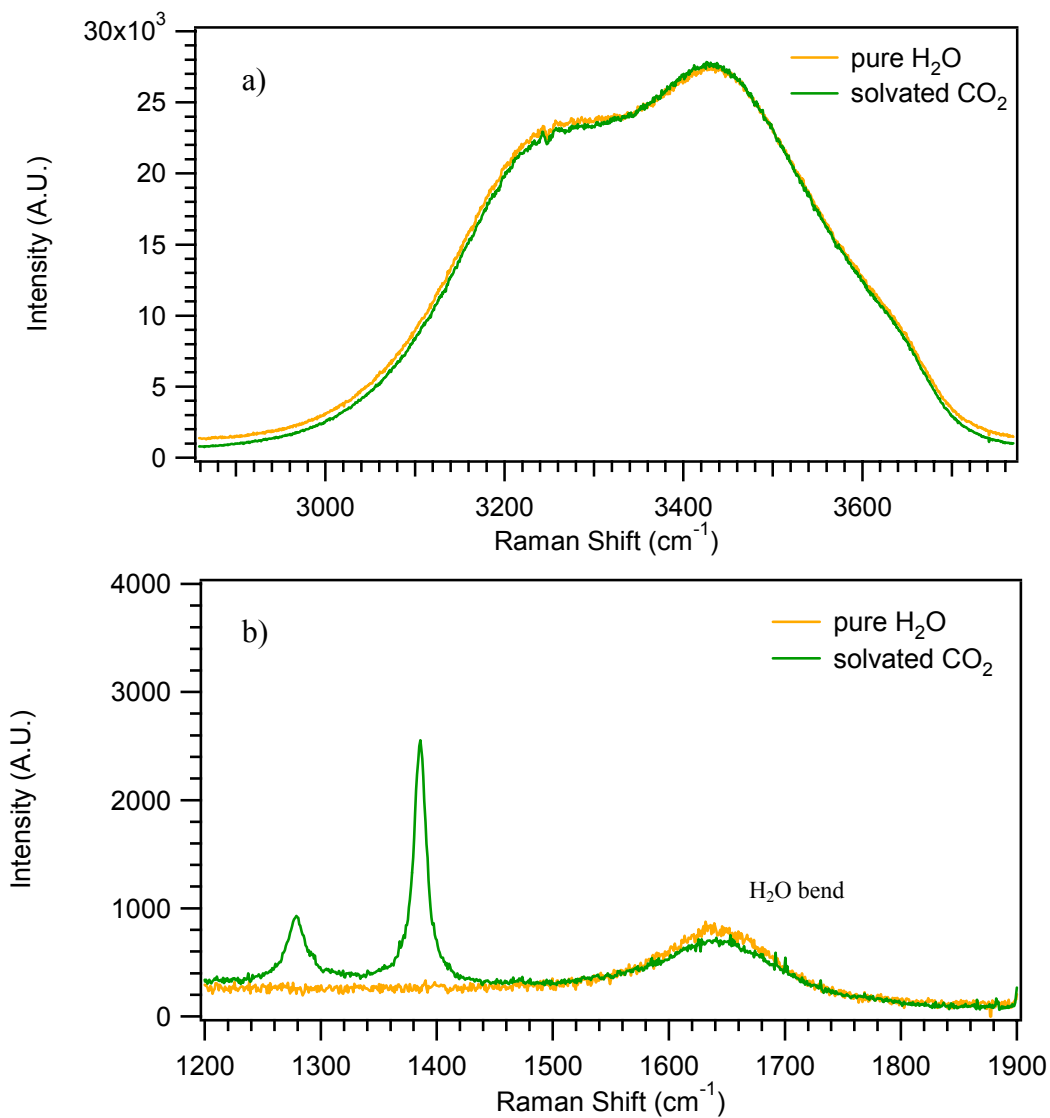
Figure 3.13: Water spectra in the pure and solvated environments. (a) The stretching region of water; (b) The bending region of water, including the $CO_{2(aq)}$ Fermi diads. Both spectra for (b) are offset.
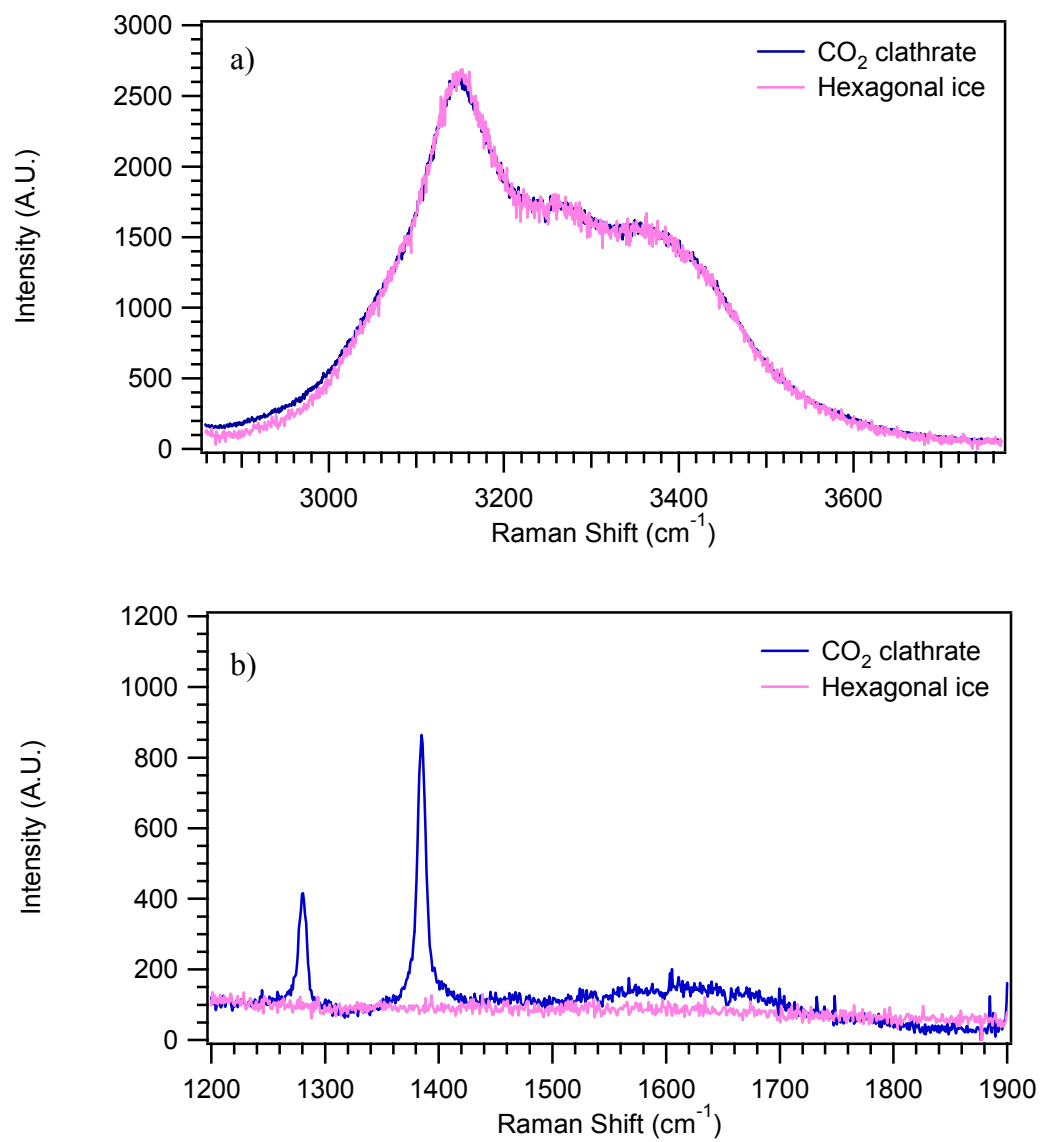
Figure 3.14: Spectra of hexagonal ice and clathrates. (a) The stretching region of water; (b) The bending region of water including the $CO_{2(aq)}$ Fermi diads. Both spectra are offset in (b).

53

frequency (cm^{-1})	assignment
1410	$2v_2$-FD; fermi diad of $CO_{2(g)}$
1382	$2v_2$-FD; fermi diad of $CO_{2(aq)}$
1381	$2v_2$-FD; fermi diad of $CO_{2(c)}$
1359	C=O SS of HCO_3^-
1308	SS-FD; fermi diad of $CO_{2(g)}$
1300	C-OH bend of HCO_3^-
1276	SS-FD; fermi diad of $CO_{2(c)}$
1275	SS-FD; fermi diad of $CO_{2(aq)}$
1061	C=O SS of CO_3^{2-}
1014	C-OH stretch of HCO_3^-

Table 3.1: Vibrational assignments of KHCO$_3$ in aqueous solution and CO$_2$ in the gas, aqueous, and clathrate phases

	SS-FD cm^{-1}	2v$_2$-FD cm^{-1}
Gas	7.2	6.5
Clathrate	7.8	8.5
Solvated	19.4	13.2

Table 3.2: The FWHM of the SS-FD and 2v$_2$-FD in the gas, clathrate, and solvated phases.

	X cm^{-1}	Δ cm^{-1}	v_1 cm^{-1}	v_2 cm^{-1}	$2v_2$ cm^{-1}
Gas	102.0	2.9	1334.6	669.4	1338.8
Clathrate	105.2	25.1	1321.9	671.6	1343.2
Solvated	107.1	32.5	1314.4	675.0	1350.0

Table 3.3: The calculated values of the gas, clathrate, and solvated phases of the observed frequency separation of the two Fermi diads (X), the separation of the unperturbed vibrational levels (Δ), the unperturbed symmetric stretch (v_1), and the unperturbed bending mode (v_2).

Conditions	Time	SS-FD			$2v_2$-FD		
	(Min)	Position (cm^{-1})	Area	FWHM (cm^{-1})	Position (cm^{-1})	Area	FWHM (cm^{-1})
5 atm	130	1275.1	5635	20.02	1382.0	89419	13.35
23 ^{O}C	140	1275.2	5768	23.27	1382.1	96570	12.83
	170	1274.6	9103	23.04	1382.0	52280	13.45
	200	1274.9	16915	19.78	1381.8	145310	13.68
	220	1274.5	19882	19.83	1381.9	155299	13.48
	240	1274.5	25404	22.47	1382.1	150345	13.33
	260	1274.2	24624	21.51	1381.9	146720	13.17
	280	1274.7	24969	22.32	1381.9	128343	13.25
	300	1274.7	25052	21.09	1382.0	145079	13.00
	330	1274.7	24061	21.77	1382.0	156500	12.87
5 atm	370	1275.0	36699	21.49	1381.9	89419	13.23
-17 ^{O}C	380	1274.7	37429	21.56	1381.5	96570	13.09
	420	1274.1	19037	19.68	1381.5	52280	12.63

Continued

Table 3.4: Calculated values for the Fermi diads of CO_2 for the peak position, peak area, and peak FWHM for the SS-FD and $2v_2$-FD. The Voigt fit function is used.

Table 3.4 Continued

Conditions	Time (Min)	SS-FD Position (cm^{-1})	Area	FWHM (cm^{-1})	2v$_2$-FD Position (cm^{-1})	Area	FWHM (cm^{-1})
15 atm 23 ^{O}C	430	1275.5	53293	17.07	1381.58	145310	12.56
	440	1275.0	60954	19.48	1381.95	155299	12.73
	450	1274.8	58849	19.56	1381.97	150345	12.69
	430	1275.0	56119	19.54	1382.13	146720	12.82
	470	1274.8	53158	20.56	1381.79	128343	13.34
15 atm -11 ^{O}C	490	1275.2	54381	20.15	1382.44	145079	12.89
	510	1275.1	57006	19.78	1382.18	156500	13.11
	530	1275.0	65623	19.75	1382	171556	13.01
	550	1275.0	68217	19.29	1381.99	185554	12.70
	570	1274.8	70519	18.92	1381.97	203585	12.80
	590	1274.9	18210	18.70	1382.03	50294	12.78
	610	1275.0	75134	18.96	1382.11	200231	12.78
	640	1275.6	7668	11.54	1381.8	20915	11.07
	650	1275.9	7914	11.16	1381.5	21232	10.66
	660	1276.1	8538	10.65	1381.46	21373	9.89
15 atm -17 ^{O}C	700	1276.8	8974	8.30	1381.75	23336	8.97
	710	1276.7	10359	8.55	1381.51	23872	8.66
	720	1276.4	10312	8.32	1381.28	23475	8.69
	730	1276.5	10281	8.43	1381.32	24416	8.65
	740	1276.4	10642	8.32	1381.36	24782	8.68
	750	1276.5	10410	8.44	1381.31	24556	8.78
	760	1276.5	10814	8.28	1381.31	25191	8.66
	770	1276.4	10731	8.44	1381.22	24599	8.82
15 atm 23 ^{O}C	790	1275.8	3677	7.76	1381.38	8933	7.39
	800	1276.9	11869	8.52	1381.66	26410	8.71
	820	1276.6	10733	8.24	1381.42	25592	8.41
	850	1276.6	12256	8.34	1381.41	27478	8.48
	870	1276.7	12287	8.32	1381.4	27152	8.44
	920	1276.6	12228	8.18	1381.29	27356	8.55
	980	1276.6	12025	8.38	1381.31	27739	8.50
	1040	1276.6	12199	8.24	1381.32	28202	8.59
	1140	1276.7	12067	8.30	1381.23	27604	8.47
	1200	1276.6	12103	7.91	1381.32	27910	8.37
	1270	1276.5	12157	8.13	1381.18	27981	8.57

Continued

Table 3.4 Continued

Conditions	Time (Min)	SS-FD Position (cm^{-1})	Area	FWHM (cm^{-1})	2v$_2$-FD Position (cm^{-1})	Area	FWHM (cm^{-1})
15 atm -11 ^{O}C	1500	1275.1	17536	19.85	1381.8	42958	12.55
	1600	1275.2	15100	18.14	1382.0	39396	12.77
	1700	1275.0	7652	17.79	1381.9	36788	12.94
	1800	1274.6	9348	18.16	1381.8	30331	12.96
	1900	1274.9	7258	19.36	1381.9	18310	16.25
15 atm 2 ^{O}C	2060	1275.1	21432	17.17	1381.7	56029	12.35
	2080	1275.5	19083	14.42	1381.5	50427	11.64
	2090	1275.4	16379	18.71	1382.1	38533	12.41
	2100	1274.7	13572	19.79	1381.9	34922	12.80
	2110	1274.2	12563	20.70	1381.9	32735	12.98
15 atm -6 ^{O}C	2180	1276.0	24569	8.93	1380.8	50304	8.62
	2200	1276.0	24532	8.87	1380.8	52321	8.77
	2250	1276.0	24586	8.88	1380.9	51752	8.56
	2360	1276.0	25309	9.00	1380.8	51393	8.62
	2390	1276.0	24481	8.86	1380.6	51963	8.70
	2400	1276.4	15868	9.86	1381.4	35300	9.51
	2500	1276.2	21953	9.49	1381.3	52102	9.53
	2600	1276.4	27326	9.71	1381.4	64365	9.62
	2700	1276.5	31272	9.58	1381.7	77762	9.24
	2800	1276.4	41089	10.26	1381.6	99959	9.77
	2900	1276.2	46410	10.11	1381.4	116174	9.49
15 atm -17 ^{O}C	3000	1276.1	68518	9.66	1381.5	190489	9.51
	3030	1275.8	108748	12.64	1381.5	293731	11.04
	3090	1275.5	122380	15.68	1381.8	326958	11.94
	3120	1275.2	126485	16.72	1381.7	338225	12.17
	3140	1275.2	126692	16.52	1381.7	338222	12.09
	3170	1275.3	125205	16.30	1381.8	334258	11.99
	3190	1275.9	9094	10.79	1381.5	24792	10.66
	3210	1276.2	9426	8.80	1381.1	22163	9.25
	3230	1276.2	10034	7.84	1380.9	23966	8.69
	3250	1276.2	10409	8.16	1380.9	24626	8.50
	3290	1276.0	9908	8.31	1380.8	23644	8.86
	3340	1276.2	10185	7.95	1380.9	23449	8.47
	3400	1276.1	10128	8.19	1380.8	23555	8.55
	3490	1276.1	10322	7.87	1380.8	23657	8.66

CHAPTER 4

CONCLUSION

The Fermi diads of CO_2 were investigated in the aqueous and clathrate phases using Raman spectroscopy. As CO_2 clathrates form from the aqueous phase, the Fermi diads are observed to shift by ~1 cm^{-1}. This shift is evidence that the CO_2 vibrational modes, such as symmetric stretch and bending modes, are affected by the formation of the clathrate cage. In addition, the Fermi diads shift closer together because the SS-FD blue-shifts and the $2v_2$-FD red-shifts. These shifts indicate the bonds involved in the symmetric stretch become stronger with clathrate formation while the bending mode shows the CO_2 molecule is less hindered by the surrounding H_2O molecules.

The small shift illustrates the intermolecular interactions between the CO_2 molecule and H_2O molecules are weak. Hydrogen bonding would result in a larger shift than was observed. Therefore, the small shift supports van der Waals forces as the sole force for preventing the clathrate cage from collapsing.

The bending mode and stretching region of H_2O were evaluated using Raman spectroscopy to examine the effect of the addition of CO_2 under solvated and clathrate conditions. The bending mode and stretching region in pure H_2O and the aqueous phase were both similar in intensity and peak position. The "free OH" band remains unchanged

in the solvated system suggesting no hydrogen bonding occurs between H_2O and CO_2 molecules.

The bending mode and stretching region in hexagonal ice and the clathrate phase were both similar in intensity and peak position. A stronger hydrogen bonding network is found in hexagonal ice compared to pure H_2O. Therefore, the similar structures of the two regions show that the CO_2 clathrate cages consist of a stronger hydrogen bonded network than the CO_2 aqueous phase.

Although the majority of these results have been reported in the literature previously, these experiments are unique because they have been conducted under different experimental conditions. Most of the literature investigates the region at temperatures of 0 ^{o}C and higher using very high pressures of up to GPa. The coexistence region of the CO_2 phase diagram is another region of great interest in the literature. The conditions in this study are unique because they are well within a three-phase region while still using ambient temperatures and pressures. Another important difference between the current literature and these results is the cell setup. Several cell setups use a cooling rod in the center of the cell that is kept cooler than the surrounding solution. The formation of clathrates initiates on the cooling rod instead of growing throughout the solution. This method significantly decreases the scatter associated with a crystallized substance resulting in a more accurate quantitative analysis of the sample.

Continued analysis of CO_2 clathrates is needed, as many details of the kinetics of formation and dissociation are still unknown. In addition, the sequestration of CO_2 in the ocean via storage of CO_2 clathrates requires accurate information regarding the effect of CO_2 clathrates when mixed with salt solutions. Natural oceanic occurrences such as

earthquakes and currents will affect the CO_2 clathrate stability and could cause

uncontrollable clathrate dissociation. Therefore, it is of vital importance to continue

studying CO_2 clathrates to make an informed assessment of the effects sequestration of

CO_2 will have on the environment.

CHAPTER 5

HENRY'S LAW

5.1 Introduction

Being the second largest contributor to the greenhouse effect, CO_2 significantly impacts the environment. With a rise of anthropogenic CO_2 predicted throughout the coming years, it is necessary to find a solution to decrease CO_2 in the atmosphere.[57,58] It has been suggested that sequestering CO_2 in the oceans could be a solution for the high concentration of anthropogenic CO_2. For this to occur, the CO_2-water system must be thoroughly understood for these methods to be successfully applied. The solubility of CO_2 in water is an important parameter when considering the disposal of CO_2 in the oceans. Therefore, reliable solubility information, such as Henry's law constants, must be obtained over a wide range of pressures and temperature conditions before CO_2 can be stored in the oceans.[59]

The Henry's law constant describes the partitioning of a species between the gas and the aqueous phases (Figure 5.1).[60,61] Henry's law is described in terms of pressure and concentration in Equation 5.1.

$$[X]_{aq} = H \cdot P_x \qquad (5.1)$$

When X is a gas, $[X]_{aq}$ is concentration of the gas in solution. H is the Henry's law

constant in units of M/atm, and P_x is the partial pressure of the gas phase at equilibrium.

In general, the most soluble gases have a Henry's law constant of 10^5 M/atm while

insoluble gases have a Henry's law constant of ~10^{-3} M/atm.[60] However, CO_2 can react

further to produce the ionic species as shown in the following reactions. These reactions

allow larger concentrations of CO_2 to be taken up into solution. Most importantly,

Henry's law is only valid for systems at equilibrium.[60,61]

[1] $CO_{2(g)} \leftrightarrow CO_{2(aq)}$

[2] $CO_{2(aq)} + H_2O \leftrightarrow H_2CO_{3(aq)}$ $K_{eq} = 1.3 \times 10^{-3}$

[3] $H_2CO_{3(aq)} \leftrightarrow H^+_{(aq)} + HCO_3^-{}_{(aq)}$ $K_{a1} = 2.00 \times 10^{-4}$

[4] $HCO_3^-{}_{(aq)} \leftrightarrow H^+_{(aq)} + CO_3^{2-}{}_{(aq)}$ $K_{a2} = 4.69 \times 10^{-11}$
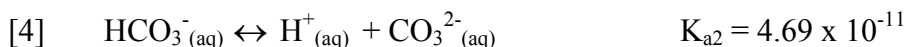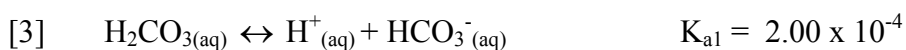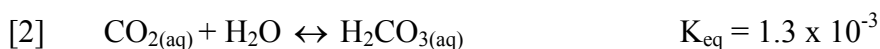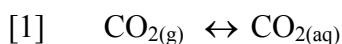
5.2 Experimental Setup

A 532 nm continuous wave (CW) laser (Spectra-Physics, Millennia II, ~95 mW)

was used to obtain the Raman spectra. A fiber optic probe (InPhotonics, RP 532-05-15-

FC) both delivers the laser excitation source to the sample and collects the scattered light.

A 200 μm collection fiber optic (InPhotonics, Inc.) delivers the scattered light to the

entrance slit of a 500 mm monochromator (Acton Research, SpectraPro 500i). A 1200

g/mm grating blazed at 1 μm was used. The slit width was set to 50.0 μm. A liquid

nitrogen cooled CCD camera (Roper Scientific, LN400EB, 1340 x 400 pixel array, back-

illuminated and deep depletion CCD) collected the data. The CCD was calibrated using

the 435.83 nm line of a fluorescent lamp. The 1382 cm^{-1} peak of a crystalline

naphthalene spectrum was used to calibrate the wavenumber position by comparing the

observed position to literature values.[29] Data collection and display were performed using the SpectraSense software (Acton Research, version 4.2.9).

A stainless steel cell (volume of 200 mL) was filled with 100.0 mL nano-pure H_2O (18.2 $M\Omega \bullet cm$). A pressure transducer (MKS Baratron pressure transducer, 10,000 torr) was attached to the cell lid and the pressure was read from a digital recorder (MKS PDR2000 Dual Capacitance Manometer). The solution was stirred during the course of the experiment. A thermister was attached to the outside of the cell, and heat tape was placed around the cell. A digital controller (Wattow 96) was used to control the temperature of the cell. When the desired temperature was achieved, the pressure was recorded. This pressure was used as the partial pressure of H_2O in the cell.

A calibration curve was used to relate the peak area of the CO_2 Fermi diad to the concentration of CO_2 in solution at 30 ± 2 ^oC. The following experimental setup was used. When 100 mL of water reached the desired temperature, the partial pressure was recorded. $CO_{2(g)}$ (99.9% purity) was then bubbled into the cell. The cell was allowed to reach equilibrium before the pressure was increased. Equilibrium was observed in the system when the intensity of the Fermi diads leveled off. At each new pressure, the system reached equilibrium after 60 min. The pressure was increased during the experiment from 6 to 12 atm. Spectra were acquired every 10 min with a 6 min acquisition time.

5.3 Henry's Law

The temperature of the system was varied from 27 to 80 ^oC to determine the Henry's law constant. Prior to introducing CO_2 into the cell, the water reached a desired temperature and the pressure was recorded. At this time, 5 atm of $CO_{2(g)}$ was added to

the cell. When the system reached equilibrium (the intensity of the Fermi diads remained constant for 60 min), the pressure was recorded. Upon achieving equilibrium, the pressure was again increased. Raman spectra were taken as previously described. The pressure was adjusted from 5 to 13 atm during the experiment. A 6 min integration time was used to acquire all spectra and a spectrum was obtained every 10 minutes. Each data point in the graphs shown in Figure 5.3 is an average of 3 to 6 spectra. The Raman areas and the standard deviations of the averages are shown in Table 5.1.

5.4 Data Analysis

All spectra were evaluated using Igor Pro (Wavemetrics, Version 4.0.5.1). A graphing macro (Appendix C), written by Dr. Laura Voss and Lisa Van Loon of the Allen lab, loaded individual spectra into one graph and table. The spectra were fit with a Voigt function, and the peak area of the $2\nu_2$-FD was determined. The $2\nu_2$-FD was chosen for analysis because it has a large S/N at all pressures used in the experiment. The peak areas of spectra acquired for a given pressure and temperature were averaged to determine the peak area for that pressure.

5.5 Results

Quantitative analysis of Raman spectra relates the concentration of a species to the Raman intensities and areas of a corresponding peak. The relation between Raman intensity and concentration of molecules in a sample are shown in Equation 5.2-5.3.[28]

$$I = N_i \sigma(\nu_{ex}) \nu_{ex}^4 E_0 e^{-E_i / kT} \tag{5.2}$$

The intensity of Raman scattering I is described by $\sigma(\nu_{ex})$, the Raman cross section in cm^2, ν_{ex} is the frequency of the excitation source, N_i which is the number density in state i, and the exponential term, $e^{-E_i/kT}$, is the Boltzmann factor for state i. The Raman intensity is also directly proportional to the source of irradiance, E_0. The intensity is directly proportional to the number density N_i of the species of interest.[28,31,36] This means the concentration of the species being probed, i.e. aqueous CO_2, can be determined by the peak intensity. For this study, a calibration curve is used to relate the concentration of a species to the Raman area.

The calibration curve (Figure 5.2) was determined using the peak area of the $2\nu_2$-FD at 30 ± 2 $^{\circ}C$. Table 5.2 shows the determined values for the Raman area and the standard deviation for the $2\nu_2$-FD. The partial pressure of CO_2 was determined by assuming the partial pressure of H_2O was the pressure recorded prior to addition of CO_2 in the cell. All recorded pressures were corrected for the partial pressure of H_2O. An average of known Henry's law constants at 30 $^{\circ}C$[62,63] was substituted into Equation 5.1 to calculate the concentrations of CO_2 in solution. Henry's law constants from the literature are shown in Table 5.6. The determined concentrations were then plotted against the corresponding peak area. The data was fit with a linear regression line as shown in Figure 5.2.

To determine the Henry's law constant at a particular temperature, the average of the peak areas after achieving equilibrium for each pressure was calculated. Tables 5.1-5.4 show all the calculated values for the pressures as well as their corresponding deviation. The calculated spectral fits are shown in Figures 5.3-5.5. The peak area average and the CO_2 partial pressure were substituted into the calibration equation. The

resulting concentration of CO_2 was graphed as a function of CO_2 partial pressure (Figure 5.6). The data was fit with a linear regression. In Equation 5.1, the slope is the Henry's law constant for a given temperature. All calculated Henry's law constants are included in Table 5.5. The values are in good agreement with literature values, which are shown in Table 5.6.[62-64]

The Henry's law constants decrease as the temperature increases. A small Henry's law constant of 10^{-3} indicates low solubility of a gas. At all temperatures, the Henry's law constants for CO_2 are 10^{-2} M/atm indicating that CO_2 is a relatively insoluble gas. Independent of temperature, Figure 5.6 shows that the concentration of CO_2 is proportional to pressure. With an increase in pressure, the number of molecules in the gas phase increases[61] resulting in more molecules striking the surface of liquid water. Therefore, the solution must take up more CO_2 molecules, resulting in an increased solubility.

5.6 Conclusion

The sequestration of CO_2 in the ocean has been proposed as a means for reducing atmospheric CO_2. However, the CO_2-H_2O system must be understood before CO_2 can be administered into the oceans for storage. One major contributor to obtaining valuable information for this system is to understand the solubility of CO_2 under deep ocean conditions by using Henry's law. Henry's law constants for CO_2 have been determined using Raman spectroscopy for a range of pressures from 5 to 13 atm and temperatures from $27 - 80\ ^{\circ}C$.

$$[X]_g = P_x$$

$$K_{eq} = \frac{[X]_{aq}}{[X]_g}$$

$$H = \frac{[X]_{aq}}{P_x}$$

$$[X]_{aq}$$
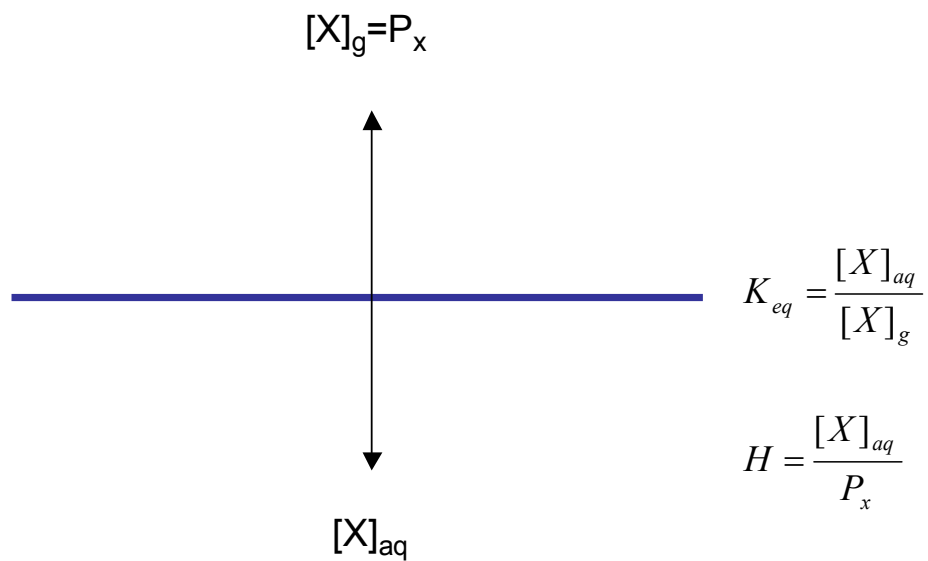
Figure 5.1: **Diagram illustrating the transfer of a gaseous species [X]$_g$ to an aqueous species [X]$_{aq}$. The equilibrium constant (K$_{eq}$) equation is shown as well as the Henry's law equation. X is CO$_2$ and P$_x$ is the partial pressure. The solid blue line represents the gas-liquid interface.**
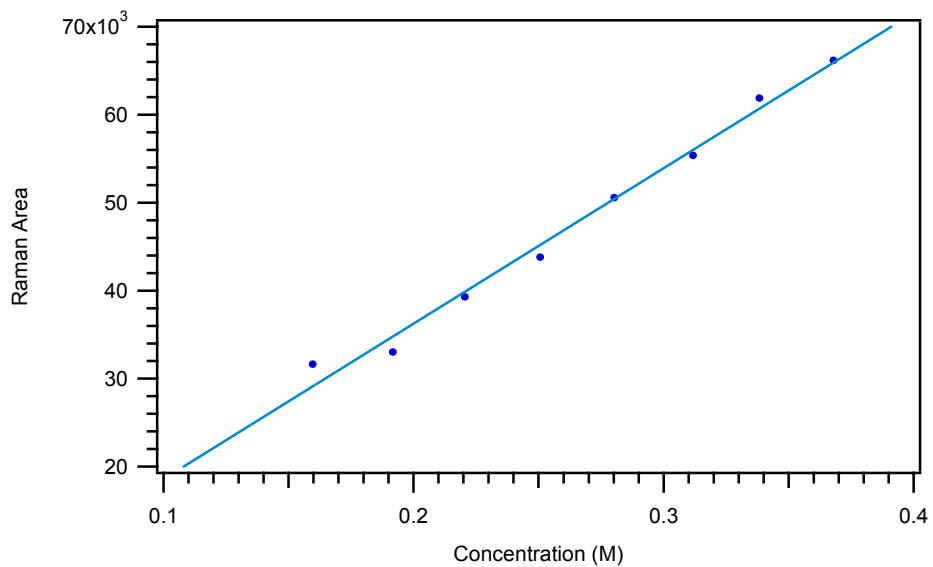
Figure 5.2: The calibration curve used to relate the Raman area to the concentration of CO_2 molecules in solution at 30 ^{o}C. The linear fit is shown in blue. Pressures from 5 to 13 atm were used.
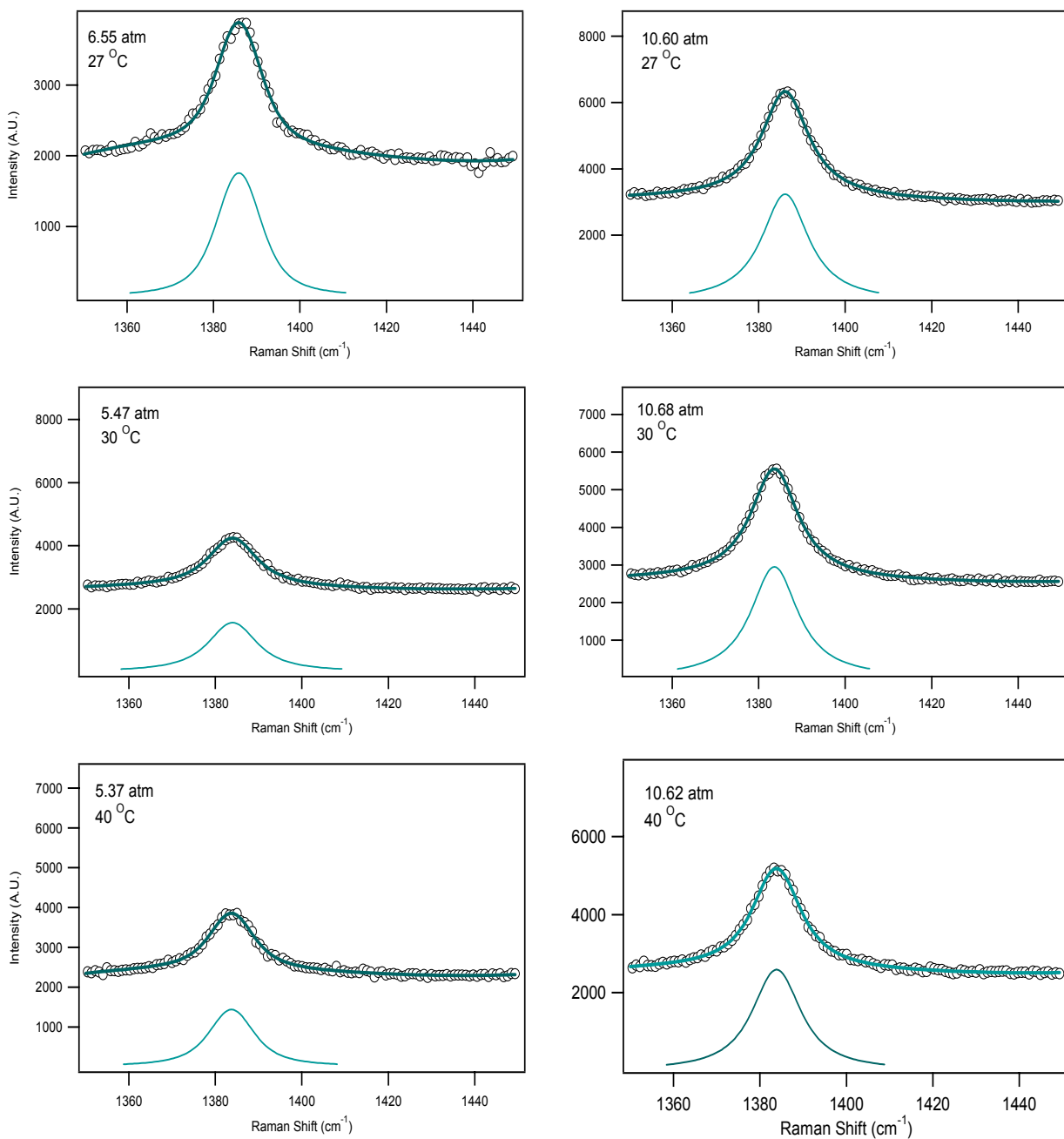
Continued

Figure 5.3: Spectral fits used to determine the peak area of the Fermi diad. The pressure and temperature conditions are shown. The calculated fits are in green and the raw data are shown as black circles.

Figure 5.3 Continued
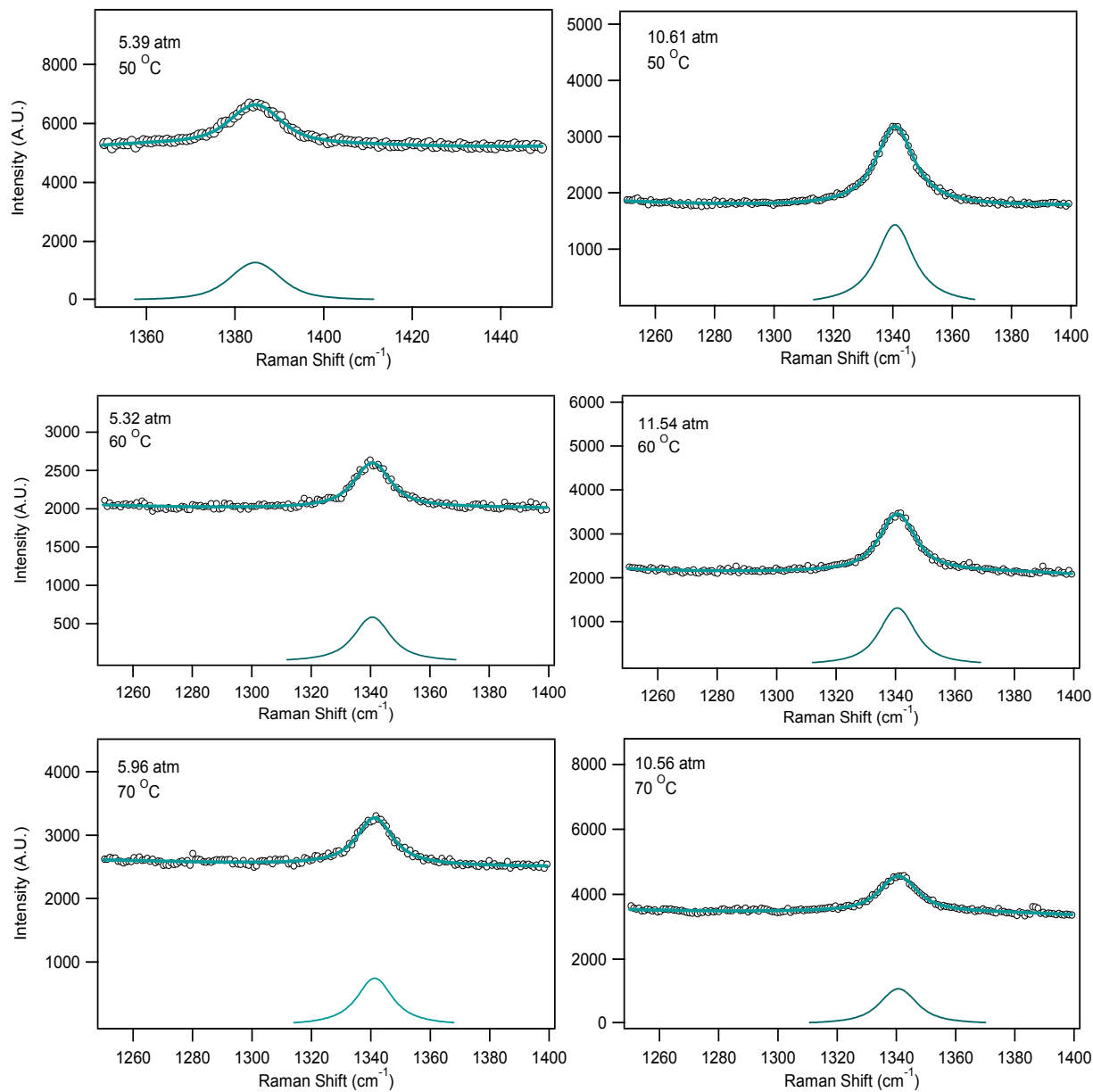
Continued

Figure 5.3 Continued
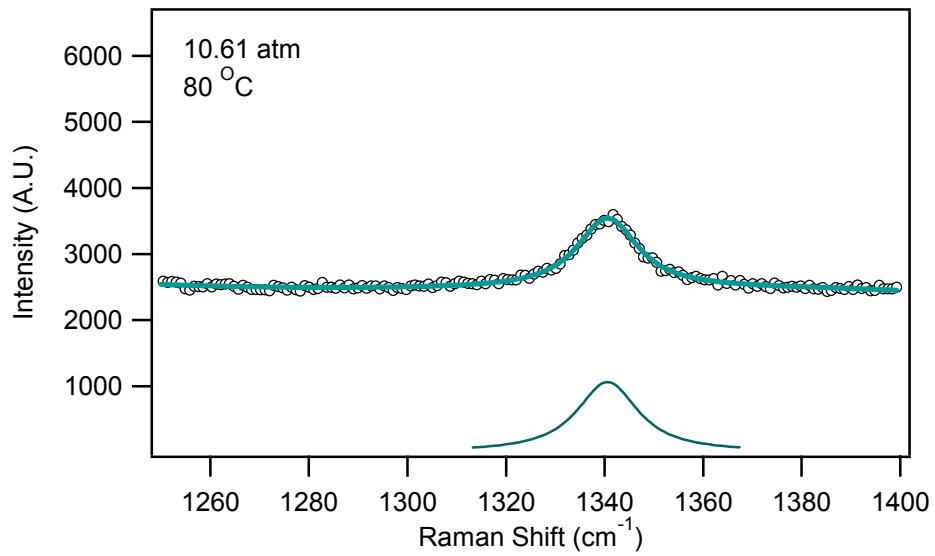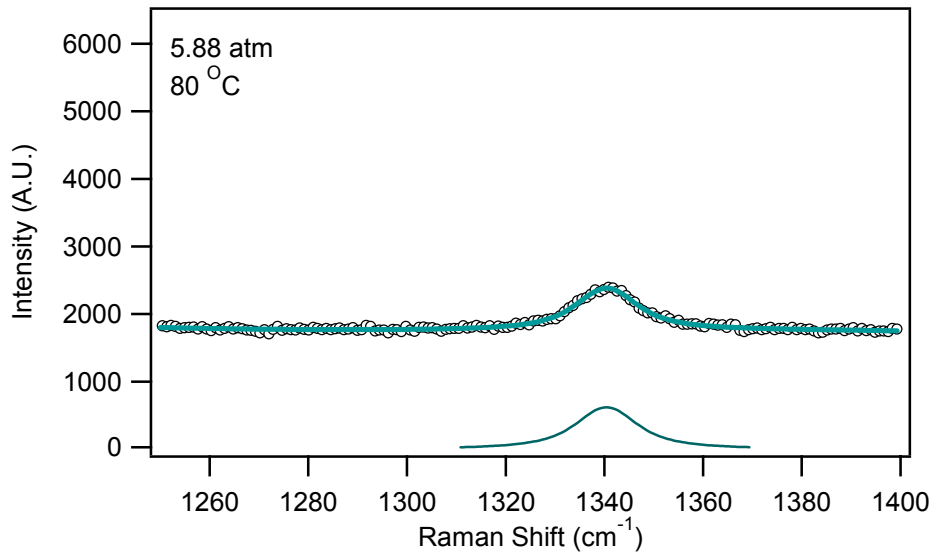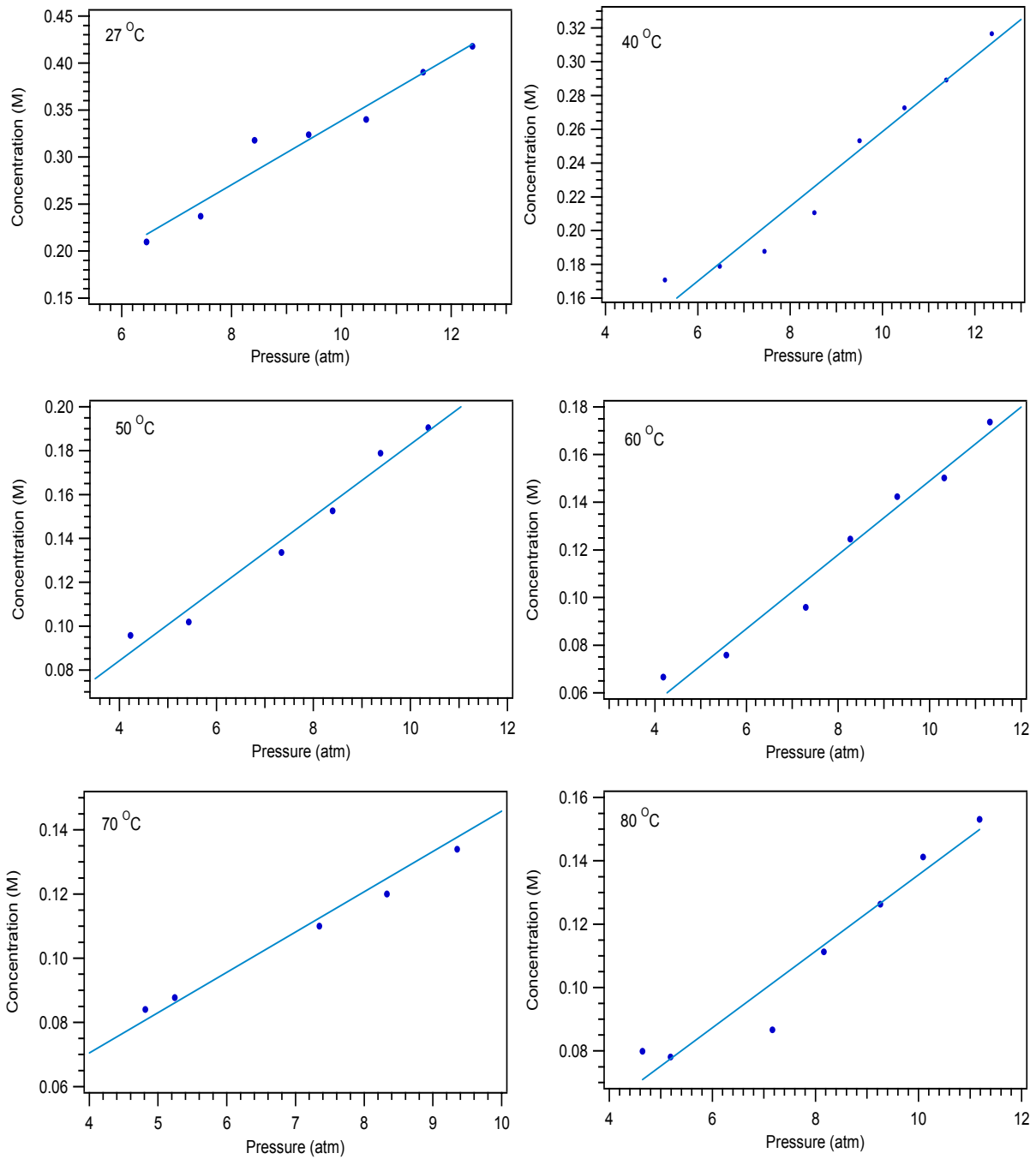
Figure 5.4: The linear regression fits used to calculate Henry's law constants. The temperature varies from 27 to 80°C.

27 °C

654.9 kPa		754.6 kPa		854.0 kPa		954.0 kPa	
Raman Area	Deviation	Raman Area	Deviation	Raman Area	Deviation	Raman Area	Deviation
39380	2103.6	40526	1877.6	56746	1712.2	57829	1951.9
37610	2167.1	39853	2244.3	55473	1820.5	56159	2304.3
40467	1872.6	43916	1667.3	58018	2304.6	58095	1934.9
37271	1622.8	44882	1758.9	55265	1894.9	55019	2207.7
37256	2940.2	45406	2345.0	59879	2511.2	59485	2678.3
39530	1652.8	43800	1940.3	56178	1906.0	62153	2035.8

		1060.0 kPa		1165.0 kPa		1256.0 kPa	
		Raman Area	Deviation	Raman Area	Deviation	Raman Area	Deviation
		56513	1681.2	62711	1905.5	68684	2314.6
		58913	2021.8	65642	2134.6	70830	2774.3
		59191	1801.7	70483	2194.1	72565	1802.6
		63414	2032.6	71892	1816.5	75517	2079.2
		66732	1629.5	68940	1692.5	78086	1924.8

30 °C

547.2 kPa		656.9 kPa		755.8 kPa		858.9 kPa	
Raman Area	Deviation	Raman Area	Deviation	Raman Area	Deviation	Raman Area	Deviation
32144	2341.9	30706	1944.7	39104	2270.7	42004	2011.7
33153	2371.8	29630	2241.4	37602	1941.2	43101	2134.1
32061	1827.3	35254	2537.1	37755	1978.0	45906	1934.3
32795	1946.2	33058	1851.6	39419	2093.3	41415	1966.1
27902	2133.8	35615	2334.2	39159	1826.8	46629	2294.2
30708	2194.0	33897	1816.8	40096	1936.2		

960.0 kPa		1068.0 kPa		1159.0 kPa		1260.0 kPa	
Raman Area	Deviation	Raman Area	Deviation	Raman Area	Deviation	Raman Area	Deviation
45664	1759.8	52632	2030.1	60537	2031.7	62867	2001.6
50338	2504.3	52628	2049.0	60686	2204.8	67602	2033.6
48739	2013.8	56494	2006.5	60403	1888.1	64281	2247.3
50274	2174.8	55426	1964.6	62417	2269.5	68765	2134.9
49103	1949.0	53922	1960.7	65407	2289.3	67412	2398.2

Continued

Table 5.1: Fitted values for the Raman area of the $2v_2$-FD used to determine the Henry's law constant at 27 °C. The deviations are included. The 30 °C data was used for the calibration curve as shown in Figure 5.2.

Table 5.1 Continued 40 °C

536.5 kPa		657.0 kPa		755.1 kPa		864.4 kPa	
Raman Area	Deviation	Raman Area	Deviation	Raman Area	Deviation	Raman Area	Deviation
34226	1890.4	30812	2193.9	32896	2008.1	35485	2174.8
34292	2229.5	32740	2283.6	35094	2088.8	37000	1861.4
33322	1323.3	33542	2015.9	34909	1862.0	41874	2061.2
27526	1877.0	31693	1922.3	33379	2033.3		
25957	1950.3	33815	2190.8				

963.8 kPa		1062 kPa		1154.0 kPa		1254.0 kPa	
Raman Area	Deviation	Raman Area	Deviation	Raman Area	Deviation	Raman Area	Deviation
46378	1810.2	41234	11238	51401	2084.9	55176	1814.1
45590	1840.3	47163	2043.4	53648	2212.4	55264	2169.1
44718	2068.2	49850	1957.7	51080	1826.0	59773	2186.6
46538	34974.2	47968	2028.8	51887	1900.0	55845	1644.2
46056	1734.8	47117	1999.4			58235	2167.8

50 °C

539.0 kPa		660.5 kPa		854.5 kPa		961.2 kPa	
Raman Area	Deviation	Raman Area	Deviation	Raman Area	Deviation	Raman Area	Deviation
17750	1112.7	19524	1060.4	23073	1063.1	26991	1065.86
17398	1167.8	17110	2032.9	25595	12007.8	28202	1134.1
17339	965.6	18319	1123.7	22272	1290.8	27717	1086.8
17355	1008.4	19363	1035.5	24984	15127.8	28575	1022.8
18413	1000.1	20254	1092.6	25546	3591.87		
18753	893.4			25592	1085.06		

1061.0 kPa		1161.0 kPa	
Raman Area	Deviation	Raman Area	Deviation
31830	128897.0	32024	999.97
31857	1206.7	34185	1110.43
31451	1197.3	35150	1180.37
33404	1289.0	36408	1187.74
34027	949.54	35062	1002.54

Continued

Table 5.1 Continued   60 $^{\text{O}}$C

532.2 kPa		671.5 kPa		847.6 kPa		945.9 kPa	
Raman Area	Deviation	Raman Area	Deviation	Raman Area	Deviation	Raman Area	Deviation
11917	974.4	14920	1259.7	17868	2360.0	22629	2.9x10^7
11578	1023.9	12672	1050.7	16829	938.8	21931	924.7
11784	809.3	14849	996.1	17495	1021.6	22973	1167.9
12565	1051.4	12674	1079.7	19191	1156.9	22711	1075.2
14977	1217.2	14419	1153.0			24278	958.2
12734	987.3						

		1050.0 kPa		1154.0 kPa		1255.0 kPa	
		Raman Area	Deviation	Raman Area	Deviation	Raman Area	Deviation
		25635	1202.2	25498	1329.85	31881	1563.78
		26437	1017.1	27773	1.1x10^6	31944	1086.88
		24915	1180.3	27292	1343.03	30958	1227.03
		27245	1237.1	28865	1425.94	31574	1106.57
				27798	1241.68		

70 $^{\text{O}}$C

596.1 kPa		639.5 kPa		852.7 kPa		952.4 kPa	
Raman Area	Deviation	Raman Area	Deviation	Raman Area	Deviation	Raman Area	Deviation
19746	1330.5	16075	1669.4	19892	1615.1	22027	1604.5
19256	1212.9	16261	1658.0	19609	1461.5	20094	1449.8
17600	1076.9	15722	3630.5	19929	1314.0	25538	7961.3
18475	1232.6	16763	1463.8	21954	1410.7	20776	1342.1
16928	1228.1	16124	1347.9				
1580	1211.1	15821	1128.2				

		1056.0 kPa		1246.0 kPa	
		Raman Area	Deviation	Raman Area	Deviation
		23265	1606.2	27099	1359.0
		23696	1209.1	31555	1342.1
		26791	1.5x10^8	29397	1455.7
		25210	1469.0	30787	1496.3
		23916	1638.5	30666	1241.2

Continued

Table 5.1 Continued   80 ^{O}C

587.5 kPa		642.7 kPa		842.8 kPa		944.0 kPa	
Raman Area	Deviation	Raman Area	Deviation	Raman Area	Deviation	Raman Area	Deviation
18919	926.6	14073	1250.9	14826	1358.8	19746	871.66
16028	1179.2	14864	1105.5	16366	1153.8	19611	1334.3
16980	726.9	12797	1130.1	16771	979.0	20939	1174.9
13904	877.8	15251	1143.6	16919	1163.1	21089	1219.4
14182	1013.3	15388	915.3			21439	1563.7
13711	813.3	15604	1133.19				

1055.0 kPa		1139.0 kPa		1250.0 kPa	
Raman Area	Deviation	Raman Area	Deviation	Raman Area	Deviation
21922	1318.1	24709	1147.99	26740	1193.4
21778	1244.9	26215	1127.75	24946	1235.41
23141	1376.7	26338	1168.11	28489	1393.92
23639	1065.3	26419	1269.78	27801	1246.05
24419	1431.44	25595	1349.86	29505	1247.16

Temperature $\pm 2^{\circ}C$	Henry's Law Constant M/atm
27	$(3.41 \pm 0.34) \times 10^{-2}$
40	$(2.22 \pm 0.18) \times 10^{-2}$
50	$(1.64 \pm 0.13) \times 10^{-2}$
60	$(1.55 \pm 0.12) \times 10^{-2}$
70	$(1.26 \pm 0.090) \times 10^{-2}$
80	$(1.21 \pm 0.14) \times 10^{-2}$

Table 5.2: Henry's law constants determined over a temperature range of 27 to 80 $^{\circ}$C.

Temperature °C	Henry's Law Constant M/atm	References
27	3.164×10^{-2}	Lisal
30	3.017×10^{-2}	Harned
	3.012×10^{-2}	Harned
	2.837×10^{-2}	Duan
40	2.400×10^{-2}	Harned
50	1.976×10^{-2}	Harned
	1.963×10^{-2}	Harned
60	1.043×10^{-2}	Duan

Table 5.3: Henry's law constants from the literature compared against calculated Henry's law constants.

LIST OF REFERENCES

(1)   Retallack, G. J. Carbon dioxide and climate over the past 300 Myr, *Phil. Trans. R. Soc. Lond. A* **2002**, *360*, 659.

(2)   Zeebe, R. E.; Wolf-Gladrow, D. *CO_2 in Seawater: Equilibrium, Kinetics, Isotopes*; Elsevier Oceanography Series: New York, 2001.

(3)   Shirayama, Y.; Thornton, H. Effect of increased atmospheric CO_2 on shallow water marine benthos, *J. Geophys. Res.* **2005**, *110*, C09S08.

(4)   Teng, H.; Yamasaki, A.; Shindo, Y. The fate of CO_2 hydrate released in the ocean, *Int. J. Energy Res.* **1999**, *23*, 295.

(5)   Jena, N. R.; Mishra, P. C. An ab initio and density functional study of microsolvation of carbon dioxide in water clusters and formation of carbonic acid, *Theor. Chim. Acta* **2005**, *114*, 189.

(6)   Larsen, J.; Dahl-Jensen, D. Interior temperatures of the northern polar cap on Mars, *Icarus* **2000**, *144*, 456.

(7)   Miller, S. L.; Smythe, W. D. Carbon dioxide clathrate in the martian ice cap, *Science* **1970**, *170*, 531.

(8)   Longhi, J. Phase equilibrium in the system CO_2-H_2O: Application to Mars, *J. Geophys. Res.* **2006**, *111*, E06011.

(9)   Ferdows, M.; Ota, M. Molecular simulation study for CO_2 clathrate hydrate, *Chem. Eng. Technol.* **205**, *28*, 168.

(10)   Teng, H.; Yamasaki, A. Pressure-mole fraction phase diagrams for CO_2-pure water system under temperatures and pressures corresponding to ocean waters at depth to 3000 M, *Chem. Eng. Commun.* **2002**, *189*, 1485.

(11)   Maynard, B. Burning Questions about Gas Hydrates, *Chemistry* **2006**, 27.

(12)   Teng, H.; Yamasaki, A. Can CO_2 hydrate deposited in the ocean always reach the seabed?, *Energy Convers. Mgmt.* **1998**, *39*, 1045.

(13)   Aya, I.; Yamane, K.; Yamada, N. Simulation experiment of CO_2 Storage in the basin of deep ocean, *Energy Convers. Mgmt.* **1995**, *36*, 485.

(14)   Circone, S.; Stern, L. A.; Kirby, S. H.; Durham, W. B.; Chakoumakos, B. C.; Rawn, C. J.; Rondinone, A. J.; Ishii, Y. CO_2 Hydrate: Synthesis, composition, structure, dissociation behavior, and a comparison to Structure I CH_4 Hydrate, *J. Phys. Chem. B* **2003**, *107*, 5529.

(15)   E. Dendy Sloan, J. Clathrate Hydrates: The Other Common Solid Water Phase, *Ind. Eng. Chem. Res.* **2000**, *39*, 3123.

(16)   Uchida, T. Physical property measurements on CO_2 clathrate hydrates. Review of crystallography, hydration number, and mechanical properties, *Waste Management* **1997**, *17*, 343.

(17)   Rudolph, W. W.; Fischer, D.; Irmer, G. Vibrational Spectroscopic Studies and Density Functional Theory Calculations of Speciation in the CO2-Water System, *Appl. Spectrosc.* **2006**, *60*, 130.

(18)   Maillet, J.-B.; Boutin, A.; Buttefey, S. From molecular clusters to bulk matter. I. Structure and thermodynamics of small CO_2, N_2, and SF_6 clusters, *J. Chem. Phys.* **1998**, *109*, 329.

(19)   Koh, C. A. Towards a fundamental understanding of natural gas hydrates, *Chem. Soc. Rev.* **2002**, *31*, 157.

(20)   Subramanian, S.; E. Dendy Sloan, J. Trends in Vibrational Frequencies of Guests Trapped in Clathrate Hydrate Cages, *J. Phys. Chem. B* **2002**, *106*, 4348.

(21)   Englezos, P. Clathrate Hydrates, *Ind. Eng. Chem. Res.* **1993**, *32*, 1251.

(22)   E. Dendy Sloan, J. *Clathrate Hydrates of Natural Gases*, 2nd ed.; Marcel Dekker, Inc.: New York, New York, 1998.

(23)   E. Dendy Sloan, J. Gas Hydrates: Review of Physical/Chemical Properties, *Energy Fuels* **1998**, *12*, 191.

(24)   Khan, A. Theoretical studies of $CO_2(H_2O)_{20,24,28}$ clusters: stabilization of cages in hydrates by CO_2 guest molecules, *J. Mol. Struct. (THEOCHEM)* **2003**, *664-665*, 237.

(25)   Falcke, H.; Eberle, S. H. Raman Spectroscopic Identification of Carbonic Acid, *Water Res.* **1990**, *24*, 685.

(26)   Abbott, T. M.; Buchanan, G. W.; Kruus, P.; Lee, K. C. 13C nuclear magnetic resonance and Raman investigations of aqueous carbon dioxide systems, *Can. J. Chem.* **1982**, *60*, 1000.

(27)   Waals, J. H. v. d.; Platteeuw, J. C. *Clathrate Solutions*; Interscience Publishers, Inc.: New York, 1959; Vol. II.

(28)   Ingle, James D.; Crouch, S. R. *Spectrochemical Analysis*; Prentice-Hall, Inc.: Upper Saddle River, NJ, 1988.

(29)   McCreery, R. L. *Raman Spectroscopy for Chemical Analysis*; John Wiley & Sons: New York, 2000.

(30)   Pelletier, M. J. *Analytical Applications of Raman Spectroscopy*; Blackwell Science Ltd: Malden MA, USA, 1999.

(31)   Smith, E.; Dent, G. *Modern Raman Spectroscopy - A Practical Approach*; John Wiley & Sons, Inc.: England, 2005.

(32)   Adams, W. A.; Greer, G.; Desnoyers, J. E.; Atkinson, G.; Kell, G. S.; Oldham, K. B.; Walkley, J. *Chemistry and Physics of Aqueous Gas Solutions*; The Electrochemical Society, Inc.: USA, 1975.

(33)   Harris, D. C.; Bertolucci, M. D. *Symmetry and Spectroscopy: An Introduction to Vibrational and Electronic Spectroscopy*; Dover Publications, Inc.: New York, 1978.

(34)   Cotton, F. A. *Chemical Applications of Group Theory*, 3rd ed.; John Wiley & Sons: New York, 1990.

(35)   Montero, S. Raman intensities of Fermi diads. I. Overtones in resonance with nondegenerate fundamentals, *J. Chem. Phys.* **1983**, *79*, 4091.

(36)   Anderson, A. *The Raman Effect*; Marcel Dekker, Inc.: New York, 1971.

(37)   Tejeda, G.; Mate, B.; Montero, S. Overtone Raman spectrum and molecular polarizability surface of CO_2, *J. Chem. Phys.* **1995**, *103*, 568.

(38)   Frantz, J. D. Raman spectra of potassium carbonate and bicarbonate aqueous fluids at elevated temperatures and pressures: comparison with theoretical simulations, *Chem. Geol.* **1998**, *152*, 211.

(39)   Wen, N.; Brooker, M. H. Ammonium Carbonate, Ammonium Bicarbonate, and Ammonium Carbamate Equilibria: A Raman Study, *J. Phys. Chem.* **1995**, *99*, 359.

(40)   Sato, H.; Matubayasi, N.; Nakahara, M.; Hirata, F. Which carbon oxide is more soluble? Ab initio study on carbon monoxide and dioxide in aqueous solution, *Chem. Phys. Lett.* **2000**, *323*, 257.

(41)   Uchida, T.; Takagi, A.; Mae, S.; Kawabata, J. Dissolution Mechanisms of CO_2 Molecules in Water Containing CO_2 Hydrates, *Energy Convers. Mgmt* **1997**, *38*, S307.

(42)   Sum, A. K.; Burruss, R. C.; E. Dendy Sloan, J. Measurement of Clathrate Hydrates via Raman Spectroscopy, *J. Phys. Chem. B* **1997**, *101*, 7371.

(43)   Roland, C. M.; Steele, W. A. Rotation-vibration CARS spectra of the $2v_2$ mode in CO_2 gas, *J. Chem. Phys.* **1981**, *74*, 2733.

(44)   Fleyfel, F.; Devlin, J. P. FT-IR spectra of carbon dioxide clusters, *J. Phys. Chem.* **1989**, *93*, 7292.

(45)   Olijnyk, H.; Daufer, H.; Jodi, H.-J. Effect of pressure and temperature on the Raman spectra of solid CO_2, *J. Chem. Phys.* **1988**, *88*, 4204.

(46)   Ikeda, T.; Mae, S.; Uchida, T. Effect of guest-host interaction on Raman spectrum of a CO_2 clathrate hydrate single crystal, *J. Chem. Phys.* **1998**, *108*, 1352.

(47)   Demetriou, M. D.; Ghoniem, N. M.; Lavine, A. S. Effects of nucleation transience on crystallization kinetics under strongly nonequilibrium conditions, *J. Chem. Phys.* **2002**, *117*, 10739.

(48)   Hirai, S.; Okazaki, K.; Tabe, Y.; Kawamura, K. CO_2 clathrate-hydrate formation and its mechanism by molecular dynamics simulation, *Energy Convers. Mgmt.* **1997**, *38*, S301.

(49)   Sloan, E. D. Clathrate hydrate measurements: microscopic, mesoscopic, and macroscopic, *J. Chem. Thermodyn.* **2003**, *35*, 41.

(50)   Henning, R. W.; Schultz, A. J.; Thieu, V.; Halpern, Y. Neutron Diffraction Studies of CO_2 Clathrate Hydrate: Formation from Deuterated Ice, *J. Phys. Chem. A* **2000**, *104*, 5066.

(51)   Kawamura, T.; Komai, T.; Yamamoto, Y.; Nagashima, K.; Ohga, K.; Higuchi, K. Growth Kinetics of CO_2 hydrate just below melting point of ice, *J. Cryst. Growth* **2002**, *234*, 220.

(52)   Buanes, T.; Kvamme, B.; Svandal, A. Computer Simulation of CO_2 hydrate growth, *J. Cryst. Growth* **2006**, *287*, 491.

(53)   Gopalakrishnan, S.; Liu, D.; Allen, H. C.; Kuo, M.; Shultz, M. J. Vibrational spectroscopic studies of aqueous interfaces: salts, acids, bases, and nanodrops, *Chem. Rev.* **2006**, *106*, 1155.

(54)   Walrafen, G. E. Effects of equilibrium H-bond distance and angle changes on Raman intensities from water, *J. Chem. Phys.* **2004**, *120*, 4868.

(55)   Schicks, J. M.; Erzinger, J.; Ziemann, M. A. Raman spectra of gas hydrates-differences and analogies to ice Ih and (gas saturated) water, *Spectrochim. Acta, Part A* **2005**, *61*, 2399.

(56)   Devlin, J. P. Structure, specta, and mobility of low-pressure ices: Ice I, amorphous solid water, and clathrate hydrates at T<150 K, *J. Geophys. Res.* **2001**, *106*, 33333.

(57)   Someya, S.; Bando, S.; Chen, B.; Song, Y.; Nishio, M. Measurement of CO_2 solubility in pure water and the pressure effect on it in the presence of clathrate hdyrate, *Int. J. Heat Mass Transfer* **2005**, *48*, 2503.

(58)   Portier, S.; Rochelle, C. Modelling CO_2 solubility in pure water and NaCl-type waters from 0 to 300 ^{O}C and from 1 to 300 bar Application to the Utsira Formation at Sleipner, *Chem. Geol.* **2005**, *217*, 187.

(59)   Chapoy, A.; Mohammadi, A. H.; Chareton, A.; Tohidi, B.; Richon, D. Measurement and modeling of gas solubility and literature review of the properties for the carbon dioxide-water system, *Ind. Eng. Chem. Res.* **2004**, *43*, 1794.

(60)   Finlayson-Pitts, B. J.; James N. Pitts, J. *Chemistry of the Upper and Lower Atmosphere: Theory, Experiments, and Applications*; Academic Press: San Diego, CA, 1999.

(61)   Brown, T. L.; H. Eugene LeMary, J.; Bursten, B. E.; Burdge, J. R. *Chemistry: The Central Science*, 9th ed.; Pearson Education, Inc.: Upper Saddle River, NJ, 2003.

(62)   Harned, H. S.; Raymond Davis, J. The ionization constant of carbonic acid in water and the solubility of carbon dioxide in water and aqueous salt solutions from 0 to 50°, *J. Am. Chem. Soc.* **1943**, *65*, 2030.

(63)   Duan, Z.; Sun, R.; Zhu, C.; Chou, I.-M. An improved model for the calculation of CO_2 solubility in aqueous solutions containing Na^+, K^+, Ca^{2+}, Mg^{2+}, Cl^-, and SO_4^{2-}, *Mar. Chem.* **2006**, *98*, 131.

(64)   Lisal, M.; Smith, W. R.; Aim, K. Analysis of Henry's constant for carbon dioxide in water via Monte Carlo simulation, *Fluid Phase Equilib.* **2004**, *226*, 161.

(65)   Kaufmann, K. Choosing Your Detector. In *OE Magazine*, 2006.

(66)   Kaufmann, K. Light Levels and Noise. In *Photonics Spectra*, 2000; 149.

(67)   McHale, Jeanne L. *Molecular Spectroscopy*; Prentice Hall: Upper Saddle River, NJ, 1999.

(68)   Wendland, M.; Hasse, H.; Maurer, Experimental pressure vs. temperature data on three- and four-phase equilibria of fluid, hydrate and ice phases in the system carbon dioxide-water. G. *J. Chem. Eng. Data* 1999, 44, 901.

APPENDIX A

PHOTOMULTIPLIER TUBE EXPERIMENTS

A.1.   Introduction

A shift of less than two wavenumbers is what distinguishes solvated CO_2 vibrational modes from CO_2 clathrate vibrational modes. Therefore, the detection system must be very accurate. The Andor CCD camera that was originally used for the clathrate experiments has a resolution of 7 cm^{-1} and does not have the accuracy needed. A more accurate system is required to verify the experimental parameters used are sufficient to form CO_2 clathrates. One possible way to solve this problem is to use a photomultiplier tube (PMT). A PMT has extremely high sensitivity and low noise compared to other photosensitive devices. The high sensitivity and low noise could provide a better resolution through a decrease of the slit widths. A brief discussion of the PMT follows.

A.2   PMT Background

A PMT (Figure A.1) is composed of a photoemissive cathode (photocathode), an electron multiplier (dynodes), and an electron collector (anode) in a vacuum tube. The PMT uses the photoelectric effect to convert optical photons into photoelectrons when radiation enters the photocathode. These photoelectrons are emitted and accelerated toward an increasingly more positive series of dynodes. The secondary electron emission

process that occurs at each dynode results in a "cascading effect" or amplification of electrons.[28,65,66]

This amplification process results in a large charge packet at the anode for each photoelectron collected by the first dynode. By the time the electrons have left the last dynode and are collected at the anode, they have been amplified by a factor of 10^6. This current amplification is also known as the gain.[28] The gain, μ, is the average number of electrons per anode pulse and depends highly on the power supply voltage, as shown in Equation 1:

$$\mu = \frac{A^n}{(n+1)^{\alpha n}} \cdot V^{\alpha n}$$

(1)

where A is a constant, n is the number of dynodes, α is a constant determined by the structure and material of the electrodes, and V is the supply voltage. Due to the high internal gain, a PMT can detect low-level signals.

The PMT conversion efficiency or radiant sensitivity is dependent upon the photocathode material. The dynodes are made of a secondary emission material that establishes the energy threshold. If the photons entering the photocathode have energy greater than the threshold energy, the photoelectrons escape the dynodes. The production probability of photoelectrons emitted when one photon strikes the photocathode is called the quantum efficiency[28] and is shown in Equation 2

$$QE = \frac{S \times 1240}{\lambda} \times 100$$

(2)

where S is the cathode radiant sensitivity in A/W at a given wavelength λ in nm. Due to its dependence on wavelength, the photocathode chosen for this experiment must have

maximum quantum efficiency at 574 nm. The cathode radiant sensitivity and quantum

efficiency of the PMT used for experiments are shown in Figure A.2.

A.3.   Experimental Setup

The experimental setup is shown in Figure A.3. A 532 nm continuous wave

(CW) laser (Spectra-Physics, Millennia II) was used to obtain spectra. A fiber optic

probe (InPhotonics, RP 532-05-15-FC) was used to both deliver the laser excitation

source to the sample and to collect the scattered light. The scattered light was delivered

to the entrance slit of a 500 mm monochromator (Acton Research, SpectraPro 500i) via a

200 μm collection fiber optic (InPhotonics, Inc.). The scatter was dispersed using a 1200

g/mm grating blazed at 500 nm, and data was collected to a photomultiplier tube

(Hamamatsu Photonics, R3896, multi-alkali, side-on, UV glass window). The voltage

was supplied to the PMT via a power supply (Spectral Products, AD110B Photobyte-P).

A virtual instrument program (LabVIEW 7.1) was used to collect and display the data.

Data was evaluated using Igor Pro (Wavemetrics, Version 4.0.5.1). Section A.4

describes the procedure used to optimize the PMT detection setup.

A.4.   Determining the Experimental Parameters

The PMT was calibrated using the 475.8 nm line from a fluorescent light and the

wavenumber position was confirmed by taking a spectrum of naphthalene. The peak

positions of fluorescent light and naphthalene were compared to the literature values. [29]

The fluorescent light spectrum was obtained using 200.0 μm entrance and exit slit widths

and a spectral range of 575 to 579 nm (Figure A.4). The 1382 cm^{-1} peak of naphthalene

(Figure A.5) was obtained with 100.0 μm entrance and exit slit widths over a spectral range of 574 to 578 nm. A 0.01 nm step size, and a PMT integration period consisting of 1,000 scans was used for both spectra.

The gain to be used for the experiments was determined by obtaining spectra of naphthalene with 150.0 μm entrance and exit slit widths. The spectral range covered 574 to 577 nm. A 0.5 nm step size and a PMT integration period consisting of 500 scans were used. Gains of 2, 4, 8, and 16 were tested, Figure A.6. As the gain increased, the S/N ratio improved. It was concluded that a gain of 16 resulted in the best S/N and would be used for future PMT experiments.

Initial solvated CO_2 spectra were obtained using a spectral region of 572 to 576 nm with a 0.20 nm step size. A PMT integration period of 1000 scans was used. A stainless steel cell was filled with 100.0 mL of nano-pure water (18.2 MΩ•cm). A pressure transducer (MKS PDR2000 Dual Capacitance Manometer) was used to verify the cell pressure was maintained at 12.73 atm. The entrance and exit slits were adjusted simultaneously to determine the appropriate slit width to be used for experiments. A solvated CO_2 peak was not observed until slit widths of 500 μm were reached. (Figure A.7) A reproducible peak was not observed until 650 μm due to low S/N.

A resolution experiment was performed to determine if 650 μm slit widths provided a better resolution than the CCD camera. The resolution of the PMT was determined by using the 1382 cm^{-1} peak of naphthalene. The step size was 0.01 nm and the spectral range covered 572 to 576 nm. A PMT integration period consisting of 1,000 scans was used. The entrance and exit slits were adjusted from 30.0 μm to 450.0 μm, simultaneously. The data was fit with a Voigt function. The FWHM of the 1382 cm-1

peak was determined for each slit width, Figure A.8. The FWHM was plotted as a function of the slit width. For slit widths below 50 μm, a poor fit due to low S/N resulted in inaccurate FWHM determinations. The near level slope at 5 cm^{-1} shows the FWHM is nearly constant for several slit widths indicating this FWHM is the minimum resolution. In addition, the slope indicates a slit width below 100 μm will not improve the resolution. The 100 μm slit width was used for experiments.

Further reduction of the slit width was attempted by increasing the integration period of the PMT and by taking the average of several spectra. It was hoped that increasing the integration period and taking an average of ten to seventeen spectra would enhance the S/N. The integration period of the PMT was adjusted from 1,000 scans to 100,000 scans. For each integration period, a spectrum was acquired using a 450 μm slit width and a 0.5 nm step size. The data was fit with a Voigt function. Although increasing the integration period of the PMT improved the S/N slightly, the integration time increased from minutes to hours, Figure A.9.

Experiments were done varying the PMT integration period from 100 scans to 1,000 scans while averaging ten spectra. The experimental parameters remained the same. Standard deviations of the averages were calculated and are shown in the plots. Obtaining an average of several spectra (Figure A.10) with shorter integration periods actually improved the S/N more than just varying the integration time but still not enough to reduce the slit width.

Neither increasing the PMT integration time nor averaging the spectra decreased the slit width to the needed 100 μm indicated by the resolution study. The last experiment to decrease the slit width involved increasing the laser energy from 148 mW to 201 mW.

The slit width was set at 100 μm and a step size of 0.1 nm was used. The PMT

integration was 10,000 scans and seventeen spectra were averaged. The resulting spectra

indicated solvated CO_2 peaks could be observed with an input laser energy of 201 mW.

Standard deviations of the averages were calculated and are shown in Figure A.11.

Energies below 201 mW were insufficient at 100 μm to observe a solvated CO_2 peak.

Since such a high energy was required to obtain data, it was necessary to determine if

the energy required to obtain data would destroy the sample. The CCD camera was used

with a shorter integration time of 90 s due to its improved S/N. A slit width of 50 μm and

a 1200 g/mm grating were used to acquire the spectrum. SpectraSense software (Acton

Research, version 4.2.9) acquired spectra. An input of energies from 77 mW to 180 mW

was used. The stainless steel cell was filled with 100.0 mL of nanopure water (18.2

$M\Omega \cdot cm$). The cell was kept at $-15 \pm 2\ ^0C$ and allowed to freeze. During the experiment,

the cell temperature was maintained while the cell was exposed to the laser for the entire

experiment. The stretching region of $H_2O_{(s)}$ (2900–3800 cm^{-1}) was evaluated for up to

three hours. A decrease in intensity of the ~3051 cm^{-1} peak and an increase in the ~3300

cm^{-1} peak would indicate the ice was melting. Refer to Chapter 3 for vibrational

assignments. However, even at the highest energy the shape of the peaks did not change

for three hours indicating the laser energy was not sample destructive, Figure A.12.

A.5.   Conclusion

Data obtained with the PMT and LabVIEW VI is reproducible and indicates the

PMT setup works correctly. However, the resolution was not improved over the use of

91

the Roper Scientific CCD camera. The Roper Scientific monochromator with CCD

camera will be used in future experiments.
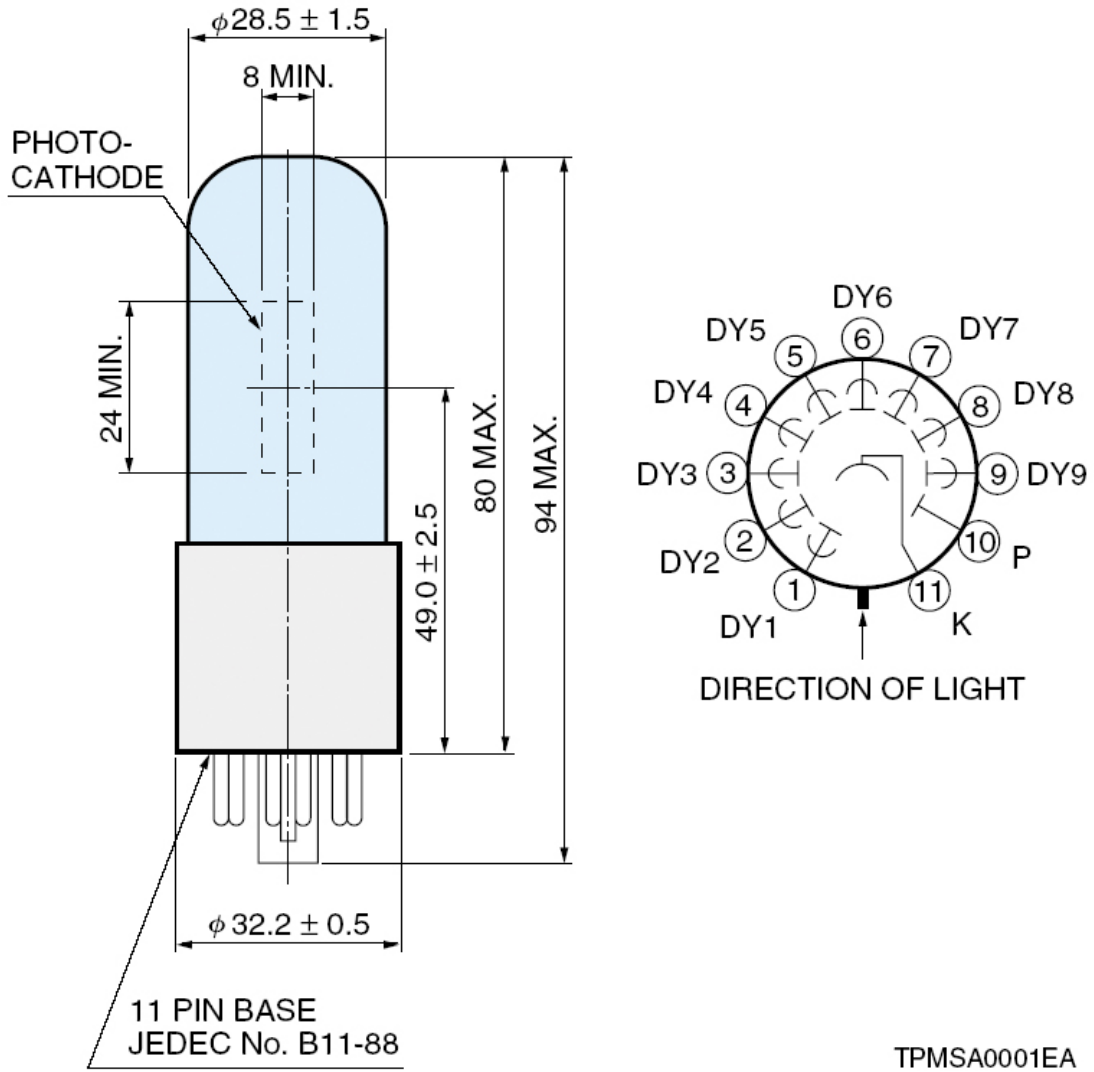
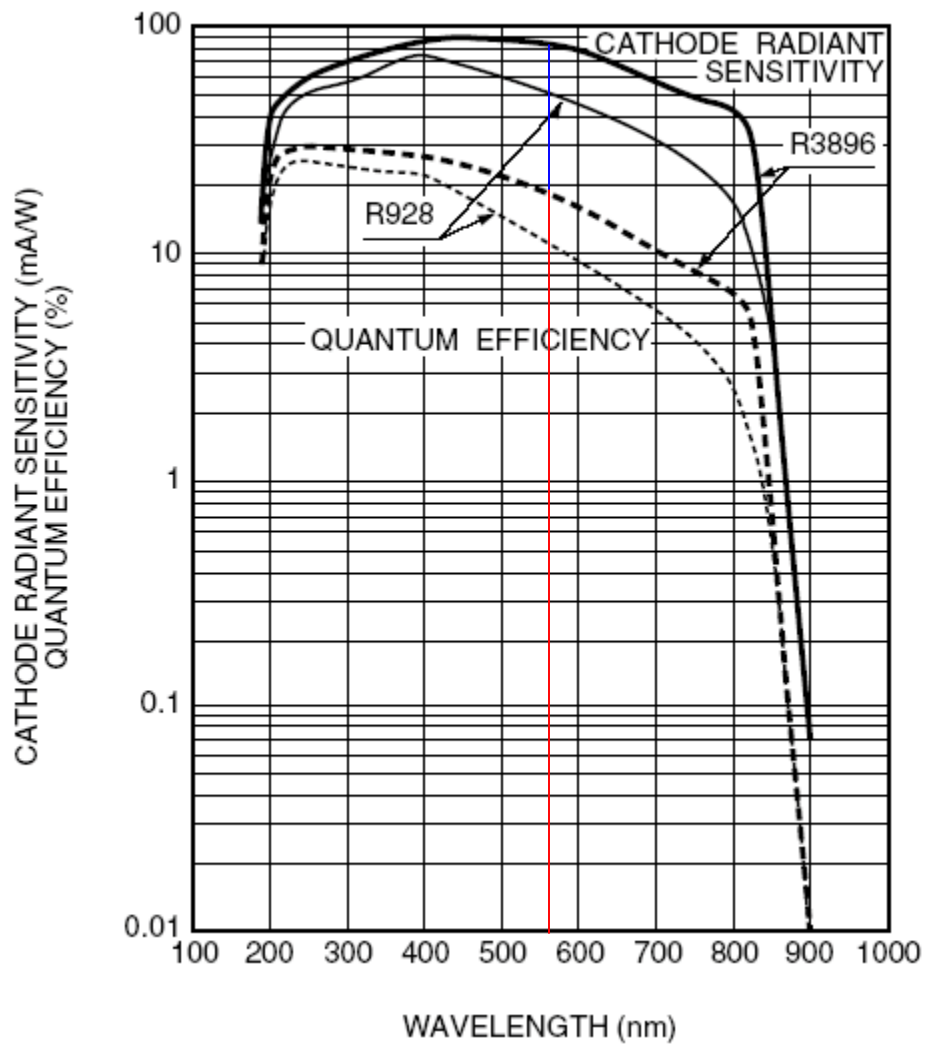**Figure A.1: Diagram of the R3896 PMT with a closeup of the dynodes. (www.sales.hamamatsu.com)**

Figure A.2: The cathode radiant sensitivity (blue) and the quantum efficiency (red) of the R3896 PMT at 574 nm. (www.sales.hamamatsu.com)
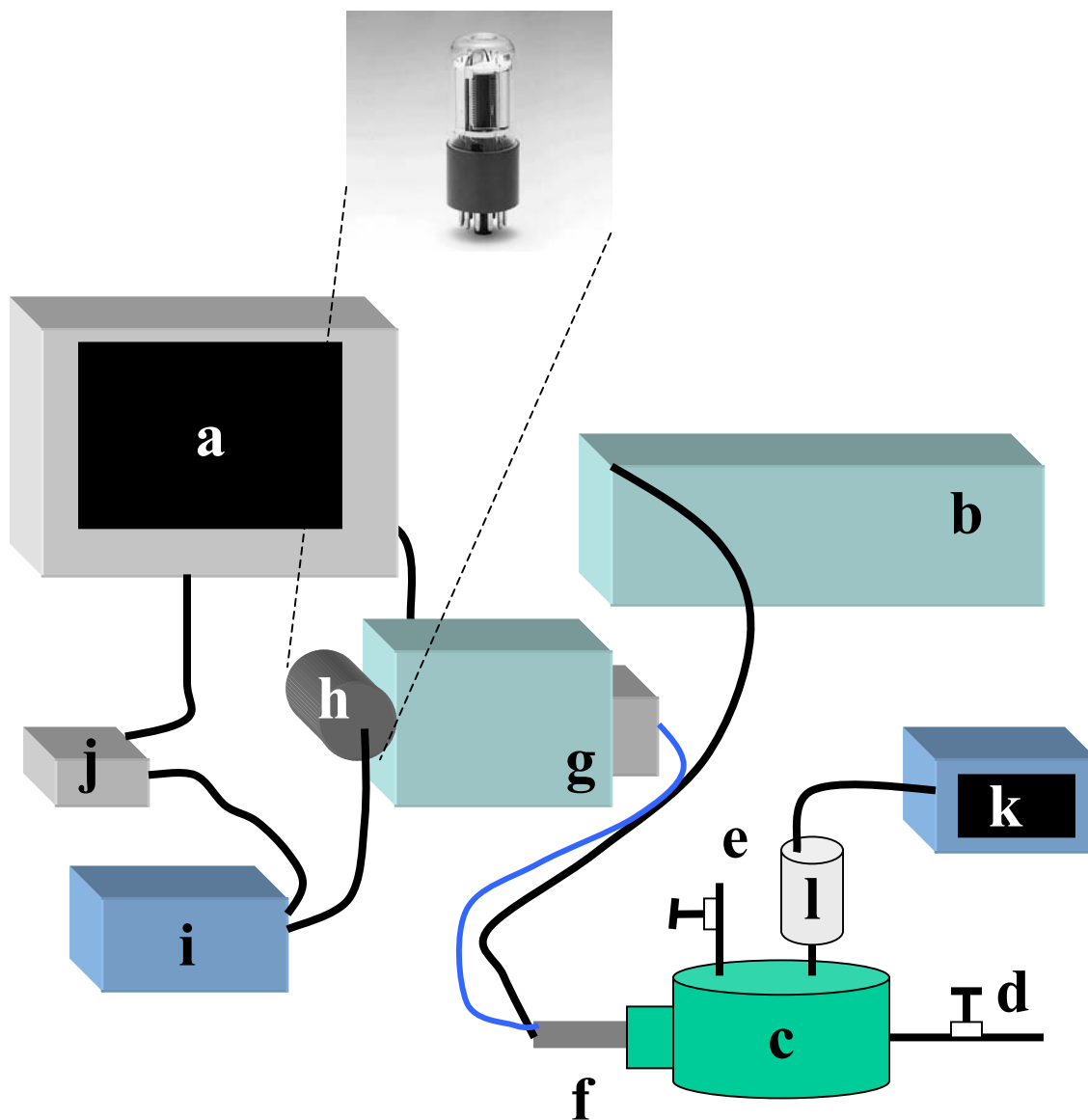
Figure A.3: Schematic of PMT Raman setup: (a) computer; (b) Spectra-Physics Millenia II laser; (c) stainless steel cell; (d) gas inlet valve; (e) gas outlet valve; (f) fiber optic Raman probe; (g) monochromator; (h) photomultipler tube; (i) AD110B power supply; (j) A/D connector; (k) MKS PDR2000 Dual Capacitance Manometer; (l) pressure transducer. The inset shows a picture of the R3896 PMT. (www.sales.hamamatsu.com)
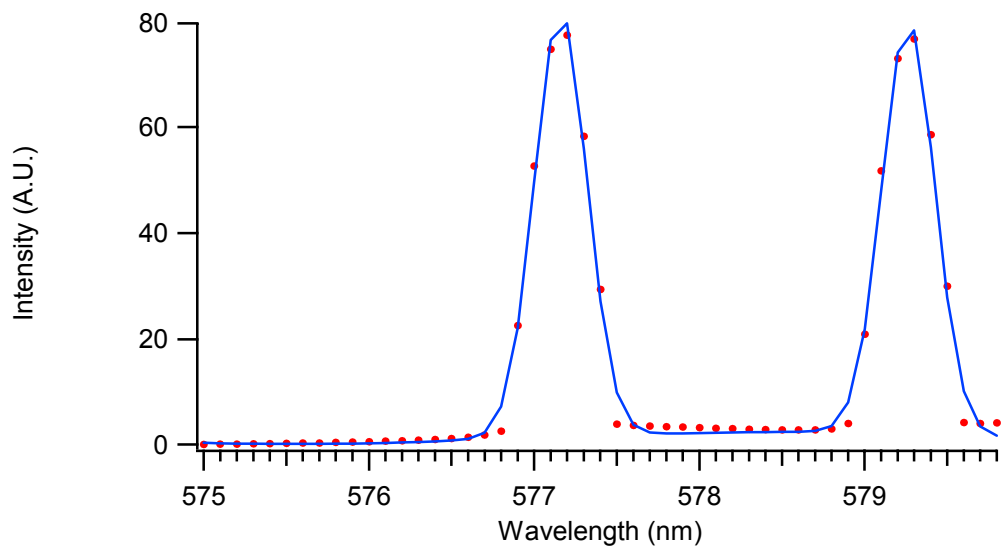
Figure A.4: Spectrum of fluorescent light showing the 577 and 579 nm lines obtained with a 200 μm slit width, a 0.01 nm step size, and a PMT integration period consisting of 1000 scans. The spectral fit is shown in blue.
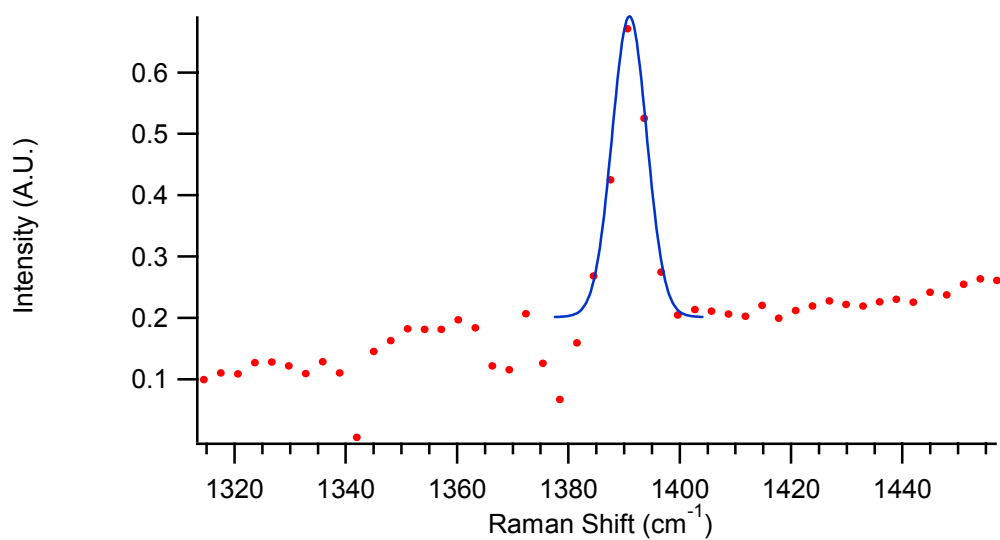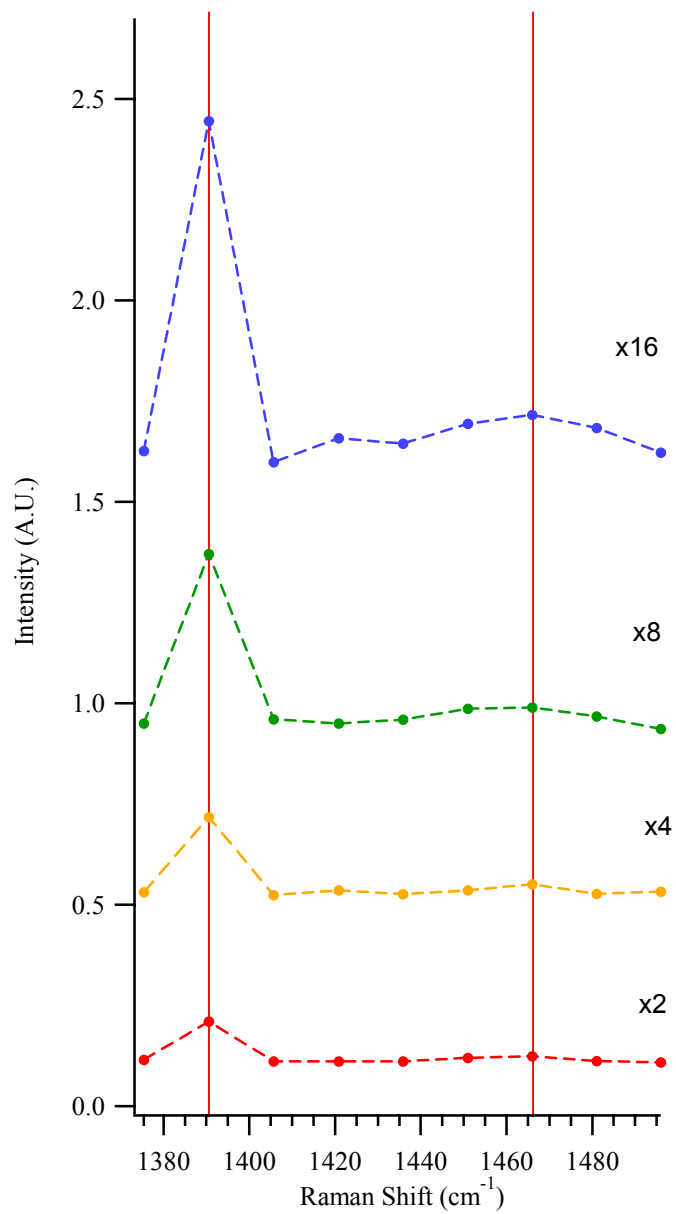
Figure A.5: Spectrum of naphthalene showing the 1382 cm^{-1} peak. The spectrum was obtained using a 100 μm slit width, a 0.01 nm step size, and a PMT integration period consisting of 1000 scans. The spectral fit is shown in blue.

Figure A.6: Naphthalene spectra were evaluated with varying gains, a 0.5 nm step size, and a PMT integration period consisting of 500 scans. The red lines indicate the 1390 and 1465 cm-1 peaks. As the gain increased, the S/N increased. The data are offset for easier observation.
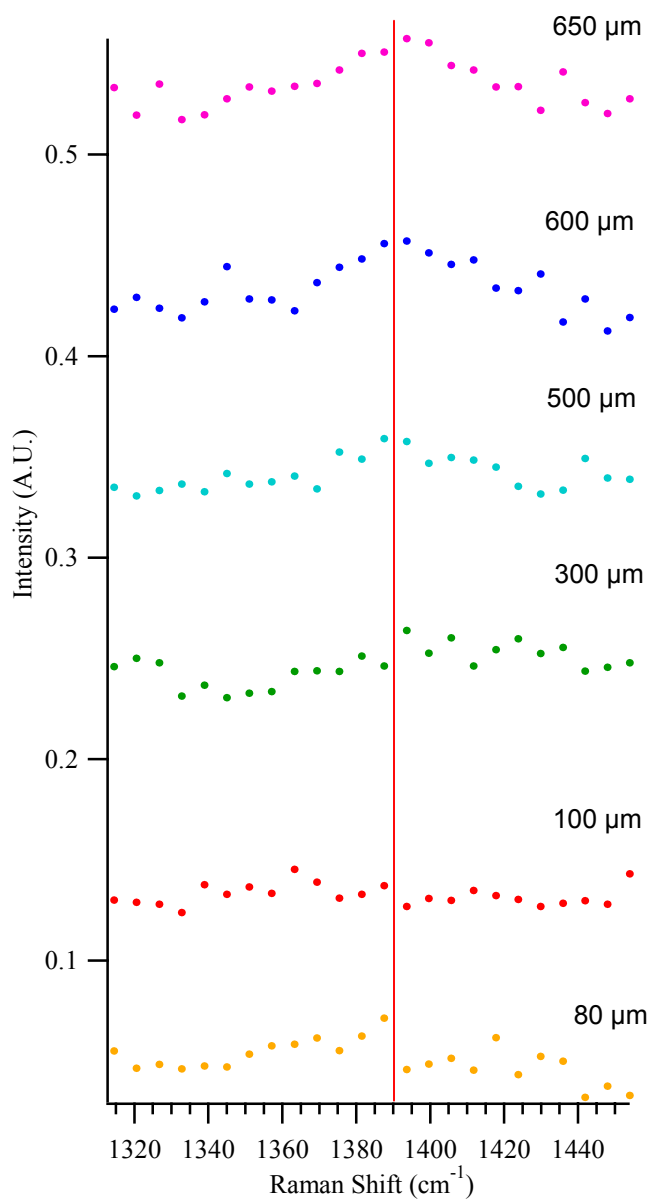
Figure A.7: Solvated CO$_2$ spectra acquired using the PMT while varying the entrance and exit slits, simultaneously. A PMT integration period consisting of 1000 scans and a 0.2 nm step size was used to acquire spectra. The red line highlights the solvated CO$_2$ peak position at 1390 cm^{-1}. The data are offset for easier observation.
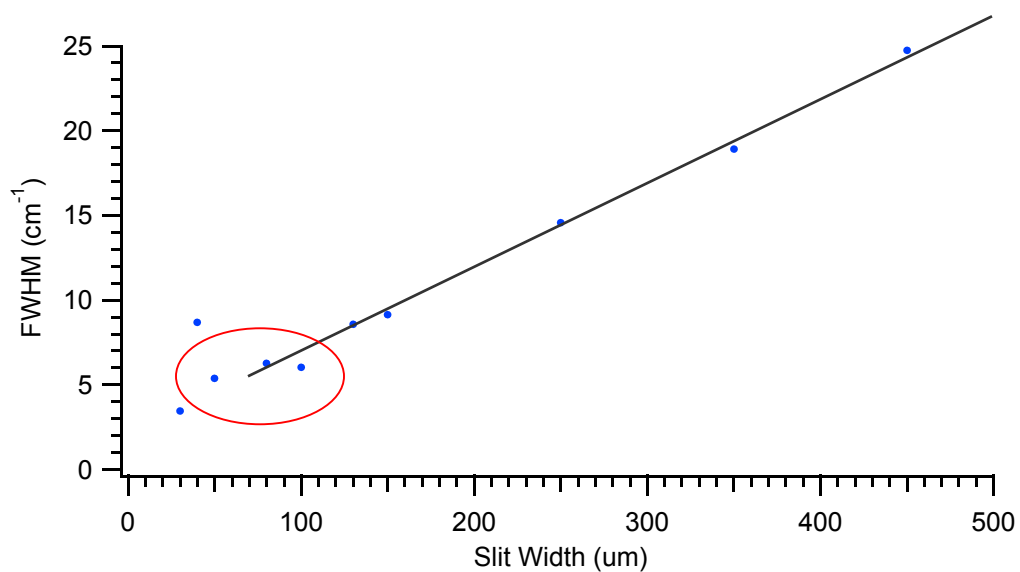
Figure A.8: **The FWHM of the 574 nm line of napthalene as a function of the slit width. Resolution was determined from the plot. Spectra were obtained using a 0.01 nm step size and a PMT integration period consisting of 1000 scans. The near level slope (red) indicates the minimum resolution of the PMT while the positive slope (black) indicates the resolution at other slit widths.**
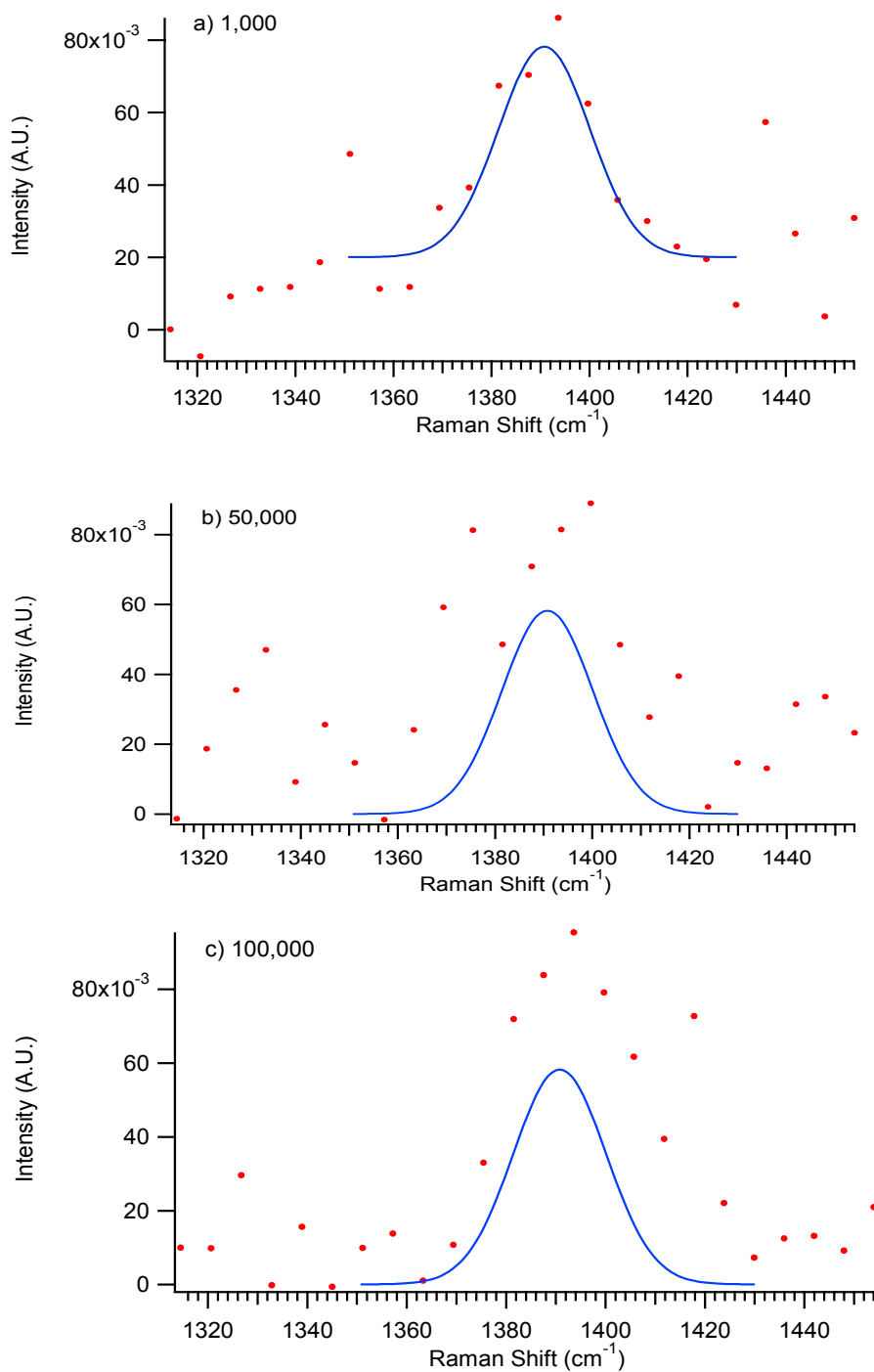
Figure A.9: Spectra of the solvated CO_2 peak obtained with a 450 um slit width and a 0.5 nm step size with PMT integration periods consisting of (a) 1,000, (b) 50, 000, and (c) 100,000 scans. The spectral fit is shown in blue.
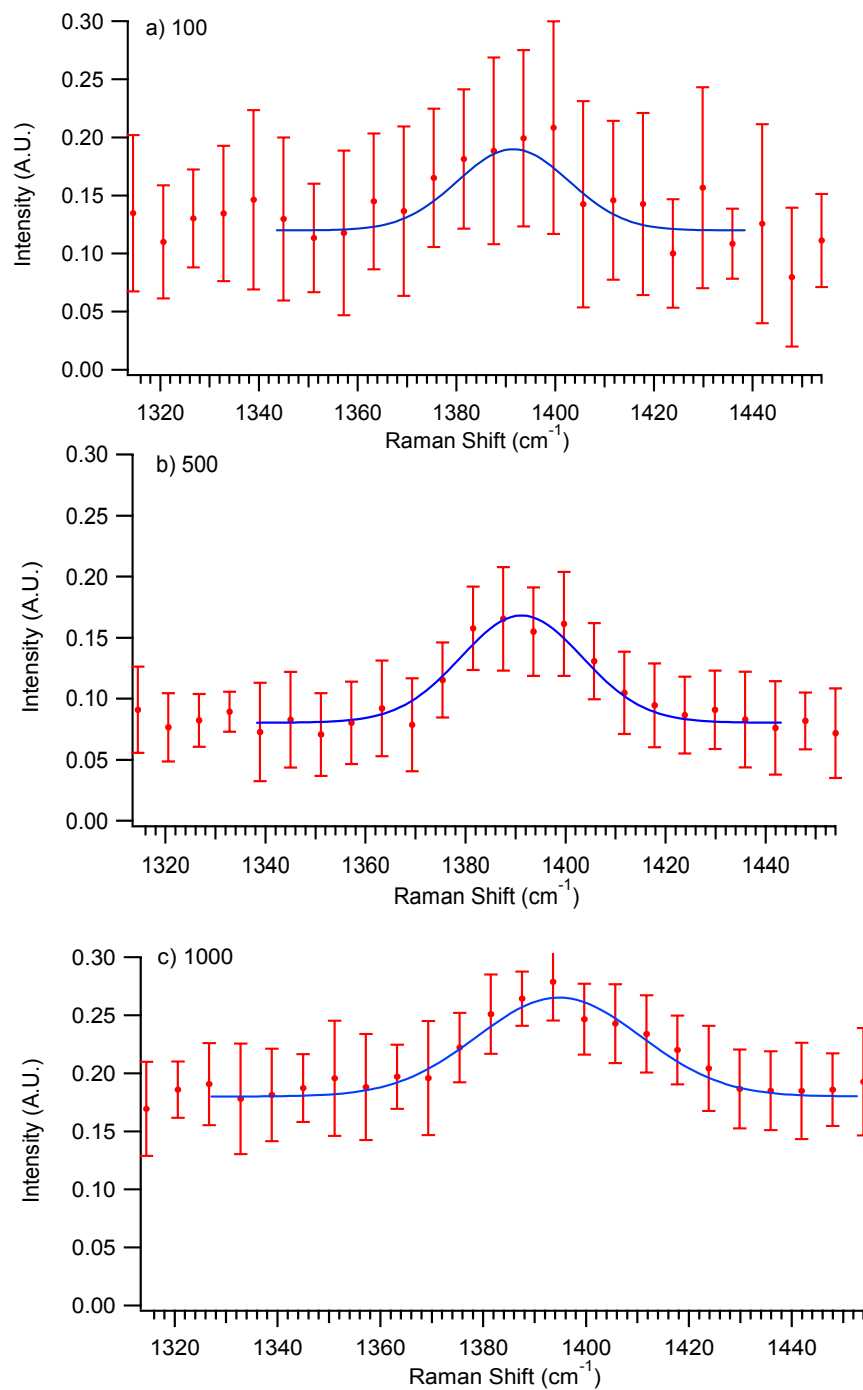
Figure A.10: Spectra of solvated CO$_2$ determined by averaging 10 spectra using different PMT integration periods consisting of (a) 100 Scans, (b) 500 Scans, and (c) 1,000 Scans. The spectra were obtained with a 450 um slit width and a 0.5 nm step size. The fits are shown in blue. Standard deviation error bars of the average are shown.
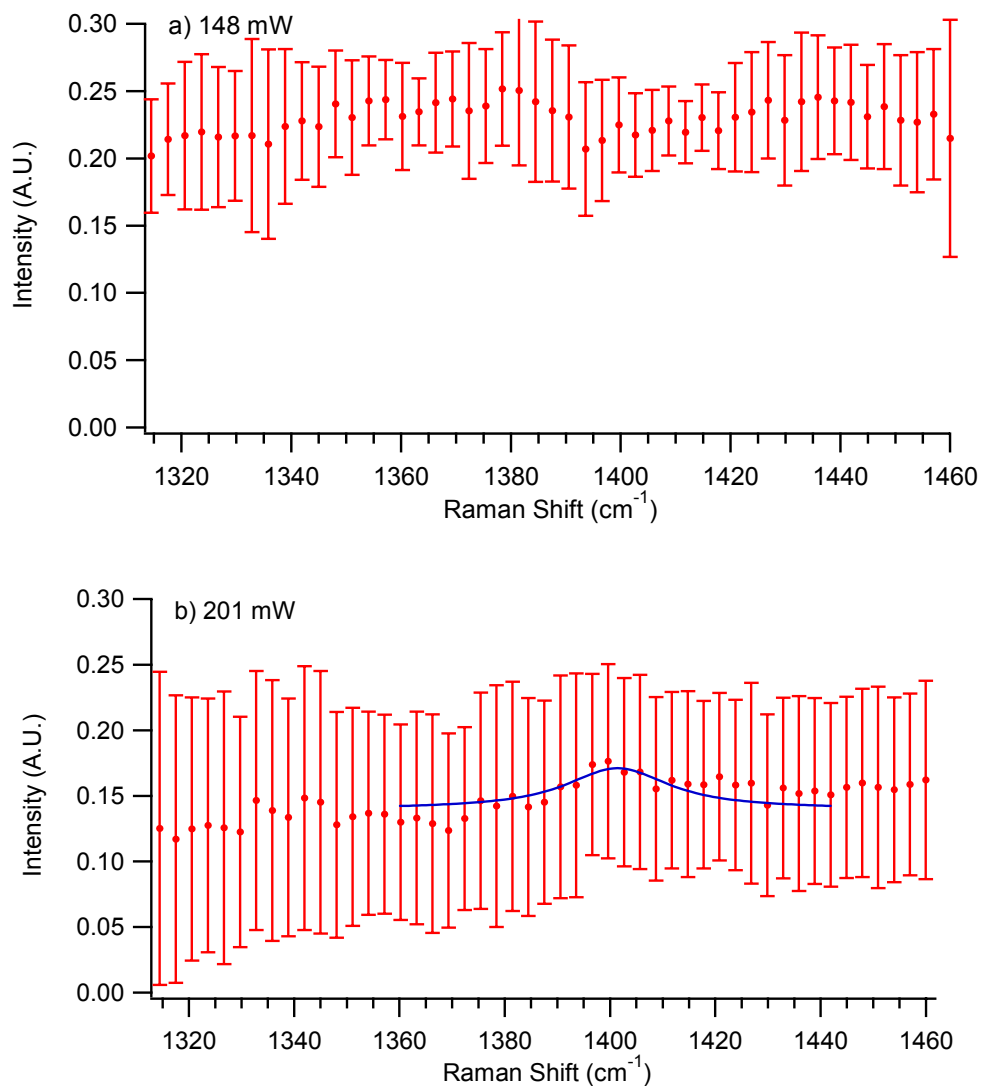
102

Figure A.11: Spectra of solvated CO_2 obtained with a PMT integration period consisting of 10,000 scans and an average of 17 spectra was used at laser energies of (a) 148 mW and (b) 201 mW. The spectra were obtained with a slit width of 100 um and a step size of 0.1 nm. The standard deviation error bars of the average are shown. A solvated CO_2 peak is observed in (b) only, and its spectral fit is shown in blue.
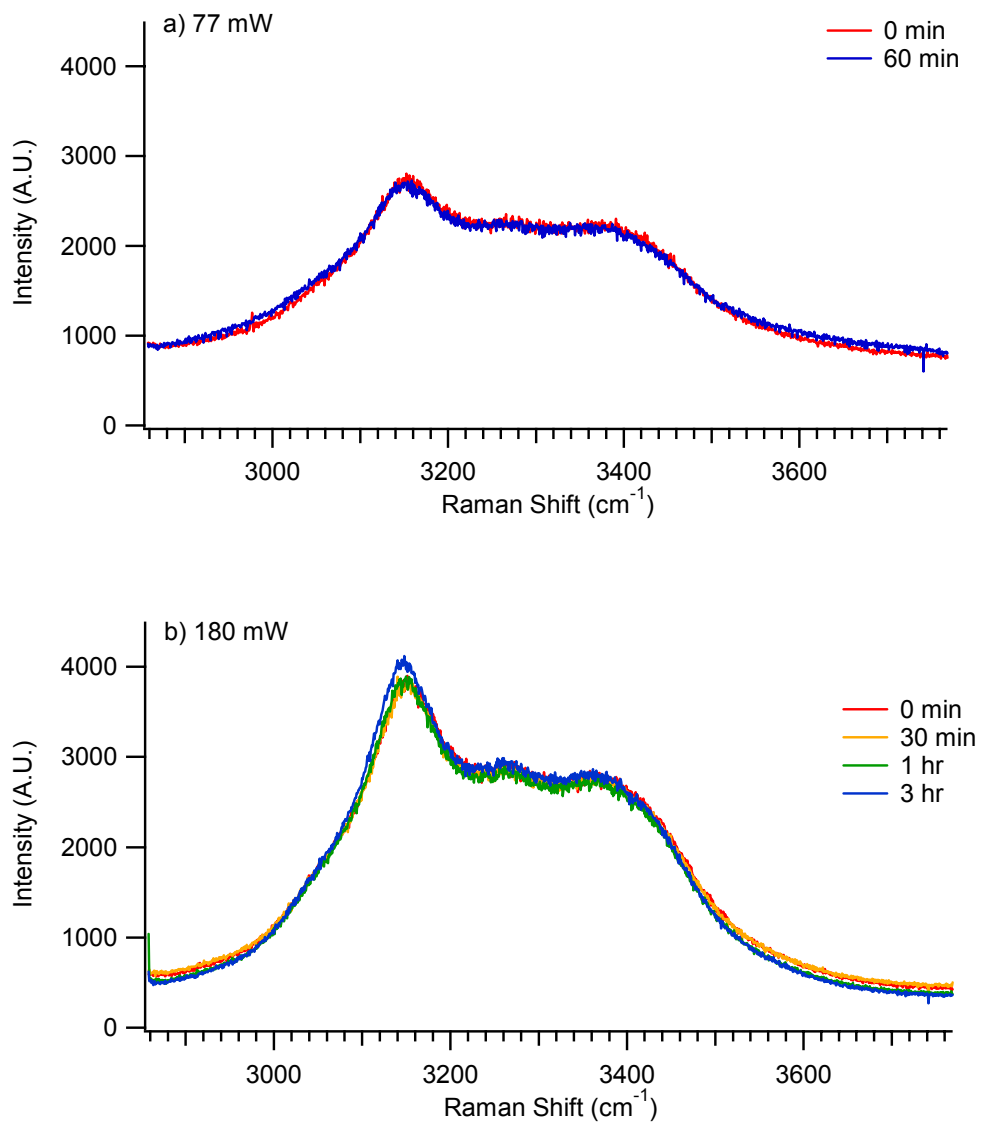
Figure A.12: The stretching region of $H_2O_{(s)}$ exposed to (a) 77 mW and (b) 180 mW laser energy for up to 3 hours. The spectra were obtained with the CCD camera with an integration time of 90 s, a 1200 g/mm grating, and a 50 um slit width.

APPENDIX B

PHOTOMULTIPLIER TUBE LABVIEW 7.1

B.1. Introduction

This appendix describes the LabVIEW 7.1 VI program used to obtain Raman spectra using a photomultiplier tube with a monochromator. The 500i PMT VI program allows communication between two instruments, the Spectral Products AD110B Photobyte-P PMT Detection System and the SpectraPro 500i Monochromator. This program is designed to easily obtain a spectrum by utilizing a scan setup with continuous data acquisition. A time delay is used to control the number of scans obtained at a set collection frequency. All spectra are individually saved as a dat file.

This LabVIEW VI program is a modified version of the one originally written by Gibum Kim and Paul Cremer from Texas A&M University. Dr. Dingfang Liu of the Allen Lab modified the LabVIEW VI program for using the AD110B Photobyte-P PMT detection system with other instruments in the laboratory. Modifications for use with the 500i monochromator were done with the assistance of Chris Beekman of the Allen Lab. An AD110B VI program developed by Spectral Products was modified and inserted into the 500i PMT VI program. Acton Research supplied the monochromator drivers.

B.2. Using the 500i PMT VI

This section explains the steps that must be followed to accurately collect data
with the 500i PMT VI program. The monochromator must be turned on before opening
the program, or it will not be recognized by the program.

1. Open **SpectraSense**. Go to *Hardware Setup*. The mirror position must be
   changed so the light is directed into the PMT instead of the CCD camera. On the
   monochromator image, two exit slits will be observed. Click on the exit slit that
   corresponds to the PMT. A click will be heard in the monochromator. The arrow
   direction will appear as shown in Figure B.1. To return to the CCD camera, click
   on the corresponding exit slit, and the arrow direction will appear as shown in
   Figure B.2.

2. Select appropriate grating.

3. Manually open the entrance slit by placing a checkmark in the box beside *ope*n.

4. Close **SpectraSense**.

5. Open **500i PMT VI**. The *Front Panel* is shown in Figure B.3. The *Block
   Diagram* is shown in Figure B.4.

6. Press the stop button on the navigation bar on the *Front Panel* because the
   program automatically runs when opened.

Front Panel Setup for the 500i PMT VI

All white boxes on the *Front Panel* require user input.

1) SCAN SETUP

7. Verify the *Scan Mode* is set at Scan. The 500i PMT VI program is designed to halt data collection if set at Fixed.

8. Enter the starting wavelength in *Begin nm*. Enter the final wavelength in *End nm*. The scan is designed to stop one wavelength past the *End nm*.

9. Indicate the number of scans to be obtained per nm in *Scans per nm*.

10. Enter the step increment to be used in *nm steps*, i.e. if 10 points per nm is needed, enter 0.10.

11. Enter the number of scans to be obtained in *Scans to run*.

12. The *Scan Delay* is used to prevent continuous running of the program. Insert the time (in milliseconds) between scans.

2) FILE SETUP

13. Under *Directory*, enter where the data is to be stored. The C drive is best for the programs used to display the data. Also, include the common name of the spectra, i.e. C:\Ashley\napth where "C:\Ashley" is the location and "napth" is the common name of the spectra.

3) PMT SETUP

14. The *Gain* may be adjusted to whatever gain the user desires. The default is set at x2, but x16 is recommended.

15. Set the *Voltage Setting* to ~900 V. The maximum voltage is dependent upon the PMT used. With the R3896 PMT, the maximum is 1000 V.

16. Under *Scans*, indicate the number of scans.

17. Open the laser shutter and turn on the PMT power supply.

18. Press the single arrow on the navigation bar at the top of the *Front Panel* to begin the scan.

Running 500i PMT VI Program

An update box is located between the *PMT SETUP* and the *SCAN CONTROL* boxes. A number of gray boxes, or indicators, verify the program is correctly controlling the monochromator. These indicators are vital to the program so a description follows:

19. *Points* indicates how many data points will be taken and plotted for each scan.

20. *Set Mono Wavelength* indicates at what wavelength the monochromator grating has been set. At the beginning of each scan, it will default to the begin nm and will auto-increment by the number entered in *nm steps*.

21. *Current NM* is the wavelength to which the monochromator is set. This is to verify the monochromator is working correctly and is vital to the program. If a −1.000 is observed instead of the number inserted into *Set Mono Wavelength*, the monochromator is not communicating effectively. The computer may need to be rebooted and/or the monochromator turned off.

22. *Elapsed Time* indicates the duration of the scan.

23. *Scans Completed* keeps the user informed of the progress of the scans.

24. The *Actual PMT Voltage* shows the voltage of the PMT after the scan is completed.

25. *Data* shows the signal voltage values.

26. *AVG* is the data point to be plotted for that wavelength. It is the average of all the PMT scans (i.e. 1000) and should correspond to the voltage from *Data*.
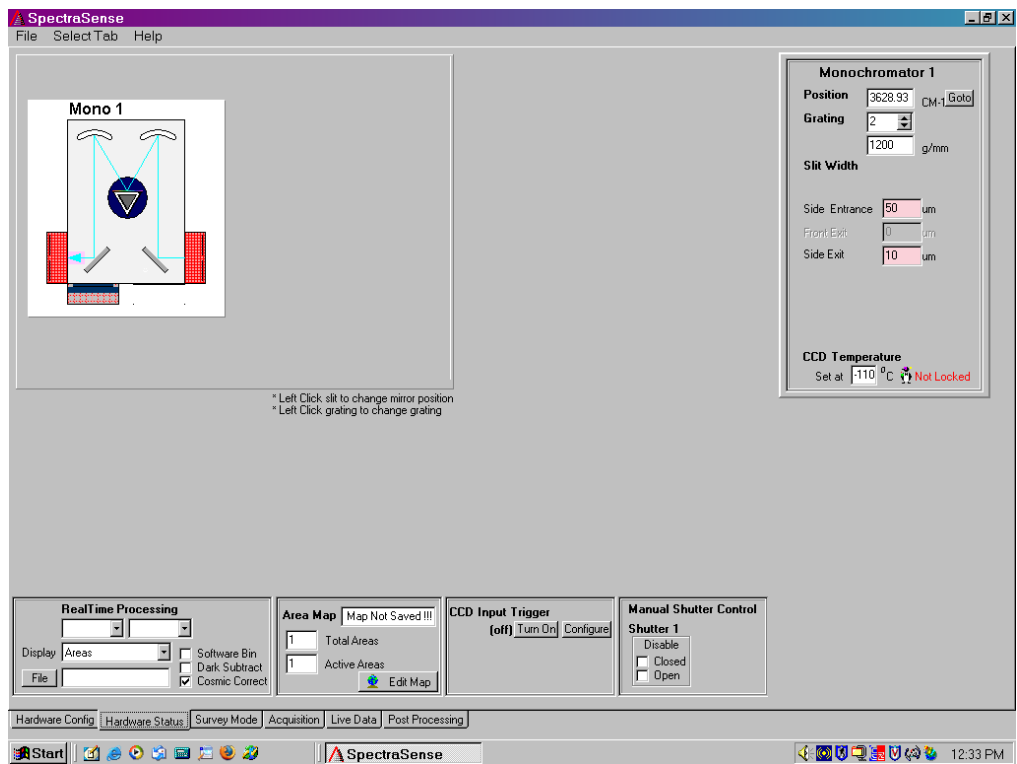
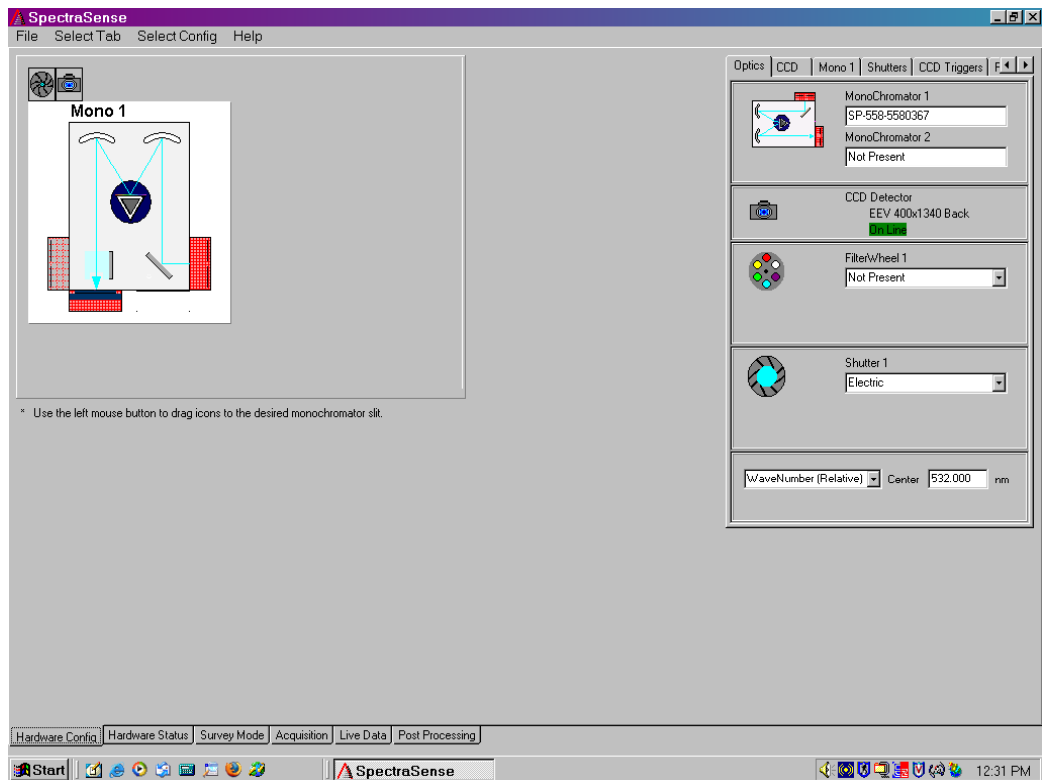**Figure B.1: SpectraSense monochromator diagram showing the laser path is towards the PMT.**

Figure B.2: SpectraSense monochromator diagram showing the laser path is towards the CCD camera.
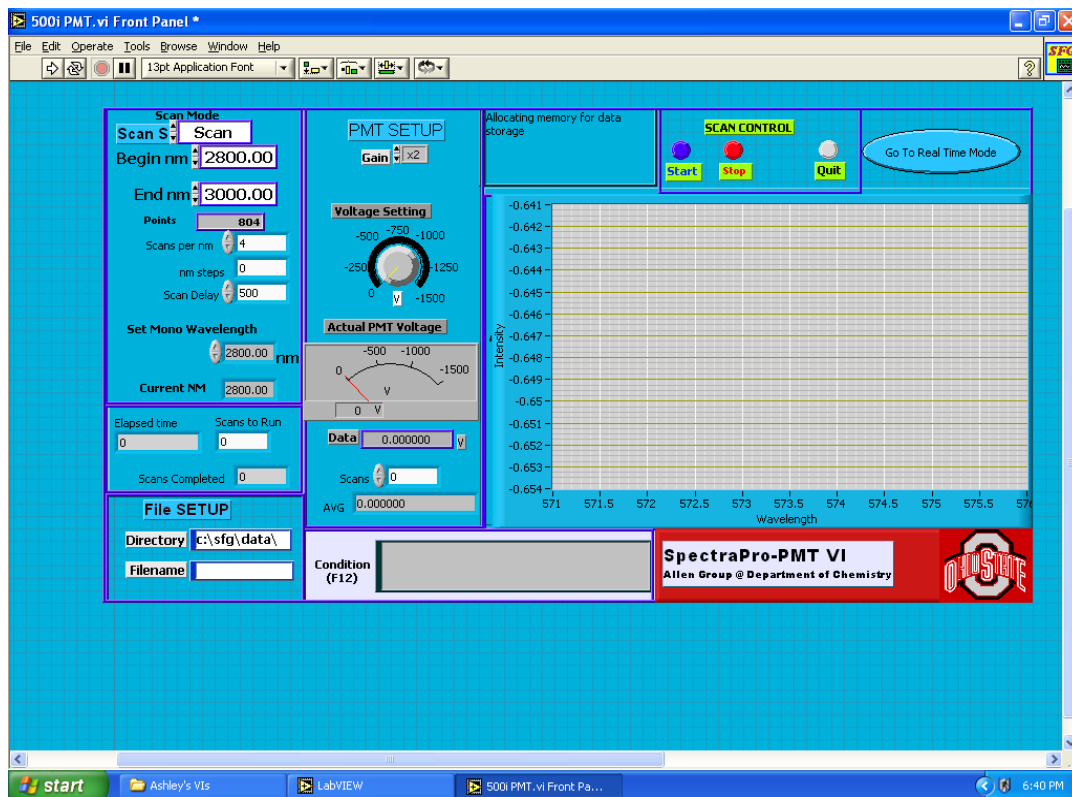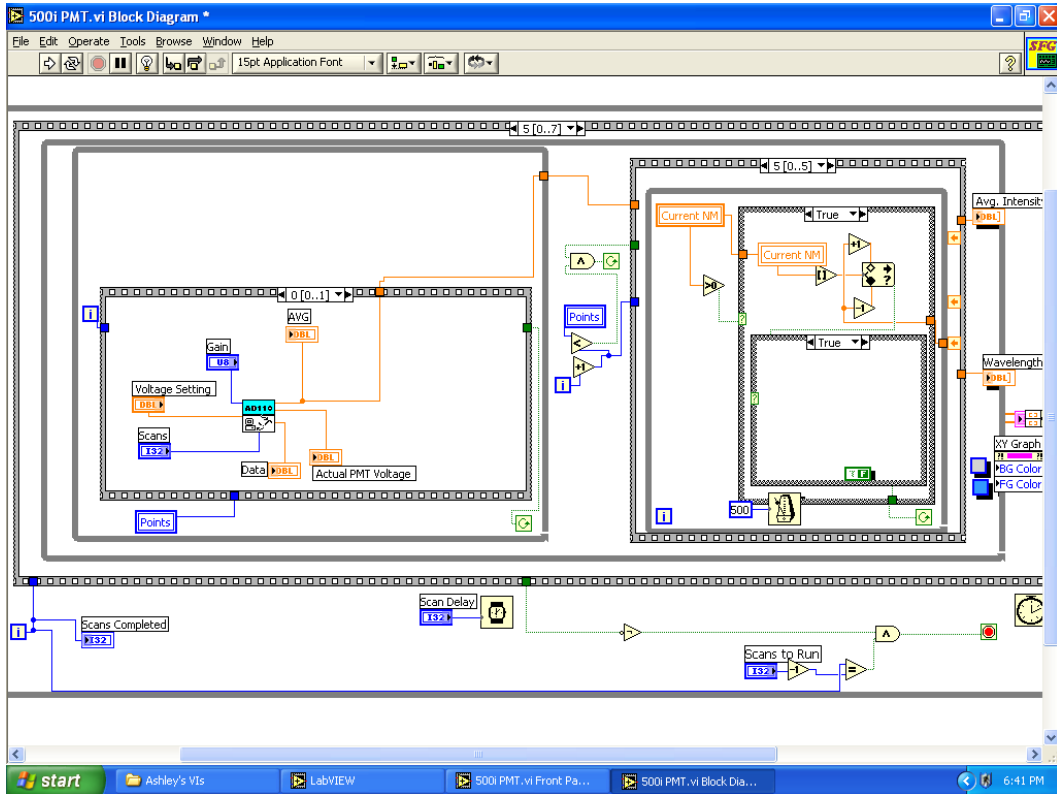
Figure B.3: Front Panel of the 500i PMT VI

Figure B.4: Block diagram of the 500i PMT VI

APPENDIX C

ANALYZING SPECTRASENSE SPECTRA IN IGOR PRO 4.0.5.1

C.1. Introduction

This appendix describes the Igor Pro (Wavemetrics, Version 4.0.5.1) macro used to analyze the Raman spectra acquired using SpectraSense (Acton Research, Version 4.2.9). The Raman macro was written by Lisa Van Loon of the Allen Lab to use with SpectraSense. The macro is designed to load individually saved spectra into one graph and table. Background subtracted spectra is provided as an option.

C.2. Using the Raman Macro

This section explains the steps that must be followed to accurately graph spectra.

1) Selecting Procedure

1. Open **IgorPro**. Go to *File*.

2. Go to *Open File*.

3. Select *Procedure*.

4. Browse for **Raman.ipf**.

5. Select **Raman.ipf**.

6. Set *limM* equal to number of spectra minus one.

2) Napthalene Spectrum

7. Specify the file location where spectra are stored in *NewPath/O path* "_", i.e. "C:Ashley:08.10.06:". Colons are used to separate files.

8. For *filename*, insert the default name SpectraSense is using. Use the naphthalene spectrum, i.e. "napth.arc_data"

3) Raw Data

9. Specify the file location where spectra are stored in *NewPath/O path* "_", i.e. "C:Ashley:08.10.06:". This should be the same location as naphthalene.

10. For *basefile*, indicate the common file name. This name is set in SpectraSense before acquisition, i.e. "clathrate1"

11. For *filename*, insert the default name used by SpectraSense. Use only the initial spectra, i.e. "clathrate1_001_Area01.arc_data"

4) Running the Raman Macro

12. To run macro, type *Raman()* into the command line of the command window.

13. Press *Enter*.

5) Background Subtraction Option

14. Repeat Step B. Use the background file instead of the naphthalene file.

15. Repeat Step C.

16. Delete the "//" inserted in the macro command: **wave1=wave1// - bkgd**

17. Repeat Step D.

The Raman macro written to analyze spectra acquired with SpectraSense is shown below:

```
#pragma rtGlobals=1              // Use modern global access method.
#include <Waves Average>

Macro raman()
```

```
Silent 1

KillWaves/A/Z

string  filename, wave0name, wave1name, basefile,xaxisname,
bkgdcorrected
string numstring

variable /g m, limM


m = 0
limM =100  // number of sample spectra minus one

NewPath/O path "c:ashley:08.10.06:"  //specify file location
filename = "naphth.arc_data"  //specify background file name
LoadWave/G/A/P = path filename

Rename wave0, wavenumbers
Rename wave1, bkgd

Edit wavenumbers, bkgd //starts table

Display bkgd vs wavenumbers as "bkgd"


NewPath/O path "c:ashley:08.10.06:"  //specify file location
basefile="clathrate1"   //specify the common file name

filename = "clathrate1_001_Area01.arc_data" //change this to match the
data file name Raman: loading the initial spectrum
      LoadWave/G/A/P=path filename


do
sprintf numstring, "%03d", (m+1)
filename = basefile + "_" + numstring + "_Area01.arc_data"
LoadWave/G/A/P=path filename

wave1=wave1// - bkgd //to load waves with no bkgd correction remove -
bkgd

wave0name = basefile + num2str(m+1) + "cm-1"
wave1name = basefile + num2str(m+1) + "au"


Rename wave0, $wave0name
Rename wave1, $wave1name

AppendtoTable $wave1name

if (m == 0) then
Display $wave1name vs wavenumbers as "data"
```

```
else

Append $wave1name vs wavenumbers

endif

ModifyGraph rgb($wave1name)=(10000,5000,m*100)

ModifyGraph tick(left)=2,mirror(left)=1,minor(left)=0,notation(left)=1
ModifyGraph font(left)="Arial"
Label left "Intensity (A.U.)"
ModifyGraph tick=2,mirror=1,minor=0,font="Arial"
Label bottom "Raman Shift (cm\\S-1\\M)"
ModifyGraph minor=1
SetAxis bottom 1200, 1500

m = m + 1

while (m<limM)

end
```